Three Dimensional (3D) Optical Information Processing

by

Kehan Tian

Submitted to the Department of Mechanical Engineering
in partial fulfillment of the requirements for the degree of

Doctor of Philosophy in Mechanical Engineering

at the

MASSACHUSETTS INSTITUTE OF TECHNOLOGY

June 2006

Author ....
Department of Mechanical Engineering
May 18, 2006

Certified by ....
George Barbastathis
Associate Professor of Mechanical Engineering
Thesis Supervisor

Accepted by ....
Lallit Anand
Chairman, Department Committee on Graduate Students

Three Dimensional (3D) Optical Information Processing

by

Kehan Tian

Submitted to the Department of Mechanical Engineering
on Mar. 18, 2006, in partial fulfillment of the
requirements for the degree of
Doctor of Philosophy in Mechanical Engineering

Abstract

Light exhibits dramatically different properties when it propagates in or interacts with 3D structured media. Comparing to 2D optical elements where the light interacts with a sequence of surfaces separated by free space, 3D optical elements provides more degrees of freedom to perform imaging and optical information processing functions.

With sufficient dielectric contrast, a periodically structured medium may be capable of forbidding propagation of light in certain frequency range, called band gap; the medium is then called a photonic crystal. Various "defects", *i.e.* deviations from perfect periodicity, in photonic crystals are designed and widely used as waveguides and microcavities in integrated optical circuits without appreciable loss. However, many of the proposed waveguide structures suffer from large group velocity dispersion (GVD) and exhibit relatively small guiding bandwidth because of the distributed Bragg reflection (DBR) along the guiding direction. As optical communications and optical computing progress, more challenging demands have also been proposed, such as tunable guiding bandwidth, dramatically slowing down group velocity and active control of group velocity. We propose and analyze shear discontinuities as a new type of defect in photonic crystals. We demonstrate that this defect can support guided modes with very low GVD and maximum guiding bandwidth, provided that the shear shift equals half the lattice constant. A mode gap emerges when the shear shift is different than half the lattice constant, and the mode gap can be tuned by changing the amount of the shear shift. This property can be used to design photonic crystal waveguides with tunable guiding bandwidth and group velocity, and induce bound states. The necessary condition for the existence of guiding modes is discussed. By changing the shape of circular rods at the shear interface, we further optimize our sheared photonic crystals to achieve minimum GVD. Based on a coupled resonator optical waveguide (CROW) with a mechanically adjustable shear discontinuity, we also design a tunable slow light device to realize active control of the group velocity of light. Tuning ranges from arbitrarily small group velocity to approximately the value of group velocity in the bulk material with the same average refractive index. The properties of eigenstates of tunable CROWs: symmetry and field distribution, and the dependence of the group velocity on the shear shift are also investigated. Using the finite-difference time-domain (FDTD) simulation, we demonstrate the process of tuning group velocity of light in CROWs by only changing the shear shift.

A weakly modulated 3D medium diffracts light in the Bragg regime (in contrast to Raman-Nath regime for 2D optical elements), called volume hologram. Because of Bragg selectivity, volume holograms have been widely used in data storage and 3D imaging. In data storage, the limited diffraction efficiency will affect the signal-noise-ratio (SNR), thus the memory capacity of volume holograms. Resonant holography can enhance the diffraction efficiency from a volume hologram by enclosing it in a Fabry-Perot cavity with the light multiple passes through the volume hologram. We analyze crosstalk in resonant holographic memories and derive the conditions where resonance improves storage quality. We also carry out the analysis for both plane wave and apodized Gaussian reference beams. By utilizing Hermite Gaussian references (higher order modes of Gaussian beams), a new holographic multiplexing method is proposed – mode multiplexing. We derive and analyze the diffraction pattern from mode multiplexing with Hermite Gaussian references, and predict its capability to eliminate the inter-page crosstalk due to the independence of Hermite Gaussian's orthogonality on the direction of signal beam as well as decrease intra-page crosstalk to lower level through apodization.

When using volume holograms for imaging, the third dimension of volume holograms provided more degrees of freedom to shape the optical response corresponding to more demanding requirements than traditional optical systems. Based on Bragg diffraction, we propose a new technique - 3D measurement of deformation using volume holography. We derive the response of a volume grating to arbitrary deformations, using a perturbative approach. This result will be interesting for two applications: (a) when a deformation is undesirable and one seeks to minimize the diffracted field's sensitivity to it and (b) when the deformation itself is the quantity of interest, and the diffracted field is used as a probe into the deformed volume where the hologram was originally recorded. We show that our result is consistent with previous derivations motivated by the phenomenon of shrinkage in photopolymer holographic materials. We also present the analysis of the grating's response to deformation due to a point indenter and present experimental results consistent with theory.

Thesis Supervisor: George Barbastathis
Title: Associate Professor of Mechanical Engineering

Acknowledgments

First of all, I would like to thank my advisor, Professor George Barbastathis. He has been a great teacher and friend throughout all these years. The most important thing George taught me was to pursue perfectness without compromise when proposing, conducting and presenting scientific research. He has been instrumental in guiding me during the course of my research and for this I will forever be grateful. I cannot thank him enough for all he did for me, and hope that one Chinese idiom could at least express my respect and gratitude to him, "my teacher one day, my father forever."

I would also like to thank my thesis committee: Professors Matthew J. Lang, Mark A. Neifeld, Demetri Psaltis, Peter So, and Dr. John Hong for inspiring me, guiding me, taking time to offer valuable advice on my work. I thoroughly enjoyed the discussions we had and have made it a point to follow their recommendations.

I would also like to thank my colleagues at the 3D Optical Systems group for all their help and stimulating discussions: Will Arora, Jose A. Dominguez-Caballero, Carlos Hidrovo, Stan Jurga, Anthony Nichol, Nick Loomis, Greg Nielson, Sebaek Oh, Wonshik Park, Troy Savoie, Nader Shaar, Wei-Chuan Shih, Arnab Sinha, Andy Stein, Paul Stellman, Satoshi Takahashi, Laura Waller, Zao Xu, and especially, Thomas Cuingnet and Zhenyu Li (at the Optical Information Processing group at Caltech) for their collaboration in the 3D deformation measurement project, Wenyang Sun, for his help and discussions in various projects.

Lastly and specially, I would like to thank my family. No gratitude is sufficient to repay the unceasing love of my parents, Fuyuan Tian and Qingzhen Zhu. I hope I make you proud. My career would not have been possible without the love and sacrifice of my wife, Wei Guo. She has been constantly supporting me, showing patience and understanding, and encouraging me every step of the way.

Contents

List of Figures

List of Tables

Chapter 1

Introduction

1.1 Three dimensional (3D) optical information processing

We live in a three dimensional (3D) world, and 3D optical information processing, such as communication, data storage, imaging, sensing, etc., is the inevitable challenge and goal for engineers and scientists. Though we can simplify and approximate our systems to 2D in many cases, the third dimension provides us more freedom in addition to the challenge. Here, "3D" means 3D structured medium. The light inside the medium interacts with the whole volume not a sequence of surfaces between which is free space. So lenses, prisms, mirrors, thin diffractive optical elements (e.g. thin gratings and holograms) and bulk uniform materials are not 3D in our definition.

Optical information processing has been extensively developed since the last century [1]. Fourier optics [1] is one of the main systematic approaches for optical information processing. 3D optical information processing becomes a more and more important branch of optical information processing since fabrication techniques and computational power have recently been developed to meet the precision requirements and complexities. 3D optical information processing is different with the typical systems in Fourier optics where 2D signal are mainly considered and processed as well as 2D optical elements are mainly used. In order to be capable of processing 3D signal, the system may lose some basic properties, such as invariance and linearity, in some dimension. Some intuitions we build for traditional signal processing systems may not be applicable. Even more, the effects of coherence may also differs within traditional 2D optical information processing systems.

1.2 Optical waves in 3D media

Light exhibits dramatically different properties when it propagates in or interacts with 3D structured media. In this thesis, we will mainly explore the light behavior in two typical 3D media: photonic crystals and volume holograms. Although these two materials are both formed by periodic dielectric modulations in thick media and their basic physical phenomena are both based on diffraction, there are also significant differences between them: e.g., photonic crystals have much higher dielectric contrast than volume holograms, the periodicity of photonic crystals is usually in the order of half the wavelength of light while in volume hologram the periodicity is usually between half wavelength to several wavelengths, and volume holograms can have much more complicated modulation patterns than photonic crystals.

Therefore, the fundamental theory, research methods and fabrication for photonic crystals and volume holograms are also different. Light behavior in both materials is governed by Maxwell's equations. Because the index modulation is weak in volume holograms, the first order Born approximation (perturbation) [2] or coupled mode theory [3] can be applied. Analytical solutions can be achieved and a systematic approach to volume holographic systems has been developed based on Fourier optics. On the other hand, due to the high dielectric contrast of photonic crystals, Maxwell's equations need to be solved numerically either in frequency domain or in time domain. Fabrication of volume holograms is also relatively easier and more controllable. To record two coherent beams interfering on a photosensitive thick holographic material can result in sufficient dielectric modulation. This recording process determines that the fabrication of volume holograms is much more flexible than that of photonic crystals. In order to have band gaps, high enough dielectric contrast is necessary for

2D and 3D photonic crystals (see Section 2.1.3 for more discussion). This requirement, in addition to subwavelength feature size, make the use of new lithography technique, rather than holographic recording, necessary for photonic crystals.

1.2.1 Photonic crystals

Photonic crystals are dielectric materials in which the refractive index is periodic in one, two or three dimensions. The validity of Bloch's theorem [4] for Maxwell equations implies the existence of photonic bands yielding allowed and forbidden frequency regions for light propagation, in analogy to electrons in crystalline solids. A photonic band gap may allow spontaneous emission to be suppressed as well as localization of light, as first proposed by E. Yablonovitch [5] and S. John [6]. The absence of allowed propagating electromagnetic modes inside the structures within the band gap gives rise to distinct optical phenomena such as high-reflecting omnidirectional mirrors and low-loss waveguiding among others. For example, a bulk crystal with a complete gap serves as a ideal mirror for lights along all directions; a patrial gap, on the other hand, allows light propagation only along certain directions and could serve as a substrate for a directional emitter; a point defect acts as a solid-state microcavity with confinement of the electromagnetic field in all directions [7, 8]; a linear defect in a photonic crystal acts as a channel waveguide for light propagation [7] and may also contain sharp bends [9]. The ability to tailor photonic bands for specific applications provides a systematic approach in controlling the properties of electromagnetic waves.

Research in the field of photonic crystals has undergone a rapid evolution in the last few years, due to the interest in basic physics and engineering as well as in prospective applications to photonic devices. The most immediate application of photonic crystal devices is in optical communications. Sharp-bend waveguides [9], channel-drop filters [10], waveguide crossings [11], and other devices for Wavelength-Division Multiplexing (WDM) systems are among the devices already realized and fabricated. Design and production of micro lasers, extremely bright LEDs, optical delay lines and next generation high-speed computers, as well as a variety of other optical circuits are among the goals of photonic crystals research.

To fabricate photonic crystals, materials with a periodic refractive index on the order of half a wavelength are needed. The most common way to accomplish this is to use two materials of different refractive index as building blocks for a periodic lattice. In the microwave region, the typical length scale is from millimeter to centimeter and photonic crystals can be fabricated easily. Because of the scaling properties of photonic crystals (following from the scaling properties of Maxwell's equations), experiments on such crystals were used to verify the photonic band structure calculations and also find applications to Terahertz devices [12, 13]. To scale down these ideas to visible and near-infrared wavelengths requires fabrication techniques that assemble structures on the order of several hundred of nanometers. This makes the fabrication cumbersome and complex. But in nature, one prominent example of a photonic crystal is the naturally occurring gemstone opal [14]. Its opalescence is essentially a photonic crystal phenomenon based on Bragg diffraction of light on the crystal's lattice planes. Another well-known photonic crystal is found on the wings of some butterflies such as the blue Morpho (Morpho granadensis) [15]. In laboratory, the nanofabrication problem has proven to be a main research direction and so far the fabrication of large size, high quality crystals still is a major challenge. Two fundamentally different approaches have been developed, based on either self-assembly of colloidal particles, or lithography combined with etching techniques. The self-assembly approach utilizes colloidal spheres that can self-organize in several different colloidal crystal symmetries if their size polydispersity (*i.e.* the relative width of the size distribution) is low enough [16, 17]. The main difficulties of this method are inflexibility in terms of structures with different lattice symmetries and inevitable random defects in photonic crystals. The other main method to fabricate photonic crystals is to use etching techniques. This approach requires the fabrication of lithographic masks with feature sizes down to 100nm. The mask is then used in an anisotropic etching process in high index materials. This technique is most suited for 2-D structures while 3D fabrication need to repeat the etching process layer by layer. Recently, more and more fabrication methods have been proposed for 3D photonic crystals, such as holographic lithography, inverse opal and other layer-by-layer methods [18, 19, 20]. It is worth noting that holographic lithography utilizes the "recording" idea from holograms. Four coherent, noncoplanar beams interfere with each order to determine the three primitive lattice vectors of 3D photonic crystals.

1.2.2 Volume holograms

Holography was invented by D. Gabor [21] in 1948. He recognized that when a suitable coherent reference is present simultaneously with the signal beam, the information about both amplitude and phase of the signal beam can be recorded even though the recording media respond only to light intensity. In the 1950's, E. N. Leith, who recognized the similarity of Gabor's holography to the synthetic-aperture-radar problem, suggested a modification of Gabor's original in-line holography that greatly improved the process. Both Gabor's and Leith's holograms are working in the Raman-Nath regime, generally diffracting the probe field that illuminates the holograms into multiple orders and in response to any probe field. Thus, they are actually "thin" holograms or 2D media.

Volume holography was first introduced by Van Heerden [22]. A volume hologram is created by recording the interference pattern of the reference and signal beams within the entire volume of a "thick" photosensitive material. Therefore, a volume hologram is essentially a 3D grating, or a superposition of 3D grating in a "thick" holographic material. A volume hologram diffracts in the Bragg regime, which means that only one order, the $+1^{st}$, is diffracted, and the properties of the diffracted field depend strongly on the probe field. For example, if the wavelength or angle of incidence of the probe field are different than the reference beam, then the diffracted beam may become very weak or even absent, called "Bragg selectivity". Because of these two key properties, volume holography has been been studied extensively [23, 3]. It is attractive for numerous coherent information processing [24] applications, including data storage [25, 26], optical interconnects [27], telecommunications [24], artificial neural networks [28], and imaging [29, 30]. Bragg selectivity in holographic data storage enables the multiplexing of thousands of data pages in one 3D medium. Similarly, in interconnects, the Bragg selectivity is used to create large numbers of non-interacting "data paths" [27]. In optical communications, the dispersion properties of volume diffraction are used instead as filter banks for spectral multiplexers or demultiplexers. The use of volume holograms as field transforming elements for imaging systems was proposed recently [29, 30]. This new imaging method is called volume holographic imaging (VHI). In this case, Bragg selectivity is designed to result in extreme position or color sensitivity, which in turn enables 3D imaging at long working distances with high resolution, minimal scanning and hyperspectral capability.

Several different kinds of materials have been investigated as volume holographic media. These include a number of photorefractive materials, such as iron-doped lithium niobate (Fe:LiNbO$_3$), organic materials and photopolymers [2]. The key point of departure between different holographic materials is the nature of the physical recording process, which largely determines most of the other properties of the storage medium. For instance, in an impurity-doped electro-optic oxide like Fe:LiNbO$_3$, an inhomogeneous space-charge distribution is created inside the medium via the diffusion of electron-hole pairs excited by the illuminating intensity, and the associated electric field then locally modulates the refractive index of the medium via the linear electro-optic effect. This mechanism determines this type of material optically erasable and hence suitable for reconfigurable applications while it also leads to volatility. On the other hand, refractive-index change in photopolymers is induced by polymerizing a monomer with visible illumination. Therefore, photopolymers are very promising due to their high sensitivity and dynamic range.

1.3 Outline of the thesis

We start by exploring the light propagation in photonic crystals. A shear discontinuity is proposed as a new type of defect in photonic crystals in Chapter 2. A brief introduction to photonic crystals and photonic crystal waveguides is given in Section 2.1 and 2.2, respectively. Detailed analysis of localized propagation modes guided by shear discontinuities is presented in Section 2.4. In Section 2.5, we investigate the dependence of guiding bandwidth and group velocity on shear shift. The bound states (localized resonance) are also discussed in detail. In Section 2.6, we discuss the necessary condition for the existence of guided modes and further optimize sheared photonic crystals by changing the shape of circular rods at the interface.

In Chapter 3, we design a tunable slow light device based on a coupled-resonator optical waveguide (CROW) with a mechanically adjustable shear discontinuity to realize active control of the group velocity of light. In Section 3.1, we give a brief introduction on CROWs. The modification of band structure and group velocity by introducing a shear discontinuity in a CROW is analyzed and discussed in Section 3.2. In Section 3.3, active control of group velocity is realized in a CROW with mechanically tunable shear discontinuity.

In Chapter 4, we continue exploring the light diffraction in volume holograms. Crosstalk in resonant holography and mode multiplexing are discussed in Chapter 4. First, we introduce the fundamental theory of volume hologram in Section 4.1. We also calculate and compare crosstalk in angle– and shift– multiplexed holographic memories. Resonant holography is discussed in Section 4.3. In Section 4.4, we carry out the calculation for the case of unapodized plane wave reference, and find out the condition where resonance is favorable. In Section 4.5, we show that further improvement is achieved by apodization with Gaussian references, which is well known for non-resonant memories. In Section 4.6, we discuss a new multiplexing method – mode multiplexing with Hermite-Gaussian references. The diffraction response is derived and simulated in this section, and the crosstalk in mode multiplexing is also analyzed.

In Chapter 5, based on our VHI system, we propose a new technique for 3D deformation measurement using volume holograms. First, we introduce the principles and properties of VHI systems and derive the optical response of VHI in Section 5.1. We provide general expressions that are applicable to arbitrary deformations under a set of mildly restrictive assumptions, such as preservation of the average index of refraction and validity of the 1^{st}-order Born approximation. The derivation is carried out in Section 5.3 for small deformations for which a perturbative approach is adequate, and in a more general (but also more algebraically complex) form in

Sections 5.6 and 5.7. In Section 5.4, we confirm that the general theory matches with the well known predictions and observations of shrinkage effects from the literature. In Section 5.5, we carry out the modeling of the diffracted field and report experimental results in the case of a deformation produced by an indenter tip applied against the surface of a semi-infinite slab. The experiments match very well with the theory.

We conclude in Chapter 6 by summarizing the main advantages and challenges of 3D optical information processing. We discuss some promising directions of future work in this field.

Chapter 2

Localized propagation modes guided by shear discontinuities in photonic crystals

2.1 Photonic crystals

Photonic crystals are periodically structured eletromagnetic media, generally possessing photonic band gaps: ranges of frequency in which light can not propagate through the structure [31, 32, 33, 34, 35]. The length scale of the periodicity is proportional to the wavelength of light in the band gap. The periodicity of photonic crystals is the electromagnetic analogue of a crystalline atomic lattice, which acts on the electron to produce the energy band gaps in semiconductors. The study of photonic crystals is likewise governed by Maxwell's Equations and the Bloch theorem.

2.1.1 Maxwell's equations for photonic crystals

All of macroscopic electromagnetism including the propagation of light in a photonic crystal is governed by Maxwell's equations (in MKS units):

$$\nabla \cdot \mathbf{D}\left(\mathbf{r}, t\right) = \rho, \tag{2.1}$$

$$\nabla \cdot \mathbf{B}(\mathbf{r}, t) = 0, \tag{2.2}$$

$$\nabla \times \mathbf{E}(\mathbf{r}, t) = -\frac{\partial}{\partial t}\mathbf{B}(\mathbf{r}, t), \tag{2.3}$$

$$\nabla \times \mathbf{H}(\mathbf{r}, t) = \frac{\partial}{\partial t}\mathbf{D}(\mathbf{r}, t) + \mathbf{J}, \tag{2.4}$$

where **E** and **H** are the electric and magnetic fields, **D** and **B** are the electric displacement and magnetic induction, and ρ and **J** are the free charges and currents. In the absence of free charges and currents, we can set $\rho = 0$ and $\mathbf{J} = 0$. In order to solve Maxwell's Equations, we need to relate **B** to **H** and **D** to **E** by constitutive equations. Considering that photonic crystals, normally, are not realized in magnetic materials, we can assume the magnetic permeability equal to that in free space, μ_0, so that

$$\mathbf{B}(\mathbf{r}, t) = \mu_0 \mathbf{H}(\mathbf{r}, t). \tag{2.5}$$

As for **D** and **E**, quite generally the components D_i of the displacement field are related to electric field components E_i by the following power series [36]:

$$D_i = \sum_j \epsilon_{ij} E_j + \sum_j \chi_{ijk} E_j E_k + O(E^3). \tag{2.6}$$

For most cases, we can simplify 2.6 using the following assumptions. First, we assume that the field strengths are small enough so that we are in the linear regime. Therefore, χ and all higher order terms can be dropped. Second, we assume that the material is macroscopic and isotropic so that the dielectric constant can be approximated by a scalar $\epsilon(\mathbf{r}, \omega)$. Third, we ignore any explicit frequency dependence of the dielectric constant. Instead, we simply choose a value of the dielectric constant appropriate to the frequency range of the physical system we are considering. Fourth, we focus only on low-loss materials, which means that the imaginary part of $\epsilon(\mathbf{r})$ is negligible. The electric displacement is thus given by

$$\mathbf{D}(\mathbf{r}, t) = \epsilon_0 \epsilon(\mathbf{r}) \mathbf{E}(\mathbf{r}, t), \tag{2.7}$$

where ϵ_0 is the free space dielectric constant and $\epsilon(\mathbf{r})$ denotes the spatially varying relative dielectric constant of the photonic crystal. Since Maxwell's equations are linear, it is convenient to solve the field distribution in the form of harmonic fields and obtain the general solution as a superposition of harmonic modes. The electric and magnetic fields **E** and **H** are expanded into a set of harmonic modes. Each mode has the following temporal characteristics:

$$\mathbf{E}(\mathbf{r},t) = \mathbf{E}(\mathbf{r})e^{i\omega t}, \mathbf{H}(\mathbf{r},t) = \mathbf{H}(\mathbf{r})e^{i\omega t}. \tag{2.8}$$

By substituting constitutive relations 2.5 and 2.7 into Maxwell's Equations 2.1– 2.4 as well as using the harmonic mode representations 2.8, we can obtain a closed form equation for the magnetic field:

$$\nabla \times \left\{ \frac{1}{\epsilon(\mathbf{r})} \nabla \times \mathbf{H}(\mathbf{r}) \right\} = \frac{\omega^2}{c^2} \mathbf{H}(\mathbf{r}), \tag{2.9}$$

where c stands for the light velocity in free space:

$$c^2 = \frac{1}{\epsilon_0 \mu_0}. \tag{2.10}$$

It is worth noting that Eq. 2.9 is a Hermitian eigenvalue problem whose solutions are determined entirely by the properties of the dielectric function $1/\epsilon(\mathbf{r})$. $\nabla \times \frac{1}{\epsilon(\mathbf{r})} \nabla \times$ is a Hermitian eigen-operator, and $\mathbf{H}(\mathbf{r})$ and ω^2/c^2 are the eigenmode and eigenvalue, respectively.

2.1.2 Bloch theorem

The study of wave propagation in 3D periodic media was pioneered by Felix Bloch in 1928, unknowingly exending an 1883 theorem in one dimension by G. Floquet. Bloch proved that waves in such a medium can propagate without scattering. Their behavior is governed by a periodic function $u_{n\mathbf{k}}(\mathbf{r})$ (Bloch envelope) multiplied by a plane wave $e^{i\mathbf{k}\cdot\mathbf{r}}$

$$\psi_{n\mathbf{k}}(\mathbf{r}) = e^{i\mathbf{k}\cdot\mathbf{r}} u_{n\mathbf{k}}(\mathbf{r}), \tag{2.11}$$

where **k** is the plane wave vector (Bloch wavevector) which is unique up to a reciprocal lattice vector, and n is the index of the solutions (there are a number of solutions for a given **k**). Although Bloch studied quantum mechanics, the same techniques can be applied to electromagnetism by casting Maxwell's equations in the form of an eigenproblem in analogy with Schrödinger's equation, as we derived in Section 2.1.1: the two curls in Eq. 2.9 correspond roughly to the "kinetic energy" and $1/\epsilon$ to the "potential".

A photonic crystal corresponds a periodic dielectric function $\epsilon(\mathbf{r}) = \epsilon(\mathbf{r} + \mathbf{R}_i)$ for some primitive lattice vectors $\mathbf{R}_i$ ($i = 1, 2, 3$ for a crystal periodic in three dimensions.) In this case, Bloch's theorem for electromagnetism states that the solutions to Eq. 2.9 can be chosen of the form

$$\mathbf{H}(\mathbf{r}) = e^{i\mathbf{k}\cdot\mathbf{r}}\mathbf{H}_{n\mathbf{k}}(\mathbf{r}). \tag{2.12}$$

The eigenvalues are $\omega_n(\mathbf{k})$, where $\mathbf{H}_{n\mathbf{k}}(\mathbf{r})$ is a periodic envelope function satisfying

$$(\nabla + i\mathbf{k}) \times \frac{1}{\epsilon(\mathbf{r})}(\nabla + i\mathbf{k}) \times \mathbf{H}_{n\mathbf{k}}(\mathbf{r}) = \frac{\omega_n(\mathbf{k})^2}{c^2}\mathbf{H}_{n\mathbf{k}}(\mathbf{r}). \tag{2.13}$$

Eq. 2.13 yields a Hermitian eigenproblem over the primitive cell at each Bloch wavevector **k**. When the primitive cell is finite, the eigenvalues are discrete, labeled by $n = 1, 2, 3\ldots$ These eigenvalues $\omega_n(\mathbf{k})$ are continuous functions of **k**, forming discrete bands in a dispersion diagram. Note also that **k** is not required to be real; complex **k** gives evanescent modes that will exponentially decay from the boundaries of a finite crystal, but cannot exist in bulk.

2.1.3 Photonic band gap

The easiest way to understand the origin of photonic band gaps is to compare it to the energy gap in a semiconductor. In a silicon crystal, for example, the atoms are arranged in a diamond lattice structure, and electrons moving through this lattice experience a periodic potential as they interact with the silicon nuclei via the Coulomb force. This interaction results in the formation of allowed and forbidden energy states.

For pure and perfect silicon crystals, no electrons are to be found in an energy range called the forbidden energy gap or simply the band gap.

Now consider photons moving through a block of transparent dielectric that contains periodically arranged high and low refractive index materials. The photons pass through regions of high refractive index interspersed with regions of low refractive index. To a photon, this contrast in refractive index looks just like the periodic potential that an electron experiences traveling through a silicon crystal. Indeed, if there is large contrast in refractive index between the two regions, then most of the light will be confined either within the high refractive index material or the low refractive index material. This confinement results in the formation of allowed energy regions separated by a forbidden region - the so-called photonic band gap. This result follows from the properties of the Hermitian eigensystem (Eq. 2.13), namely that the eigenvalues minimize the variational problem

$$\omega_n^2(\mathbf{k}) = \min_{\mathbf{E}_{n\mathbf{k}}} \frac{\int |(\nabla + i\mathbf{k}) \times \mathbf{E}_{n\mathbf{k}}|^2}{\int \epsilon \, |\mathbf{E}_{n\mathbf{k}}|^2} c^2. \tag{2.14}$$

In Eq. 2.14, $\mathbf{E}_{n\mathbf{k}}$ is the periodic electric field envelope which can be obtained from the periodic envelope function of the magnetic field. The numerator minimizes the "kinetic energy" and the denominator minimizes the "potential energy." Furthermore, the bands $n > 1$ are additionally constrained to be orthogonal to the lower bands m:

$$\int \mathbf{H}_{m\mathbf{k}}^* \cdot \mathbf{H}_{n\mathbf{k}} = \int \epsilon \mathbf{E}_{m\mathbf{k}}^* \cdot \mathbf{E}_{n\mathbf{k}} = 0. \tag{2.15}$$

Therefore, at each $\mathbf{k}$, there will be a gap between the lower bands concentrated in the high dielectric (low potential) and the upper bands that are less concentrated in the high dielectric because they are forced out by the orthogonality condition or must have fast oscillation that increase their kinetic energy. By this argument, it follows that any periodic dielectric variation in one dimension will lead to a band gap while in order to obtain a complete band gap in 2D or 3D, two additional conditions need to be satisfied. First, although in each symmetry direction of the the crystal and each $\mathbf{k}$ there will be a band gap by the 1D argument, these band gaps will not necessarily overlap in frequency. For the gaps to overlap, the gaps must be sufficiently large, which implies a minimum dielectric contrast to each geometry. Second, following the vectorial boundary conditions on the electric field, moving across a dielectric boundary from ϵ to $\epsilon' < \epsilon$, $\epsilon \left|\mathbf{E}\right|^2$ will decrease discontinuously if $\mathbf{E}$ is parallel to the interface ($\mathbf{E}_{\parallel}$ is continuous) and will increase discontinuously if $\mathbf{E}$ is perpendicular to the interface ($\mathbf{E}_{\perp}$ is continuous). This means that it is much harder to strongly contain the field energy in the high dielectric whenever the electric field has component perpendicular to the dielectric boundary, and vice versa. Thus, the band gaps exist for the polarization direction where the electric field lines do not need to cross a dielectric boundary. In order words, to obtain a large band gap, a dielectric structure should consist of thin, continuous veins or membranes along the electric field polarization direction.

Usually a bulk photonic crystal is of less interest than the existence of a defect in it. This is because defects can support localized states whose properties are dictated by the nature of the defect. A point defect could act as a mircocavity and a line defect as a waveguide. The design of defects enables us to tailor the band structures for specific applications and model the flow of light corresponding to different demands. Therein lies the potential of photonic crystals.

2.2 Photonic crystal waveguides

Certain defects in photonic crystals can lead to localized states in the defect's vicinity. For example, by introducing a line defect, we can induce a guided mode along the defect axis for a band of frequencies inside the band gap [7]. Such a waveguide does not rely on the total internal reflection as regular dielectric waveguides do. Because of that, the evanescent region is virtually zero. Light can be guided without appreciable losses for a wide range of frequencies and transmitted efficiently around sharp corners [9], even if the radius of curvature of the bend is on the order of one wavelength. Conventional photonic crystal waveguides consist of a missing row of rods or holes in a two-dimensional (2-D) array of dielectric rods or air holes. These structures have been studied extensively in both theory [7, 9, 37] and experiments [38, 39]. However, many of the proposed waveguide structures suffer from a large group velocity dispersion (GVD) and exhibit relatively small guiding bandwidth because of the distributed Bragg reflection (DBR) along the guiding direction. Techniques that have been proposed to mitigate guided mode dispersion have been either successful for relatively small bandwidth or involve a combination of slab mode and photonic crystal confinement [40, 41, 42].

In this chapter, we propose a new type of defect, consisting of a shear discontinuity in an otherwise periodic photonic crystal lattice, as shown in Fig. 2-1. Such a defect can confine optical waves to propagate along the shear plane. Such guided waves are sometimes referred to as zero mode [43] or surface waves. The confined propagation mode is effective over the entire band gap, provided that the shear shift equals half the lattice constant. The guided modes avoid large GVD due to flattening of the dispersion curve. This is because the local period is half the lattice constant and thus breaks the DBR condition. The low GVD makes this structure very promising for high speed transmission, high speed optical signal processing and highly integrated optical circuits. Alternatively, the shear shift can be adjusted as a parameter to tailor a particular dispersion response. If the shear shift is not equal to half the lattice constant, a mode gap [44] emerges inside the band gap. This property can be used to implement a tunable optical filter or optical switch. We also investigate the coupling efficiency between a guided mode external to the photonic crystal and the shear mode, with the shear shift as a parameter. The group velocity can also be tuned by changing the shear shift. This enables us to realize tunable, slow light devices. We find that the existence of surface waves for each half of the sheared photonic crystals is a necessary condition for the existence of guided modes. The mode gap introduced by the shear shift can also be used to induce bound states [44]. By changing the shape of circular rods at the interface (height h in Fig. 2-1(b)), we can further optimize the design of our sheared photonic crystals to achieve minimum GVD or other requirements.

We will continue this chapter with a brief introduction of computational methods

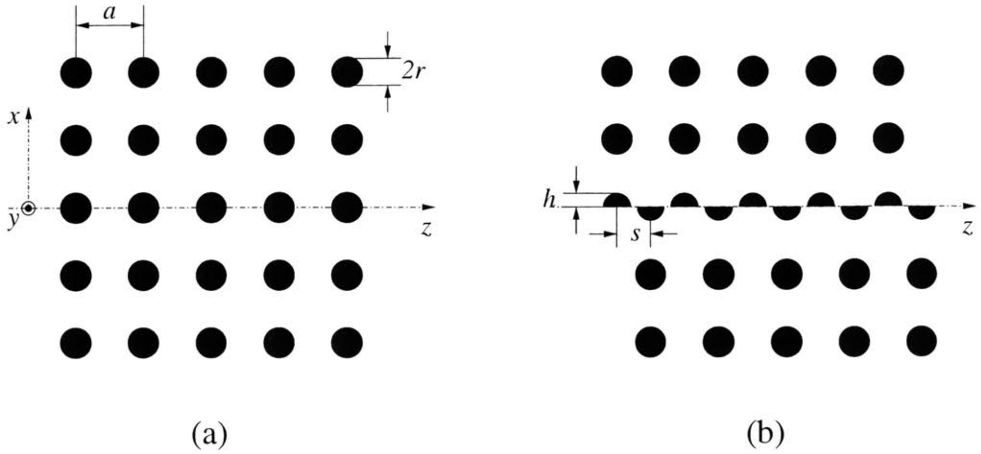

Figure 2-1: Two dimensional photonic crystals: (a) square lattice of dielectric rods in air, with lattice constant a and radius $r = 0.2a$ (b) photonic crystal lattice with shear discontinuity (sheared photonic crystals) with shear shift $s = a/2$ and cylinder section height at the interface $h = r$.

that we will use to investigate a photonic crystal and its defect states. Detailed analysis of localized propagation modes guided by shear discontinuities is presented in Section 2.4. In Section 2.5, we investigate the dependence of the guiding bandwidth and group velocity on the shear shift. The bound states (localized resonance) are also discussed in detail. In Section 2.6, we discuss the necessary condition for the existence of guided modes and further optimize sheared photonic crystals by changing the shape of circular rods at the interface.

2.3 Computational methods

To investigate the properties of a photonic crystal and its defect states, two different computational approaches are used. The first solves Maxwell's equations in the frequency domain, while the second solves the equations in the time domain. These two methods reveal different information about photonic crystals and their defects. The frequency-domain method yields the dispersion relationship, polarization, symmetry, and the field distributions of its eigenstates, while the time-domain method allows us to determine the temporal behavior of the modes. By exploiting the evolution of the fields in time, we will be able to determine the coupling efficiency, the steady state, the scattering and the quality factor of cavities.

2.3.1 Frequency domain

In the first method, one concentrates on solving the field distribution of the harmonic state of electromagnetic field from Maxwell's equations. The fields are expanded into a set of harmonic modes representations 2.8 and solved by using the wave equation 2.9 for the magnetic field. Eq. 2.9 is an eigenvalue problem which can be rewritten as

$$\Theta \mathbf{H}_n = \lambda_n \mathbf{H}_n \tag{2.16}$$

where Θ is a Hermitian differential operator and λ_n is the nth eigenvalue, proportional to the squared frequency of the mode. The Hermitian eigenvalue problem (2.9) can be solved by using a variational approach where each eigenvalue is computed separately by minimizing the functional $< \mathbf{H}_n|\Theta|\mathbf{H}_n >$. This method is described in more detail in Ref. [45] and implemented by the MIT Photonic-Bands (MPB) package. Briefly, to find the minimum, we use the conjugate gradient method with preconditions. The gradient method has the advantage of being more efficient than the traditional method of steepest descent, in that it requires fewer iterations to reach convergence. In order to minimize the functional, we need to calculate

$$\Theta \mathbf{H}_n (\mathbf{r}) = \left\{ \nabla \times \frac{1}{\epsilon (\mathbf{r})} \nabla \times \right\} \mathbf{H}_n (\mathbf{r}) . \tag{2.17}$$

Since the curl is a diagonal operator in reciprocal space and $1/\epsilon (\mathbf{r})$ is a diagonal operator in real space, each of these operators is computed in the space where it is diagonal by going back and forth between real and reciprocal space using fast Fourier transforms (FFT's). This allows the operator Θ to be diagonalized without storing every element of the $N \times N$ matrix; instead, only the N elements of $\mathbf{H}_n$ need to be stored. Therefore, we will be able to consider structures of very large dimensions.

Because of piecewise continuity of the true dielectric function in many systems of interest, the main source of inaccuracy is the coarseness of the FFT grid along the boundary between dielectrics. This is compensated for by smoothing the dielectric constant along the boundaries. To calculate the band structure of a periodic system, the computational cell is chosen to be one unit cell of the periodicity. To study eigenstates of systems that are intrinsically non-periodic, such as cavities, surfaces and waveguides, one could employ the supercell approximation in which the non-periodic system is periodically repeated in space. The spurious effects introduced by the artificial periodicity can be either minimized or estimated by the use of supercells of increasingly larger size.

2.3.2 Time domain

The second method solves Maxwell's equations in real space, where the explicit time dependency of the equations is maintained. The equations for the electric and magnetic fields can be written as

$$\mu_0 \frac{\partial}{\partial t} \mathbf{H}(\mathbf{r}, t) = -\nabla \times \mathbf{E}(\mathbf{r}, t) \tag{2.18}$$

$$\epsilon_0 \epsilon(\mathbf{r}) \frac{\partial}{\partial t} \mathbf{E}(\mathbf{r}, t) = \nabla \times \mathbf{H}(\mathbf{r}, t) \tag{2.19}$$

These equations can be solved by using the Finite-Difference Time-Domain (FDTD) method. Eqs. 2.18 and 2.19 are discretized on a simple cubic lattice, where space-time points are separated by fixed units of time and distance. The derivatives are approximated at each lattice point by a corresponding centered difference, which gives rise to finite-difference equations. By solving these equations, the temporal response of the structures can be determined. In solving Eqs. 2.18 and 2.19, special attention must be given to the fields at the boundary of the finite-sized computational cells. Since information outside the cell is not available, the fields at the edges must be updated using boundary conditions. In our simulations, perfectly matched layer (PML) boundary conditions are used to minimize back reflections into cells.

2.4 Localized propagation modes guided by shear discontinuities

We start with a conventional 2-D photonic crystal consisting of dielectric rods in air on a square array with lattice constant a, as shown in Fig. 2-1(a). Just as the regular arrangement of atoms in a crystal gives rise to band gaps, here the spatial periodicity of the dielectric index may prevent electromagnetic waves of certain frequencies from propagating inside the photonic crystal. As a numerical example, we assume that the refractive index of the rods is 3.0 and the radius is $r = 0.2a$. The crystal has a TM (magnetic field in-plane) band gap which extends from frequency $\omega = 0.323 \times 2\pi c/a$ to $\omega = 0.443 \times 2\pi c/a$. The gap range corresponds to the canonical free-space wavelength for light between 451nm and 619nm when $a = 0.2\mu$m. Subsequent simulations use this value of a and center wavelength $\lambda_0 = 550$nm. Here we restrict our analysis to TM modes.

We introduce a shear discontinuity in the middle row, as shown in Fig. 2-1(b). The circular dielectric rods in the middle row are cut in half (the height $h = r$). In this section, we will restrict our analysis to shear shift $s = a/2$, *i.e.* exactly one half the lattice constant. General shear shifts will be discussed in Section 2.5. When light of frequency within the band gap enters the photonic crystal along the shear plane, we can expect that the light will be well confined near the shear plane. This is because the upper and lower halves are still perfect photonic crystals and there are no extended modes into which the propagating wave can couple. Unlike other guided mode structures, the transverse confinement is induced by a zero thickness entity: the shear plane. The computational setup is shown in Fig. 2-2. A slab waveguide with core index 1.5 and core thickness 0.4μm sandwiched by clading of index 1.0 is used to couple the light source into the sheared photonic crystal with lattice constant $a = 0.2\mu$m and radius of rods $r = 40$nm. Using the FDTD method, we simulated a 10fs pulse with center wavelength of 550nm being injected by an external waveguide near the tip of the shear plane. All the FDTD simulations in this chapter are 2-D. Because the spectrum of the pulse is mostly inside the band gap of the photonic

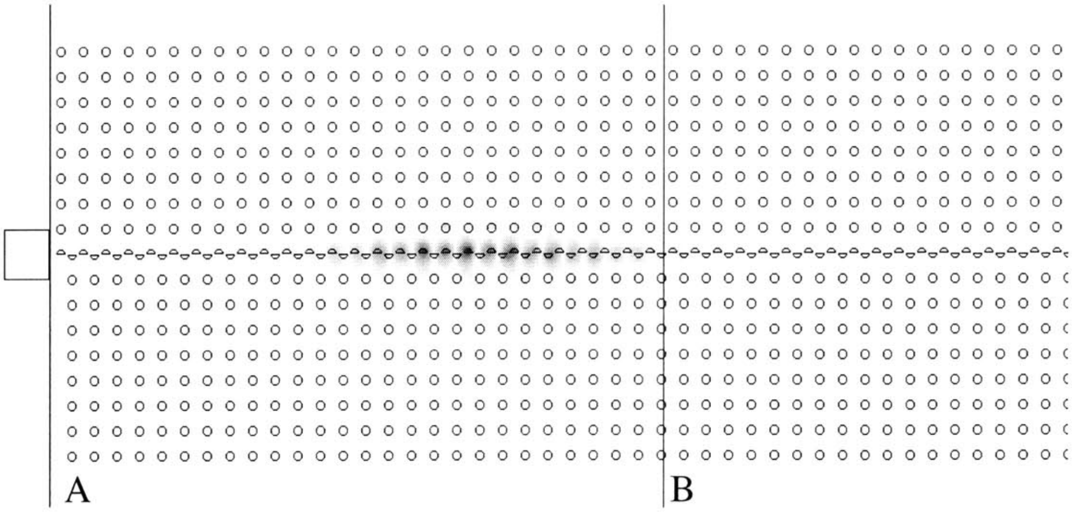

Figure 2-2: (Color) A pulse is coupled in by a slab waveguide and propagates inside the sheared photonic crystal. The pulse duration is 10fs and the center wavelength is 550nm. Plane A is at the end of the slab waveguide and Plane B is located 5.5μm away from Plane A.

crystal, we can see from Fig. 2-2 that the entire pulse is well confined to the shear plane.

The dispersion diagrams for the sheared photonic crystals in this chapter are calculated by solving Maxwell's equations in the frequency domain for the given dielectric configurations as described in Section 2.3.1. A supercell of size $15a \times a$ with periodic boundary conditions is used as the computational domain. Because the guided modes are sufficiently localized and the width of the supercell is large enough, the introduction of the supercell has a negligible effect on the results. When the shear shift equals half the lattice constant and the shear discontinuity is formed by half circular dielectric rods, the dispersion relation is illustrated as the solid line in Fig. 2-3, indicating the existence of two guided modes inside the band gap.

Two important features of the dispersion diagram are worth pointing out. First, no flattening occurs at the edge of Brillouin zone X ($k = \pi/a$), unlike in conventional photonic crystal waveguides. The flattening is very undesirable for optical signal transmission, since it makes guided modes suffer from large GVD. The primary physical reason for the flattening in conventional photonic crystal waveguides is the DBR

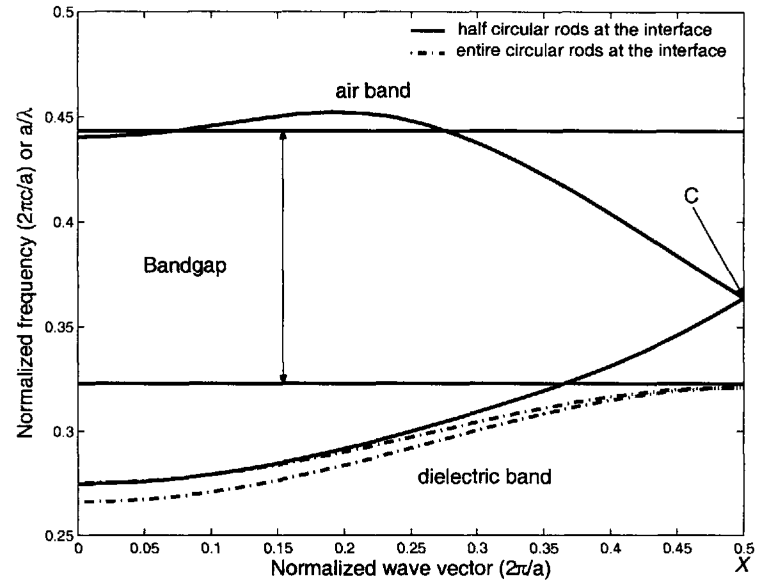

Figure 2-3: Dispersion relation for the sheared photonic crystals when $s = a/2$. Solid line: half circular rods at the interface $h = r$; dash-dot line: entire circular rods at the interface $h = r + a/2$.

effect or the constructive backward coupling [46] since the spatial periodicity of the photonic crystal waveguides is exactly half of the Bloch wavelength at the edge of the first Brillouin zone. In the sheared photonic crystal, the local period along the shear plane is actually $a/2$ instead of a, although the period of the entire structure still equals a. Therefore, the condition for strong backward DBR coupling is broken. Since the local period is decreased to one half of the lattice period, the actual Brillouin zone of guided modes doubles. The mode outside the first Brillouin zone of the entire sheared photonic crystal folds back to form a second mode inside the band gap. Second, as an additional benefit of the absence of flattening, no mode gap exists [44]; guided modes span the entire band gab. Without the problems of limited bandwidth and a large GVD, the sheared photonic crystals are very promising for applications such as high speed transmission, high speed optical signal processing and highly integrated optical circuits.

The very low dispersion of sheared photonic crystals also results in uniform coupling efficiency over the entire width of the band gap. In the FDTD simulation,

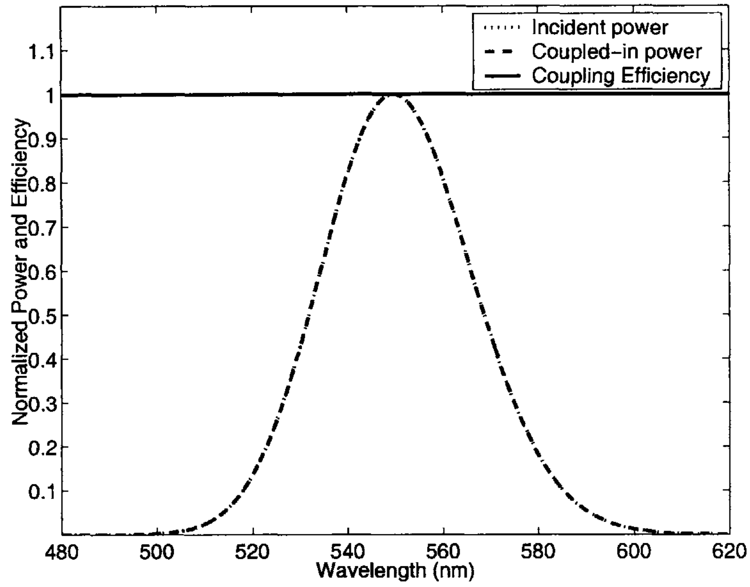

Figure 2-4: Incident power spectrum at Plane A and coupled-in power calculated at Plane B, and coupling efficiency when a 10fs pulse with center wavelength of 550nm is input into the sheared photonic crystal.

we calculated the power coupled into the sheared photonic crystals at Plane B, as shown in Fig. 2-2, which is $5.5\mu m$ away from the end of slab waveguide, Plane A. Then we calculated the coupling efficiency as the ratio of the coupled-in power and incident power at Plane A. Fig. 2-4 shows the spectrum of coupling efficiency when a 10fs pulse is coupled into the shear photonic crystal in Fig. 2-2. The profile of normalized power of incident and coupled-in pulse almost overlap with each other and the coupling efficiency is equal to 1 uniformly for the entire pulse spectrum. In order to obtain the coupling efficiency for the full band gap, we use a 3fs pulse with center wavelength 550nm. The pulse spectrum covers the entire width of the band gap. As shown in Fig. 2-5, the coupling efficiency is uniformly equal to 1 inside the band gap, while some oscillations emerge at the edge of the band gap. The rapid fluctuations of coupling efficiency at the edge of the band gap are not real features of the system and likely to be numerical artifacts [8, 47]. These artifacts arise from the small signal-to-noise ratio outside the band gap and from Gibbs effect inside the band gap.

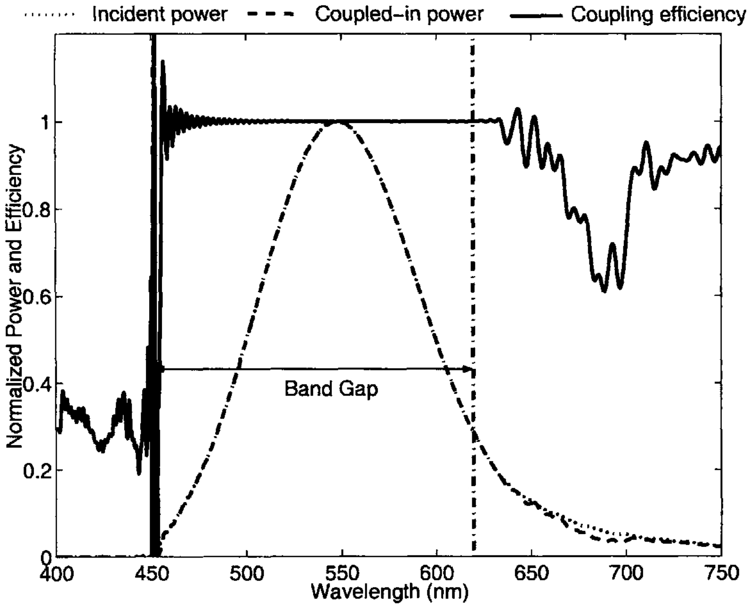

Figure 2-5: Incident power spectrum at Plane A and coupled-in power calculated at Plane B, and coupling efficiency when a 3fs pulse with center wavelength of 550nm is input into the sheared photonic crystal.

2.5 The effect of shear shifts on GVD and group velocity

It can be expected that guiding by shear discontinuities in photonic crystals will depend strongly on the shear shift s between the upper and lower halves of the lattice. The dispersion diagram for shifts other than half lattice constant is shown in Fig. 2-6. We can see that a mode gap opens up progressively towards the band gap edges as the shear shift decreases from half lattice constant to zero. At this point, the presence of the mode gap is also because of DBR. So the dispersion curves are flattened and the mode gap re-emerges. This can also be explained from the symmetry in the Fourier domain as follows. The band diagram must continue symmetrically beyond X. Therefore, when there is no crossing point at X, as in the case of half the lattice constant shear shift, all bands must have zero group velocity (*i.e.* zero slope) at X in order to be analytic functions of the wave vector. Note that sheared photonic

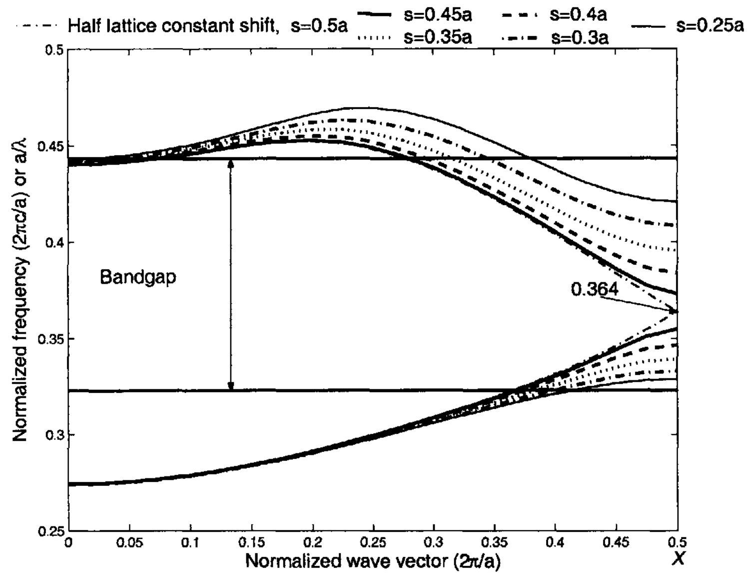

Figure 2-6: Dispersion relation for the sheared photonic crystal with different shear shifts. Half circular rods are at the interface $h = r$.

crystals with shear shift s are actually the same as with shear shift $a - s$ because of the periodicity of the whole structure. So we only consider the case $s < 0.5a$ here. Because no guided modes exist within the frequency range of the mode gap, light of wavelength inside the mode gap can not propagate in sheared photonic crystals. Thus, tunable sheared photonic crystals can be used to implement optical filtering or optical switching. The relationship between the mode gap and shear shift follows Fig. 2-7. Using FDTD simulations, we obtain the spectra of coupling efficiency for different shear shifts, as shown in Fig. 2-8. For wavelengths inside the mode gap, the coupling efficiency decreases to zero. Wavelengths outside the mode gap but inside the band gap retain very high coupling efficiency. The small coupling efficiency near the band edge and outside the band gap result from numerical artifacts in this calculation. Within the band gap, however, the FDTD calculation is very accurate, as can be seen by the excellent match between the mode gap calculated by FDTD and by the dispersion relation(Fig. 2-7).

These phenomenon can also be explained intuitively by the argument of surface waves as follows. The fields in the lower and upper halves of the sheared photonic

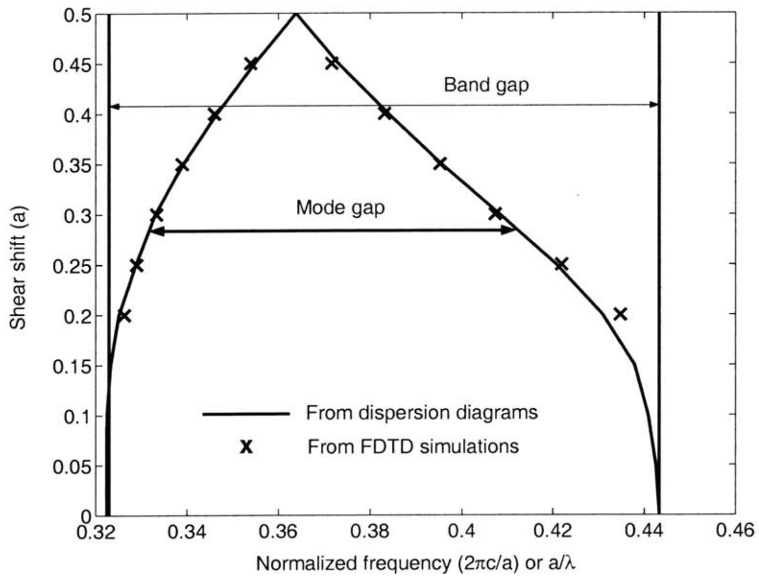

Figure 2-7: Mode gap versus shear shift s of the sheared photonic crystals. Cross symbols indicate the mode gap measured from FDTD simulations.

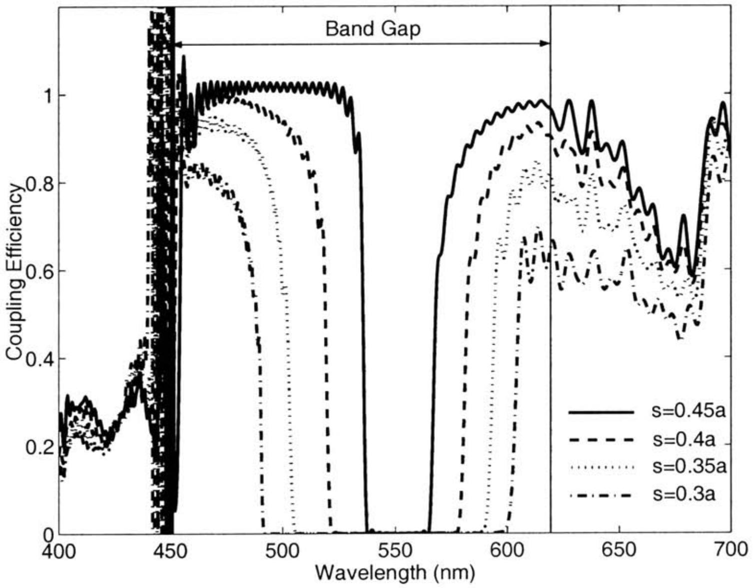

Figure 2-8: Coupling efficiency spectra for different values of shear shift s. 3fs pulses with center wavelength of 550nm are input into the sheared photonic crystals.

crystal can be thought of as surface waves localized at the shear surface. Half lattice constant shear shift will phase match the two Bloch surface waves. They can then strongly couple into each other, resulting in a guided mode that is well confined along the shear plane. When the shear shift is between half lattice constant and zero, the two surface waves are partially phase matched, and so coupling efficiency decreases while mode gaps emerge. When the shear shift is equal to zero (perfect photonic crystal without defect), the two surface waves are totally phase mismatched, and so no wavelengths can propagate within the band gap.

From Fig. 2-6, the slope of the dispersion curves (*i.e.*, the group velocity) also depend on the shear shift. The flattened dispersion curves at the edge of the Brillouin zone result in small group velocities. Thus, the shear photonic crystal structure with mechanically controlled shear shift can be used for active control of the group velocity. Fig. 2-9 shows the group velocity spectra for different shear shifts. The group velocity can be tuned from zero to approximately its value in bulk material with the same averaged index as the sheared photonic crystal, as the shear shift increases. The flattened dispersion curves in Fig. 2-6 are well inside the band gap and isolated from the continuum of modes that lie outside the band gap. This is in contrast with some photonic crystal waveguides which achieve low group velocity near the band edge at the cost of poor field confinement. Our proposed approach is unique in that it utilizes structure to control the group velocity. Tuning via shear does not require special media like cold atomic gases, electronic transitions in crystalline solids or other nonlinear optical effects and electrical heating process [48, 49, 50, 51]. Thus, our approach is applicable at any wavelength range, particularly in the low loss window of optical devices, and independent of operation temperature. Our approach also provides high flexibility because it is decoupled from nonlinear, electro-optic or other effects that are best reserved for other purposes in optical systems.

Fig. 2-6 shows that not only wider mode gaps exist for smaller shear shifts, but also that part of the guided modes for larger shear shifts always fall into the mode gap for smaller shear shifts. This means that bound states can exist [44] whenever a slice of sheared photonic crystal with larger shear shift is sandwiched by two semi-

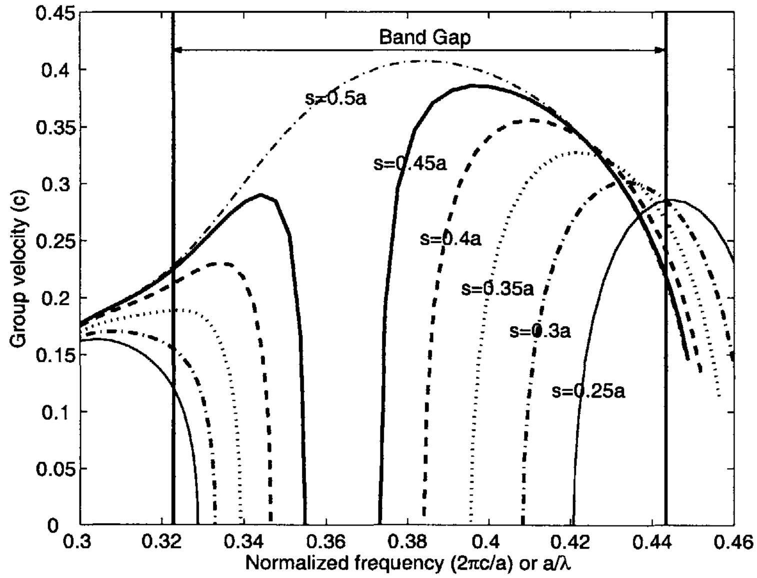

Figure 2-9: Group velocity spectra for different values of shear shift s of the sheared photonic crystals.

infinite sheared photonic crystals with smaller shear shifts. We indeed find a bound state at $\omega = 0.334 \times 2\pi/a$ by choosing a configuration such that a slice of sheared photonic crystal with half lattice constant shift had length $2a$ and was sandwiched by two semi-infinite sheared photonic crystals with quarter lattice constant shift. The electric field for this case is shown in Fig. 2-10. The shear discontinuity is a totally new method to induce bound states instead of changing the width of guiding region in conventional photonic crystal waveguides or metallic waveguides. Actually, in our case, the width of the guiding region does not change at all and also it is easier to find bound states than in conventional waveguides.

2.6 The effect of truncated rod shapes near the interface

The shape of dielectric rods at the interface is also crucial to the presence and properties of the guided modes. The shape of dielectric rods in this thesis is defined by

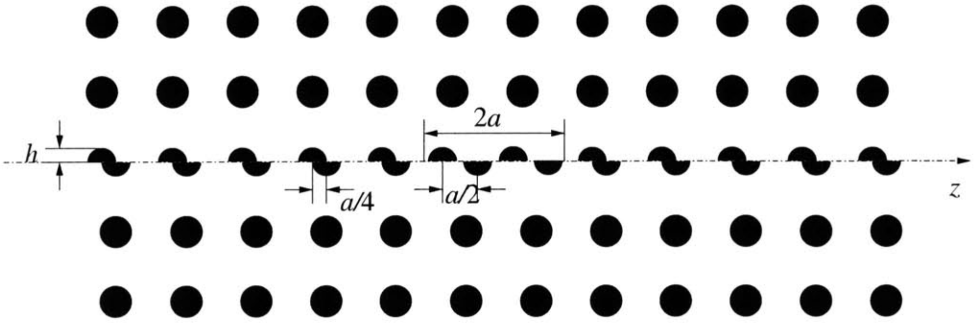

(a)

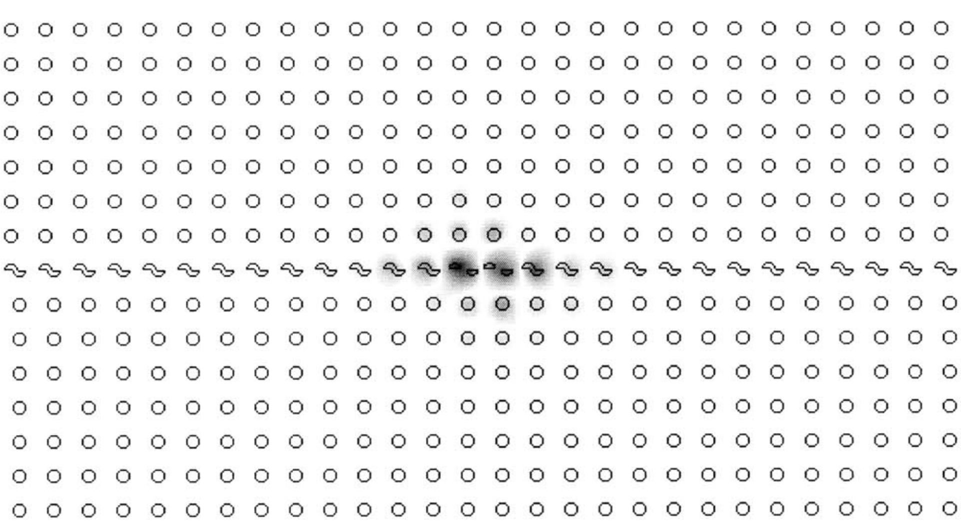

(b)

Figure 2-10: (a) Geometry of a slice of sheared photonic crystal with shear shift $s = a/2$ and thickness $2a$ sandwiched between tow semi-infinite sheared photonic crsytals of $s = a/4$. (b) (Color) Electric field for the bound state at $\omega = 0.334 \times 2\pi/a$ in the geometry shown in (a).

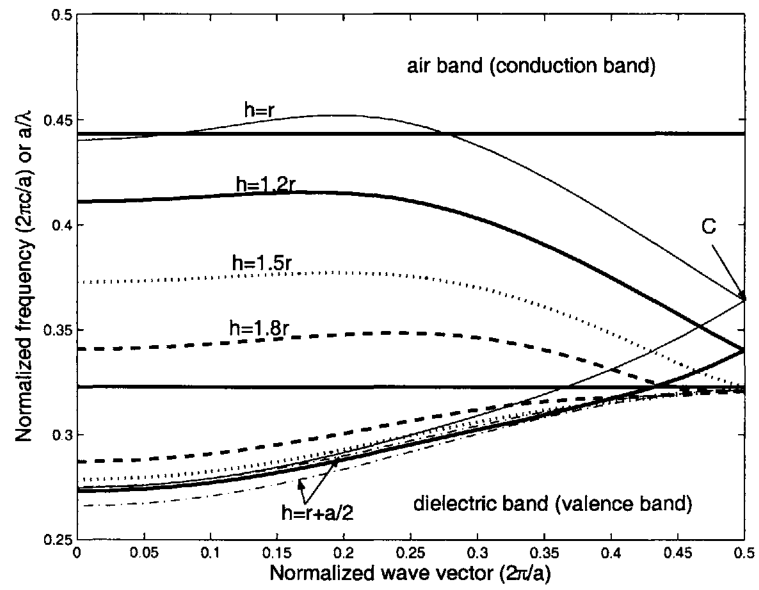

Figure 2-11: Dispersion relations for sheared photonic crystals with different values of h when $s = a/2$. Truncating rods at the interface creates guided modes originated from dielectric band.

the height h: the distance from the top of the circular rods to the shear plane as shown in Fig. 2-1(b). For example, $h = r$ means half circular rods at the interface, while $h = r + a/2$ means that entire circular rods are at the interface and the distance between the centers of circular rods of lower and upper halves near the interface is a. As the dashed line in Fig. 2-3, no guided modes exist inside the band gap when whole rods ($h = r + a/2$) are at the shear interface. The disappearance of guided modes for this case can also be explained by the lack of a surface mode in this geometry [52]. The existence of surface waves for each half of the sheared photonic crystals is a necessary condition for guided modes.

Removing dielectric material resembles adding acceptor atoms in semiconductors [53]. This gives rise to acceptor modes which have their origin at the top of the dielectric (valence) band. So by gradually truncating the rods near the shear plane, we can "pull" the dispersion curves into the band gap, thus creating guided modes that were originally in the dielectric band, as shown in Fig. 2-11.

From Fig. 2-3, we see that point C is actually below the center of the band gap

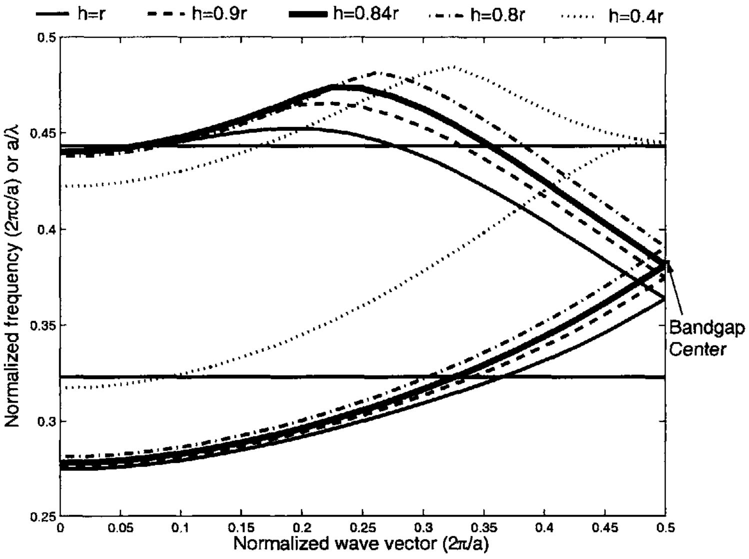

Figure 2-12: Optimization for the dispersion relations with $s = a/2$ and h as optimization parameter.

when $h = r$. So half circular rods at the interface may not fully utilize the advantages of half lattice constant shear shift, and may not achieve the minimum GVD. By truncating the rods at the interface by more than half, we can "pull" the dispersion curves further till the center of the band gap. As shown in Fig. 2-12, when 42% of rods ($s = 0.84r$) left at the interface, point C moves to the center of the band gap. It is worth noting that when only 20% of rods ($s = 0.4r$) is left, guided modes may still have relatively small GVD even though the point C moves out of the band gap. This is understood as follows: the first guided mode occupies the entire band gap although the second guided mode is "pulled" out of the band gap. We calculated the average GVD parameter $\beta_2 = \mathrm{d}^2k/\mathrm{d}\omega^2$ of the guided modes inside the band gap for different heights h, as shown in Fig. 2-13. We can see that guided modes have minimum GVD when the height h is around $0.8r$ and relatively smaller GVD when $h = 0.4r$ than when $h = 0.5r$. The shape of dielectric rods at the interface provides us with another degree of freedom to design and optimize photonic crystal waveguides corresponding to different requirements.

In summary, we have described a new type of waveguide that consists of a shear

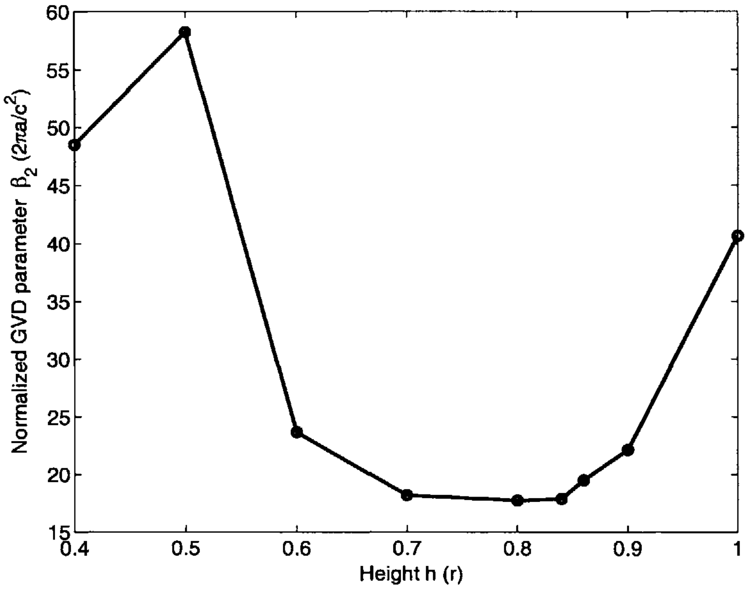

Figure 2-13: Group velocity dispersion parameter β_2 versus h for $s = a/2$.

discontinuity in a photonic crystal. The shear shift was shown to be a design parameter that can be varied to achieve dispersion properties. For example, we can achieve guiding over the entire band gap with minimal GVD by selecting shear shift of half the lattice constant. Alternatively, by changing the shear shift we can tune the mode gap and the group velocity. This type of tuning can be implemented mechanically for dynamic reconfiguration by shearing two plates containing the half lattices relative to each other; or the shear shift may be lithographically defined and fixed to satisfy specific device requirement. In both cases, such devices can be useful for telecommunication and other information processing operations involving large bandwidths. In Chapter 3, we will also present a periodic modification of the shear photonic crystal that can be used as a coupled-resonator optical waveguide (CROW) [54] with tunable group velocity.

Chapter 3

Tunable group velocity in a coupled-resonator optical waveguide (CROW) formed by shear discontinuities in a photonic crystal

3.1 Coupled-resonator optical waveguide (CROW)

In Chapter 2, we discussed photonic crystal waveguides which guide light through Bragg reflection from a periodic structure. Recently a new type of waveguide based on the weak coupling of optical resonators, the coupled-resonator optical waveguides (CROW), was proposed [54]. The CROW consists of a periodic array of defects in a photonic crystal as shown in Fig. 3-1(a). If the resonators' quality factor Q is sufficiently high and the coupling between resonators is sufficiently weak, the photons are well confined in the resonators. Therefore, photons can propagate only by hopping from one resonator to its nearest neighbor. In direct correspondence with the description of electrons in a strong periodic potential in solid state physics, the guided modes of a CROW can be described using the tight binding approximation. A CROW is characterized by a nearly flat sinusoid dispersion relationship and can achieve group velocity smaller by several orders of magnitude than bulk material of the same average refractive index. The guided modes of a CROW are well inside the band gap and isolated from the continuum of modes that lie outside the band gap. This is in contrast with some photonic crystal waveguides which achieve low group velocity at the edge of Brillouin zone or band edge but at the cost of a large group velocity dispersion (GVD) and poor confinement of the fields. The dispersion curve of CROW can be simply characterized by the coupling coefficient κ between nearest resonators (Eq.(5) in Ref. [54]). Similarly, the group velocity is actually linearly proportional to the coupling coefficient κ. The coupling coefficient κ is defined as the overlap of the eigenmodes of two adjacent resonators, so the coupling strength depends on the exponential decay of evanescent waves in the coupling region between resonators. We called this coupling region the evanescent coupling region (ECR). In Fig. 3-1(a), the space between cavities is occupied by a perfect photonic crystal. Because of the periodicity of photonic crystals, the modes of the electromagnetic waves inside can be expanded in Bloch functions defined by their wave vector **k**, as Eq. 2.12. Inside the band gap, there are no solutions to Maxwell's equations for an infinite crystal for any real wave vector **k**. One can only obtain solutions with complex **k**. The imaginary part of complex wave vector **k** is proportional to the difference between the mode frequency and the edge of the band gap [35, 44]. The imaginary part of **k** determines how fast the evanescent waves decay exponentially in ECR.

In Chapter 2, we showed that the shear-type defect supports localized modes. The shear amount controls the mode shape and, hence, a number of mode properties, including mode localization and dispersion. In this chapter, we exploit this property further in a shear-type defect waveguide with additional periodic point defects acting as resonators, as shown in Fig. 3-1(b). We show that by changing the amount of shear shift we can control the coupling between adjacent resonators and, hence, the group velocity. Thus, the shear-type defect provides a means of designing a tunable slow light device. Active control of the speed of a light signal is very important

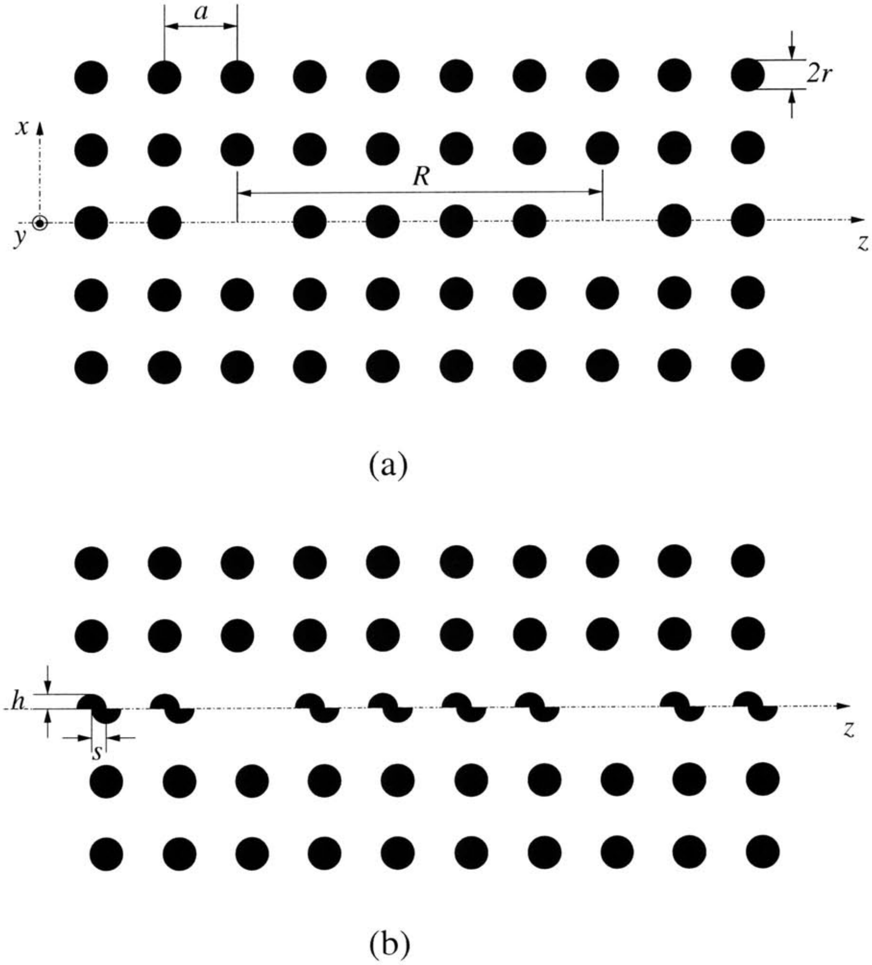

Figure 3-1: (a) Schematic of a CROW with periodicity R consisting of defect cavities embedded in a 2-D photonic crystals with square lattice of dielectric rods in air of lattice constant a and radius $r = 0.2a$. (b) Sheared CROW, with shear shift s and height at the interface h.

to the development of fast access optical memories and optically controlled delay lines in optical communication systems and optical computing. For example, delay-based computing has received attention recently. Our proposed approach is unique in that it utilizes structure to control the group velocity. As in Chapter 2, tuning via shear does not require special media like cold atomic gases [48, 49], electronic transitions in crystalline solids [50] or other nonlinear optical effects. Thus, our approach is applicable at any wavelength range, particularly in the low loss window of optical devices. Our approach also provides high flexibility, e.g. it is decoupled from nonlinear, electro-optic or other effects that could be used in optical systems for other purposes. Because of strong resonant field concentrations and slow group velocity, nonlinear effects can be realized within much lower power and much smaller scale by using CROWs. These enhancements can be further actively controlled by integrating them with the tunable CROWs since nonlinear optical effects usually are proportional to $(1/v_g)^2$ [55]. Thus, active control of harmonic generation, soliton propagation, and stimulated scattering becomes possible. Active control of nonlinear optical processes will have wide applications in many areas, such as lasers, optical communications, and biomedical optics.

3.2 CROW formed by shear discontinuities in photonic crystals

Photonic crystals and photonic crystal waveguides resemble the nearly-free-electron approximation in solid state physics while in the other extreme, a CROW is exactly the optical analog of the tight binding approximation. From Eq.(5) in Ref. [54], the group velocity of a CROW is linearly proportional to the coupling coefficient κ which is defined as the overlap of the eigenmodes of two adjacent resonators,

$$\kappa = \int \mathrm{d}^3\mathbf{r}\, [\epsilon_0 (\mathbf{r} - R\mathbf{e}_z) - \epsilon (\mathbf{r} - R\mathbf{e}_z)] \times \mathbf{E}_\Omega (\mathbf{r}) \cdot \mathbf{E}_\Omega (\mathbf{r} - R\mathbf{e}_z) \tag{3.1}$$

where $\mathbf{E}_\Omega(\mathbf{r})$ is the eigenmode with mode frequency Ω of individual resonators along a straight line parallel to the $\mathbf{e}_z$ axis and the coordinate of the center of the n-th resonator is $z = nR$. $\epsilon_0(\mathbf{r})$ is the dielectric constant of a single resonator while $\epsilon(\mathbf{r})$ is the dielectric constant of the whole CROW. The imaginary part of the wave vector, $\Im\{\mathbf{k}\}$, ($\mathcal{I}\{k\}$) plays a very important role in this integral. The amplitude of $\mathbf{E}_\Omega(\mathbf{r})$ at $z = R$ (the center of $\mathbf{E}_\Omega(\mathbf{r} - R\mathbf{e}_z)$) decays as $\exp[-\Im\{\mathbf{k}\} \cdot (R - a)]$, where $R - a$ is the length of ECR. Therefore, κ is proportional to $\exp[-\Im\{\mathbf{k}\} \cdot (R - a)]$. In turn, the group velocity v_g is proportional to κ, as we mentioned earlier. This implies that v_g in a CROW can be tuned in one of two possible methods. The first method is to adjust the intercavity distance R. The group velocity will decrease (increase) with more (less) spacing between two adjacent resonators [56]. But this adjustment is not continuous: the intercavity distance must be an integer multiple of the lattice constant a. It is also very difficult to change the intercavity spacing once the structure of a CROW is chosen. The second method to control v_g is to adjust the imaginary part of wave vector $\mathbf{k}$, i.e. to change the coupling strength within the ECR. In this section, we will investigate how to use shear discontinuities to change the imaginary part of $\mathbf{k}$, which can give continuous tuning with very simple actuation.

In Chapter 2, we showed that by introducing a shear discontinuity we can modify the band structure of a photonic crystal. When the shear shift is zero (a perfect photonic crystal), the frequency gap equals the band gap. As the shear shift increases, the gap starts to shrink as shown in Fig. 2-7. Because the imaginary part of $\mathbf{k}$ is proportional to the difference from mode frequency to the edge of the gap, we can expect smaller imaginary part of $\mathbf{k}$ with larger shear shift. Therefore, we obtain larger coupling coefficient and larger group velocity, though still much slower than that in bulk material with the same average refractive index. Furthermore, for different shear shifts we have different frequency gaps, resulting in different coupling coefficients and, hence different group velocities. The dependence of frequency gap, coupling coefficient, and group velocity on shear shift constitutes the principle of tunable CROWs presented herein.

First, we compare a CROW using as ECR a perfect photonic crystal ($s = 0$,

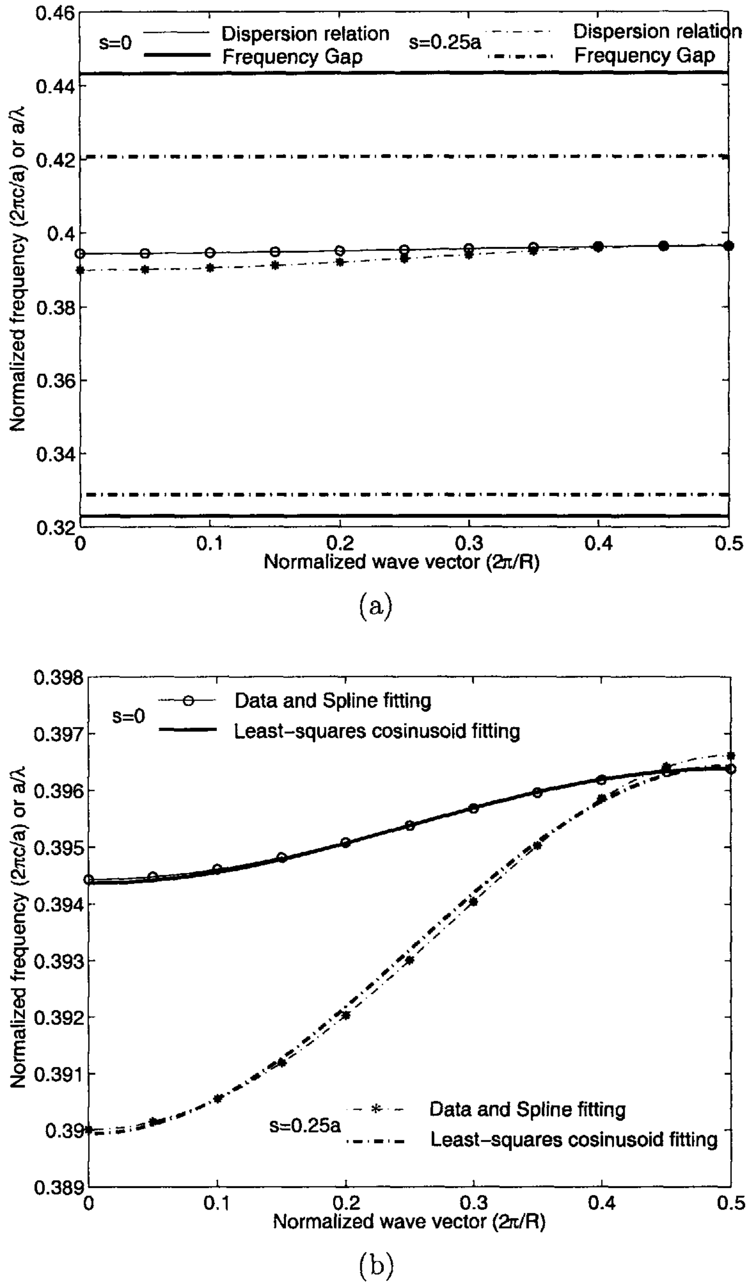

Figure 3-2: (a) Dispersion relations and frequency gaps for CROWs. The intercavity spacing is $R = 5a$ and half circular rods at the interface $h = r$. Thicker lines are frequency gaps while symbols and thinner lines are the data of dispersion relations and their spline fitting. Solid line: $s = 0$, perfect photonic crystal as ECR; dashdot line: $s = 0.25a$, sheared photonic crystal as ECR. (b) Dispersion relations for CROWs with $s = 0$ and $s = 0.25a$. The least-squares fitting are $\omega = 0.395\,[1 - 0.0026\cos(kR)]$ and $\omega = 0.393\,[1 - 0.0083\cos(kR)]$, respectively, for $s = 0$ and $s = 0.25a$.

Fig. 3-1(a)) with a sheared lattice ECR of $s = 0.25a$. In the simulations, we assumed intercavity spacing of 4 rods, $R = 5a$, and half circular rods at the interface, $h = r$. In Fig. 3-2(a), we show the frequency gaps and dispersion curves for the two cases. We can see that the frequency gap is smaller for $s = 0.25a$ and the dispersion curve has larger slope, indicating larger group velocity. Fig. 3-2(b) shows more detail on these dispersion curves. The symbols (circle and star) and the thinner lines (solid and dashdot) show the exact data and a spline fit for each case, respectively. Using the least-squares method, we fit the data to Eq. (5) of Ref.[54] as thicker lines in Fig. 3-2(b), and obtain the coupling coefficient κ. We can see that least-squares fit matches the data and spline fit very well. This indicates that our CROW operates well at the weakly coupled region under the tight binding approximation. For $s = 0$ and $s = 0.25a$, κ is 2.6×10^{-3} and 8.3×10^{-3}, respectively. The corresponding group velocities are $0.0304c$ and $0.103c$, respectively, at $k = 0.5 \times 2\pi/R$ where the CROW systems have zero dispersion and maximum group velocity. CROWs operating at this point have far larger bandwidths than most other slow light devices. (Here, c is the speed of light in the vacuum.) Note that the group velocities were calculated from the direct difference of the data here while least-squares fit also gives very close results, $0.0317c$ and $0.102c$, for $s = 0$ and $s = 0.25a$, respectively. The y-components of the electric field for the eigenstates at $k = 0.5 \times 2\pi/R$ in Fig. 3-3(a) and 3-3(b) illustrate strong confinement in the resonators and evanescent decay in the ECR. To quantify this argument, we calculate the fraction of the electric field energy inside the resonators as 59.5% and 50.5%, respectively, for $s = 0$ and $0.25a$. We can see that the guided field exists primarily inside the resonators, although they have much lower average dielectric constants. The main difference between Fig. 3-3(a) and 3-3(b) is that the mirror symmetry to z-axis in the case of $s = 0$ is broken when $s = 0.25a$. At zero shear shift, the eigenstate is four-fold symmetric and has four symmetry axes (mirror planes) $\mathbf{e}_z$, $\mathbf{e}_x$, $1/\sqrt{2}(\mathbf{e}_x + \mathbf{e}_z)$ and $1/\sqrt{2}(\mathbf{e}_x - \mathbf{e}_z)$ while at $s = 0.25a$ it is only two-fold symmetric and has no mirror symmetry, as expected.

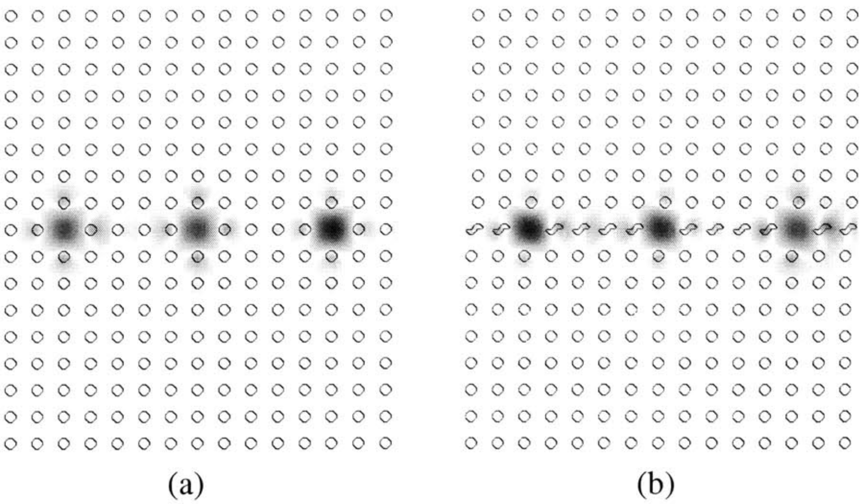
(a) (b)

Figure 3-3: (Color) The electric field y-component for the guided mode of the CROW (a) with $s = 0$ at $k = 0.5 \times 2\pi/R$, (b) with $s = 0.25a$ at $k = 0.5 \times 2\pi/R$

3.3 Tunable group velocity in sheared CROW

When changing the shear shift between the lower and upper halves, we can realize tunable slow light devices. We simulated the dispersion diagram for $s = 0.1a$, $0.15a$, $0.2a$ and $0.25a$ in Fig. 3-4. Circles and thinner lines are the exact data and spline fit while thicker lines are least-squares cosinusoid fit. We can see that smaller shift has better least-squares fit. That is because with smaller shift the evanescent waves decay faster within the ECR. In other words, photons are more tightly confined within each individual resonator, and thus the tight binding approximation holds better. The coupling coefficients and group velocities at $k = 0.5 \times 2\pi/R$ are listed in Table 3.1. The group velocities are calculated from direct difference of the data and least-squares fit. Both methods give very close results. In order to obtain the dependence of the group velocity on the shear shift, we calculated dispersion diagrams for shear shifts ranging from zero to half lattice constant and their corresponding group velocities at $k = 0.5 \times 2\pi/R$. Fig. 3-5 shows quartic dependence of group velocity on shear shift as $v_g = (7.6199s^4 + 0.7188s^2 + 0.0304)c$. We can see that the group velocities obtained from direct difference and least-square fit are very close, and the polynomial fit of the dependence curve also matches very well. The group velocity can be tuned from

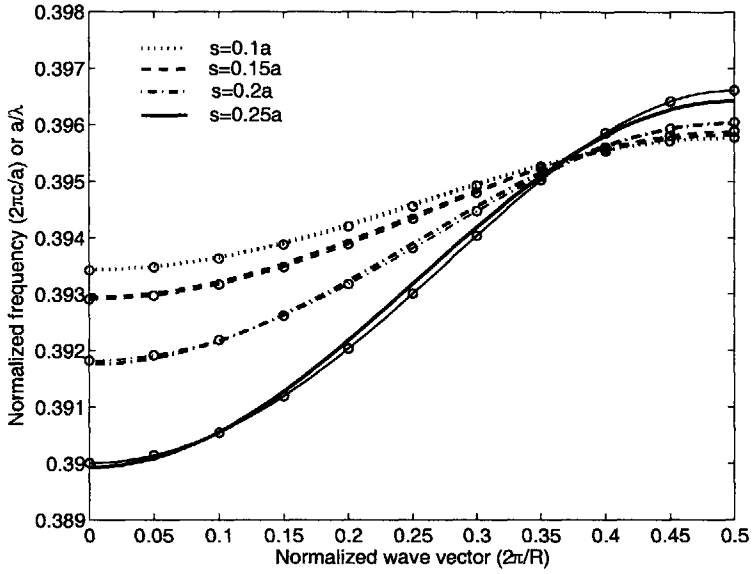

Figure 3-4: The dispersion relations for sheared CROWs with different shear shift s.

Table 3.1: Coupling coefficients and group velocities for sheared CROWs with different shear shifts. The dispersion curves are shown in Fig. 3-4

Shear shift s	Coupling coefficient κ	Group velocity (least-squares fit)	Group velocity (difference)	Group velocity (FDTD)
$0.1a$	3.0×10^{-3}	$0.0367c$	$0.0367c$	$0.0338c$
$0.15a$	3.7×10^{-3}	$0.0466c$	$0.0454c$	$0.0448c$
$0.2a$	5.4×10^{-3}	$0.0661c$	$0.0672c$	$0.0659c$
$0.25a$	8.3×10^{-3}	$0.102c$	$0.103c$	$0.0998c$

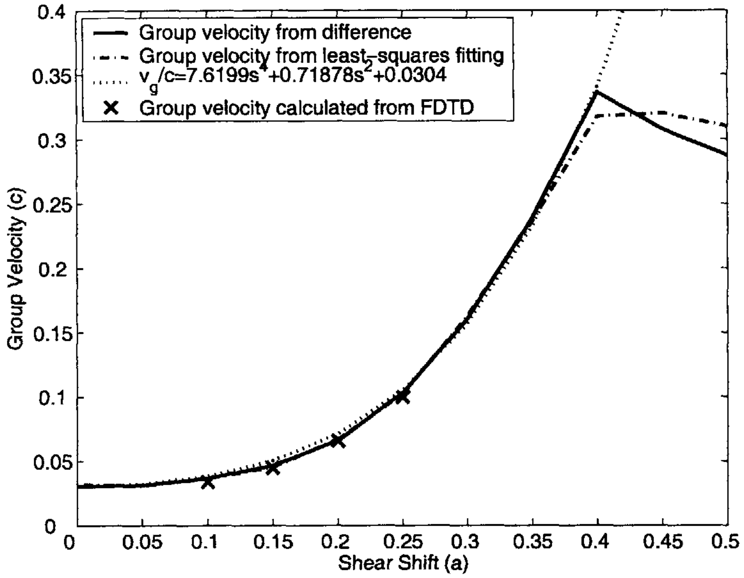

Figure 3-5: Group velocity of guided mode in sheared CROWs versus shear shift s in Fig. 3-1(b).

$0.0304c$ with $s = 0$ to $0.336c$ with $s = 0.4a$. It is worth noting that this range is not the limit of our tunable CROWs. We can achieve tunable range from arbitrarily small group velocity to around that in the bulk material with the same average refractive index when we increase the intercavity distance [56]. Another way is to place one or more side cavities in the neighborhood of each individual resonator in the CROW, as in Fig. 1 in Ref. [57]. The discrepancy at shear shift larger than $0.4a$ is because of the failure of evanescent coupling in ECR. When the shear shift is larger than $0.4a$, the mode gap becomes too small. For sufficiently small gap, the wave vector $\mathbf{k}$ attains real solutions at the mode frequency. There the resonators are coupled by propagating rather than evanescent waves. The light is not well confined in the resonators and coupling among them becomes strong, invalidating the tight binding approximation. This situation looks more like a photonic crystal waveguide than a CROW. This is verified in Fig. 3-6, which depicts the y-component of the electric field corresponding to the eigenstate of the sheared CROW with $s = 0.5a$ at $k = 0.5 \times 2\pi/R$. The lack of light confinement becomes clear upon camparison with Fig. 3-3(a) and 3-3(b). The fraction of the electric field energy in the resonators in Fig. 3-6 is only 28.2%.

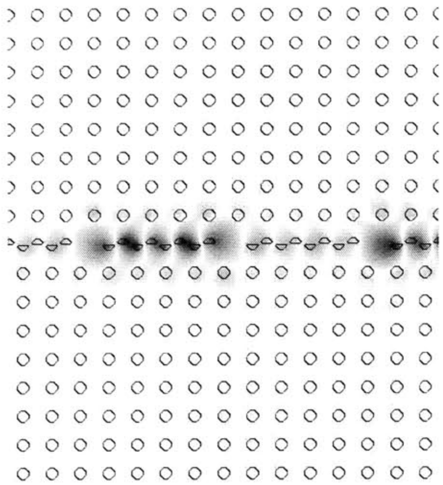

Figure 3-6: (Color) The electric field y-component for the guided mode of the CROW with $s = 0.5a$ at $k = 0.5 \times 2\pi/R$.

We simulated light propagation in tunable CROWs using the FDTD method. We generated a Gaussian pulse with the duration time of $T_0 = 750a/c$ by exciting the first cavity. The spectrum of the pulse is inside the bandwidth of guided modes of the CROW. The group velocities are tuned by changing the shear shift s. As we have observed earlier, the electric field is concentrated in the resonators. From the snapshots at $t = 3850a/c$, we can see that the pulse in a tunable CROW with $s = 0.1a$ [Fig. 3-7(a)] propagates obviously slower than the case of a tunable CROW with $s = 0.2a$ [Fig. 3-7(b)]. The peak of the electric field is at 12th cavity and 21st cavity for the tunable CROWs with $s = 0.1a$ and $s = 0.2a$, respectively. Another indication of the group velocity is the spatial duration of the pulse in tunable CROWs. Since the spatial duration $L_0 = T_0 v_g$, the length of the pulse is linearly proportional to the group velocity. In Fig. 3-7, it is obvious that the pulse is shorter in length in the tunable CROW with $s = 0.1a$ than with $s = 0.2a$. The pulse shapes as functions of time in the first cavity (Plane A in Fig. 3-7) and the twelfth cavity (Plane B in Fig. 3-7) for CROWs with different shear shifts, $s = 0.1a$, $0.15a$, $0.2a$ and $0.25a$, are plotted in Fig. 3-8, where the pulses propagate through the CROWs at different speeds according to the shear shifts. The group velocities can be calculated from

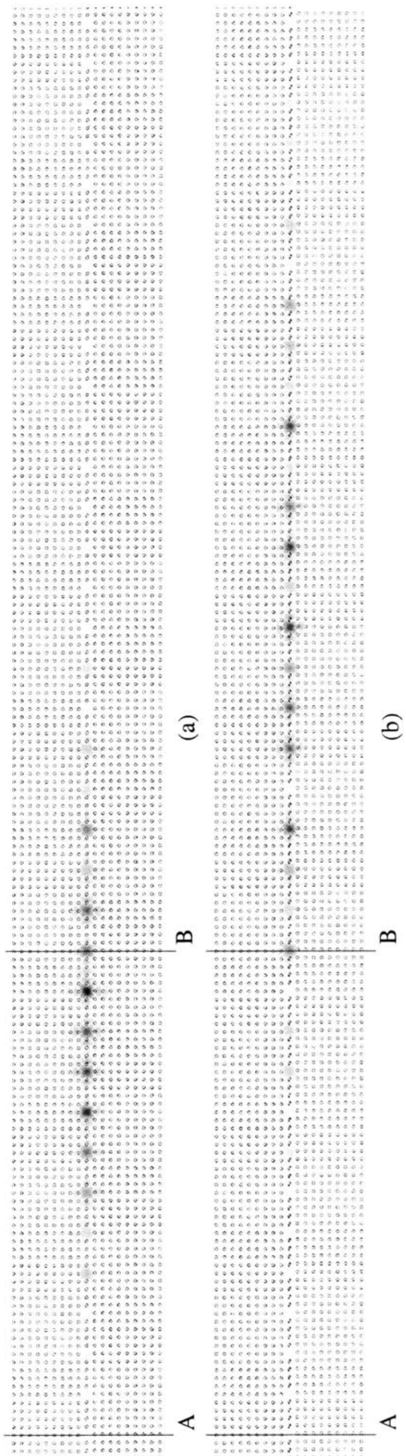

Figure 3-7: (Color) Snapshots of the electric field in tunable CROWs at $t = 3850a/c$. Gaussian pulses propagate inside tunable CROWs (a) with $s = 0.1a$ and (b) with $s = 0.2a$. The duration time of the pulses is $750a/c$.

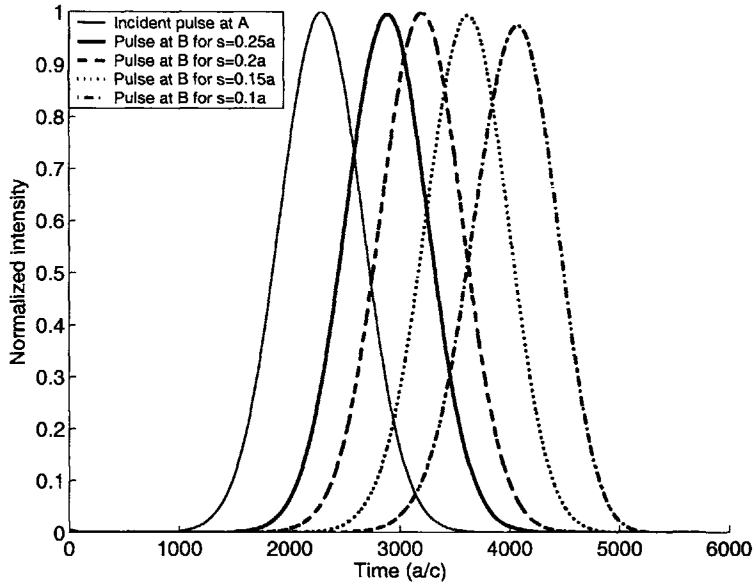

Figure 3-8: The pulse intensities as a function of time recorded in the first cavity (Plane A in Fig. 3-7) and the twelfth cavity (Plane B in Fig. 3-7) for CROWs with different shear shifts.

the propagation of the peaks of these pulses. The results are listed in Table 3.1 and labeled as Crossing symbols in Figure 3-5. They match very well with the dependence curve of group velocity on the shear shift. Thus, our FDTD simulations demonstrate the ability to tune group velocity using CROWs with shear discontinuities in good agreement with the earlier prediction from dispersion diagrams.

In summary, we have designed a tunable slow light device based on a CROW with a mechanically adjustable shear discontinuity to realize active control of the group velocity of light. Tuning ranges from arbitrarily small group velocity to approximately the value of group velocity in the bulk material with the same average refractive index. By combining the ideas of tunable CROW and bound states in sheared photonic crystals that we discussed in Chapter 2, we can furthermore stop and store the light coherently by engineering only the structure. The group velocity tuning capability holds promise for optical communications and quantum information processing. We can even optimize the group velocity, GVD and other properties of tunable CROWs by changing the shape of circular rods (height h in Fig. 3-1(b)) at the shear interface, as in Chapter 2.

Chapter 4

Crosstalk in resonant holographic memories and mode multiplexing with Hermite-Gaussian references

4.1 Fundamental theory of volume holography

Volume holograms are recorded by exposing thick photosensitive media to the interference between two mutually coherent beams, the signal and the reference (Fig. 4-1). The signal carries the information that we want to store and usually has a complicated wavefront, while the reference wavefront is relatively simple, usually a plane wave or spherical wave, carrying the index of the stored information. During the readout process, when the probe beam is the same as the reference beam, strong reconstructed diffraction can be obtained from the hologram (Bragg match). If, however, the plane-wave probe beam deviates in angle or the spherical-wave probe beam shifts in position or the wavelength is different in both plane-wave and spherical wave cases, then diffraction from different parts of the hologram becomes phase mismatched causing the diffraction efficiency to drop (Bragg mismatch). The amount by which the angle or shift or wavelength need to change before the reconstruction power drops to zero is Bragg selectivity and depends on the geometry and thickness of the material.

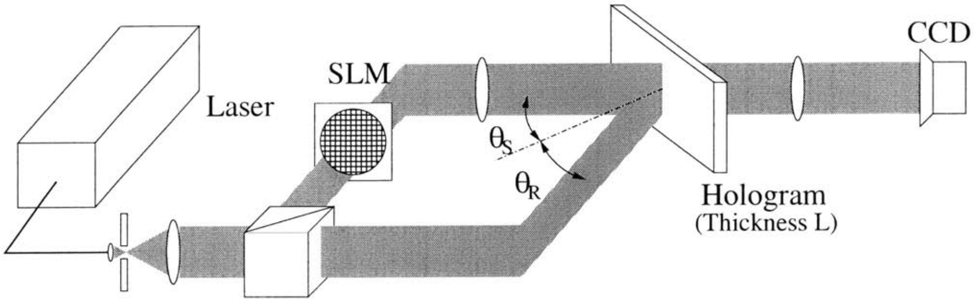

Figure 4-1: Volume holography

We use the plane-wave transmission geometry of Fig. 4-1, a very common setup for holographic storage, as an example to introduce the fundamental theory of volume holography. The plane-wave reference $E_{\mathrm{R}}(\mathbf{r})$ is incident at angle θ_{R} and the signal beam $E_{\mathrm{S}}(\mathbf{r})$ at θ_{S} on the thick volume hologram. They are both at wavelength λ_{R}. The hologram is recorded as modulation of the material dielectric constant, resulting from exposure to the interference pattern between the signal and reference beams. We assume the modulation $\Delta\epsilon$ is weak compared to the material dielectric constant ϵ and proportional to the intensity (interference pattern). In the example of Fig. 4-1, we have a plane-wave object so that

$$E_{\mathrm{R}}(\mathbf{r}) = \exp\{i\mathbf{k}_{\mathrm{R}} \cdot \mathbf{r}\}, \mathbf{k}_{\mathrm{R}} = \frac{2\pi}{\lambda}(-\sin\theta_{\mathrm{R}}, 0, \cos\theta_{\mathrm{R}}), \tag{4.1}$$

$$E_{\mathrm{S}}(\mathbf{r}) = \exp\{i\mathbf{k}_{\mathrm{S}} \cdot \mathbf{r}\}, \mathbf{k}_{\mathrm{S}} = \frac{2\pi}{\lambda}(\sin\theta_{\mathrm{S}}, 0, \cos\theta_{\mathrm{S}}), \tag{4.2}$$

Here, $\mathbf{r} \equiv (x, y, z)$ is the position vector with respect to a coordinate system centered at the hologram and we assume that reference and signal beams have the same polarization. Without loss of generality, we have assumed that the reference and signal beams are in the x–z plane. Thus, the modulation can be expressed as

$$\Delta\epsilon(\mathbf{r}) = \epsilon_1 |E_{\mathrm{R}}(\mathbf{r}) + E_{\mathrm{S}}(\mathbf{r})|^2 = 2\epsilon_1 \{1 + \cos(\mathbf{K}_g \cdot \mathbf{r})\}, \tag{4.3}$$

where $\mathbf{K}_g = \mathbf{k}_{\mathrm{S}} - \mathbf{k}_{\mathrm{R}}$ is the grating vector of the volume hologram and ϵ_1 denotes the strength of the hologram. Further, Eq. 4.3 can be written as

$$\Delta\epsilon\left(\mathbf{r}\right)=2\epsilon_1\left\{1+\cos\left[\left(\sin\theta_{\mathrm{S}}+\cos\theta_{\mathrm{R}}\right)\frac{2\pi x}{\lambda}+\left(\cos\theta_{\mathrm{S}}-\cos\theta_{\mathrm{R}}\right)\frac{2\pi z}{\lambda}\right]\right\}. \tag{4.4}$$

Eq. 4.4 can be divided into three terms as follows:

$$\Delta\epsilon\left(\mathbf{r}\right)=\Delta\epsilon_0(\mathbf{r})+\Delta\tilde{\epsilon}(\mathbf{r})+\Delta\tilde{\epsilon}^*(\mathbf{r}), \tag{4.5}$$

$$\Delta\epsilon_0(\mathbf{r})=2\epsilon_1, \tag{4.6}$$

$$\Delta\tilde{\epsilon}(\mathbf{r})=\epsilon_1\exp\left\{i\mathbf{K}_g\cdot\mathbf{r}\right\}. \tag{4.7}$$

In Eqs. 4.3– 4.5, $\Delta\epsilon_0(\mathbf{r})$ is the constant term and much smaller than ϵ; $\Delta\tilde{\epsilon}(\mathbf{r})$ leads to forward diffraction, and $\Delta\tilde{\epsilon}^*(\mathbf{r})$ leads to the phase-conjugate diffraction. Since $\Delta\epsilon_0(\mathbf{r})$ and $\Delta\tilde{\epsilon}^*(\mathbf{r})$ do not contribute significantly to the forward diffracted field, we only maintain $\Delta\tilde{\epsilon}(\mathbf{r})$ and simplify the notation as $\Delta\epsilon(\mathbf{r})$:

$$\Delta\epsilon(\mathbf{r})=\epsilon_1\exp\left\{i\left[\left(\sin\theta_{\mathrm{S}}+\sin\theta_{\mathrm{R}}\right)\frac{2\pi x}{\lambda}+\left(\cos\theta_{\mathrm{S}}-\cos\theta_{\mathrm{R}}\right)\frac{2\pi z}{\lambda}\right]\right\}. \tag{4.8}$$

Furthermore, Eq. 4.8 can also be expressed as

$$\Delta\epsilon(\mathbf{r})=\epsilon_1 E_R(\mathbf{r})^* E_S(\mathbf{r}). \tag{4.9}$$

where $*$ denotes complex conjugate.

The reconstruction of the recorded hologram is posed as the problem of diffraction from the modulation $\Delta\epsilon(\mathbf{r})$ upon illumination by a probe beam $E_{\mathrm{p}}(\mathbf{r})$ (possibly different than $E_{\mathrm{R}}(\mathbf{r})$). This problem admits analytical solution under the Born and paraxial approximations. The diffracted field $E_{\mathrm{d}}(\mathbf{r}'')$ just after the hologram is given approximately by the first order Born approximation as

$$E_{\mathrm{d}}(\mathbf{r}'')=\iiint E_{\mathrm{p}}(\mathbf{r})\Delta\epsilon(\mathbf{r})V(\mathbf{r})G(\mathbf{r}''-\mathbf{r})\mathrm{d}^3\mathbf{r}, \tag{4.10}$$

where $G(\mathbf{r})$ is Green's function for free space, $\mathbf{r}''\equiv(x'',y'')$ is the position vector on the exit face of the volume hologram and $V(\mathbf{r})$ is the index function of the holographic material, defined as

$$V(\mathbf{r}) = \begin{cases} 1 & \text{inside volume hologram} \\ 0 & \text{outside volume hologram} \end{cases}. \tag{4.11}$$

The integral 4.10 can be interpreted as follows: each infinitesimal region inside the hologram acts as a point source while the diffracted field is obtained as the coherent superposition of all the fields emitted by these the infinitesimal point-sources. Under the paraxial approximation, the Green's function can be simplified as

$$G(\mathbf{r}'' - \mathbf{r}) = \frac{1}{i\lambda(z'' - z)} \exp\left\{ i2\pi \frac{z'' - z}{\lambda} + i\pi \frac{(x'' - x)^2 + (y'' - y)^2}{\lambda(z'' - z)} \right\} \tag{4.12}$$

Substituting Eqs. 4.8, 4.12 and the expression of the probe beam

$$E_{\mathrm{p}}(\mathbf{r}) = \exp\left\{ i\frac{2\pi}{\lambda} \left(-\sin\theta_{\mathrm{p}} x + \cos\theta_{\mathrm{p}} z \right) \right\}, \tag{4.13}$$

into Eq. 4.10, assuming that the dimensions of the volume hologram are infinite in the x– and y–directions and the thickness of the volume hologram is L as well as neglecting the constant ϵ_1 and $1/\lambda(z'' - z)$ term which is slowly varying comparing to the exponential terms, we finally obtain

$$\begin{aligned} E_{\mathrm{d}}(\mathbf{r}'') \;=\; & \iiint \operatorname{rect}\left(\frac{z}{L}\right) \exp\left\{ i\frac{2\pi}{\lambda} \left(-\sin\theta_{\mathrm{p}} x + \cos\theta_{\mathrm{p}} z \right) \right\} \\ & \exp\left\{ i \left[\left(\sin\theta_{\mathrm{S}} + \sin\theta_{\mathrm{R}} \right) \frac{2\pi x}{\lambda} + \left(\cos\theta_{\mathrm{S}} - \cos\theta_{\mathrm{R}} \right) \frac{2\pi z}{\lambda} \right] \right\} \\ & \exp\left\{ i2\pi \frac{z'' - z}{\lambda} + i\pi \frac{(x'' - x)^2 + (y'' - y)^2}{\lambda(z'' - z)} \right\} \mathrm{d}x\mathrm{d}y\mathrm{d}z, \end{aligned} \tag{4.14}$$

The x any y integrals are readily obtained using the following lemma from complex analysis:

$$\int_{-\infty}^{\infty} \exp[i(ax^2 + bx)]\mathrm{d}x = \operatorname{sgn}(a) i \sqrt{\frac{\pi}{|a|}} \exp\left[\frac{b^2}{4a}\right] \tag{4.15}$$

for a and b real, and $a \neq 0$. Then by neglecting the constants, the resulting z integral yields

$$\begin{aligned}
E_{\mathrm{d}}(\mathbf{r}'') = {} & \exp\left\{ i\frac{2\pi}{\lambda}\left(\sin\theta_{\mathrm{S}} + \sin\theta_{\mathrm{R}} - \sin\theta_{\mathrm{p}}\right)x'' + \right. \\
& \left. i\frac{2\pi}{\lambda}z''\left[1 - \frac{1}{2}\left(\sin\theta_{\mathrm{S}} + \sin\theta_{\mathrm{R}} - \sin\theta_{\mathrm{p}}\right)^2\right]\right\} \\
& \int \mathrm{rect}\left(\frac{z}{L}\right)\exp\left\{ i\frac{2\pi}{\lambda}z\left(\cos\theta_{\mathrm{S}} - \cos\theta_{\mathrm{R}} + \cos\theta_{\mathrm{p}}\right)\right\} \\
& \exp\left\{ -i\frac{2\pi}{\lambda}z\left[1 - \frac{1}{2}\left(\sin\theta_{\mathrm{S}} + \sin\theta_{\mathrm{R}} - \sin\theta_{\mathrm{p}}\right)^2\right]\right\}\mathrm{d}z \\
= {} & \exp\left\{ i\frac{2\pi}{\lambda}\left(\sin\theta_{\mathrm{S}} + \sin\theta_{\mathrm{R}} - \sin\theta_{\mathrm{p}}\right)x'' + \right. \\
& \left. i\frac{2\pi}{\lambda}z''\left[1 - \frac{1}{2}\left(\sin\theta_{\mathrm{S}} + \sin\theta_{\mathrm{R}} - \sin\theta_{\mathrm{p}}\right)^2\right]\right\} \\
& \mathrm{sinc}\left\{ \frac{L}{\lambda}\left[\left(\cos\theta_{\mathrm{S}} - \cos\theta_{\mathrm{R}} + \cos\theta_{\mathrm{p}}\right) + \right.\right. \\
& \left.\left.\left(1 - \frac{1}{2}\left(\sin\theta_{\mathrm{S}} + \sin\theta_{\mathrm{R}} - \sin\theta_{\mathrm{p}}\right)^2\right)\right]\right\}. \qquad (4.16)
\end{aligned}$$

Expressing Eq. 4.16 with $\mathbf{K}_g$ and $\mathbf{k}_{\mathrm{p}}$ and retrieving the paraxial approximation, we can obtain a more simplified form:

$$\begin{aligned}
E_{\mathrm{d}}(\mathbf{r}'') = {} & \exp\left\{ i\left[\left(K_{\mathrm{gx}} + k_{\mathrm{px}}\right)x'' + \sqrt{k^2 - \left(K_{\mathrm{gx}} + k_{\mathrm{px}}\right)^2}\right]\right\} \\
& \mathrm{sinc}\left\{ \frac{L}{2\pi}\left[K_{\mathrm{gz}} + k_{\mathrm{pz}} - \sqrt{k^2 - \left(K_{\mathrm{gx}} + k_{\mathrm{px}}\right)^2}\right]\right\}. \qquad (4.17)
\end{aligned}$$

From Eq. 4.17, we can find that the diffracted wave-vector $\mathbf{k}_{\mathrm{d}}$ is determined by the following conditions:

$$\mathbf{k}_{\mathrm{d}} \times \hat{\mathbf{z}} = \left(\mathbf{k}_{\mathrm{p}} + \mathbf{K}_g\right) \times \hat{\mathbf{z}}, \qquad (4.18)$$

$$|\mathbf{k}_{\mathrm{d}}| = \frac{2\pi}{\lambda}, \qquad (4.19)$$

where $\hat{\mathbf{z}}$ is the unit vector in the z–direction. The diffraction efficiency is proportional the sinc-function in Eqs. 4.16 and 4.17,

$$\left|\frac{\mathbf{E}_{\mathrm{d}}}{\mathbf{E}_{\mathrm{p}}}\right|^2 = \eta_1 \mathrm{sinc}^2\left(\frac{L\delta\mathbf{k}_{\mathrm{d}} \cdot \hat{\mathbf{z}}}{2\pi}\right) \qquad (4.20)$$

where η_1 is Bragg-matched single pass diffraction efficiency and proportional to the strength of hologram ϵ_1. The quantity

$$\delta \mathbf{k}_{\mathrm{d}} = \mathbf{K}_g + \mathbf{k}_{\mathrm{p}} - \mathbf{k}_{\mathrm{d}} \tag{4.21}$$

is referred to as "Bragg-mismatch." If $\delta \mathbf{k}_{\mathrm{d}} = 0$, the hologram is "Bragg-matched," and the diffraction efficiency is maximum. When $\delta \mathbf{k}_{\mathrm{d}} \neq 0$, the diffraction efficiency drops according to the sinc-function of Eq. 4.16 and 4.17. The amount that $\mathbf{k}_{\mathrm{p}}$ needs to change from its "Bragg-match" condition before the sinc-function reaches its first null is called "Bragg selectivity". For example, the Bragg selectivity for angle change of the probe beam, or "angular Bragg selectivity", can be obtained from Eq. 4.16 as

$$(\Delta\theta)_{\mathrm{B}} = m\frac{\lambda \cos\theta_{\mathrm{S}}}{L \sin(\theta_{\mathrm{R}} + \theta_{\mathrm{S}})}, \quad m = 1, 2, ... \tag{4.22}$$

This means that the crosstalk between the two holograms is minimal when $\Delta\theta_{\mathrm{p}}$ equals the Bragg selectivity.

If the probe beam has different wavelength than the recording signal and reference, we obtain the wavelength selectivity. In this case, the expression for the probe beam is

$$E_{\mathrm{p}}(\mathbf{r}) = \exp\left\{ i\frac{2\pi}{\lambda_{\mathrm{p}}}\left(-\sin\theta_{\mathrm{p}} x + \cos\theta_{\mathrm{p}} z\right)\right\}, \tag{4.23}$$

The integral for diffracted field can be obtained as

$$\begin{aligned} E_{\mathrm{d}}(\mathbf{r}'') \ &= \ \iiint \mathrm{rect}(\frac{z}{L}) \exp\left\{ i\frac{2\pi}{\lambda_{\mathrm{p}}}\left(-\sin\theta_{\mathrm{p}} x + \cos\theta_{\mathrm{p}} z\right)\right\} \\ &\quad \exp\left\{ i\left[(\sin\theta_{\mathrm{S}} + \sin\theta_{\mathrm{R}})\frac{2\pi x}{\lambda} + (\cos\theta_{\mathrm{S}} - \cos\theta_{\mathrm{R}})\frac{2\pi z}{\lambda}\right]\right\} \\ &\quad \exp\left\{ i2\pi\frac{z'' - z}{\lambda_{\mathrm{p}}} + i\pi\frac{(x'' - x)^2 + (y'' - y)^2}{\lambda_{\mathrm{p}}(z'' - z)}\right\} \mathrm{d}x\mathrm{d}y\mathrm{d}z, \end{aligned} \tag{4.24}$$

By assuming that the dimensions of the volume hologram are infinite in the $x-$ and

y-directions and using lemma 4.15, we obtain the explicit expression

$$\begin{aligned}
E_{\rm d}(\mathbf{r}'') &= \exp\left\{ i\frac{2\pi}{\lambda_{\rm p}}\left(\frac{\lambda_{\rm p}}{\lambda}\sin\theta_{\rm S} + \frac{\lambda_{\rm p}}{\lambda}\sin\theta_{\rm R} - \sin\theta_{\rm p}\right)x'' + \right. \\
&\left. i\frac{2\pi}{\lambda_{\rm p}}z''\left[1 - \frac{1}{2}\left(\frac{\lambda_{\rm p}}{\lambda}\sin\theta_{\rm S} + \frac{\lambda_{\rm p}}{\lambda}\sin\theta_{\rm R} - \sin\theta_{\rm p}\right)^2\right]\right\} \\
&\int \mathrm{rect}\left(\frac{z}{L}\right)\exp\left\{i\frac{2\pi}{\lambda_{\rm p}}z\left(\frac{\lambda_{\rm p}}{\lambda}\cos\theta_{\rm S} - \frac{\lambda_{\rm p}}{\lambda}\cos\theta_{\rm R} + \cos\theta_{\rm p}\right)\right\} \\
&\exp\left\{-i\frac{2\pi}{\lambda_{\rm p}}z\left[1 - \frac{1}{2}\left(\frac{\lambda_{\rm p}}{\lambda}\sin\theta_{\rm S} + \frac{\lambda_{\rm p}}{\lambda}\sin\theta_{\rm R} - \sin\theta_{\rm p}\right)^2\right]\right\}\mathrm{d}z \\
&= \exp\left\{ i\frac{2\pi}{\lambda_{\rm p}}\left(\frac{\lambda_{\rm p}}{\lambda}\sin\theta_{\rm S} + \frac{\lambda_{\rm p}}{\lambda}\sin\theta_{\rm R} - \sin\theta_{\rm p}\right)x'' + \right. \\
&\left. i\frac{2\pi}{\lambda_{\rm p}}z''\left[1 - \frac{1}{2}\left(\frac{\lambda_{\rm p}}{\lambda}\sin\theta_{\rm S} + \frac{\lambda_{\rm p}}{\lambda}\sin\theta_{\rm R} - \sin\theta_{\rm p}\right)^2\right]\right\} \\
&\mathrm{sinc}\left\{\frac{L}{\lambda_{\rm p}}\left[\left(\frac{\lambda_{\rm p}}{\lambda}\cos\theta_{\rm S} - \frac{\lambda_{\rm p}}{\lambda}\cos\theta_{\rm R} + \cos\theta_{\rm p}\right) + \right.\right. \\
&\left.\left.\left(1 - \frac{1}{2}\left(\frac{\lambda_{\rm p}}{\lambda}\sin\theta_{\rm S} + \frac{\lambda_{\rm p}}{\lambda}\sin\theta_{\rm R} - \sin\theta_{\rm p}\right)^2\right)\right]\right\}. \qquad (4.25)
\end{aligned}$$

Eq. 4.24 can be expressed in the same form as Eq. 4.17 only by replacing k with $k_{\rm p}$:

$$\begin{aligned}
E_{\rm d}(\mathbf{r}'') &= \exp\left\{i\left[(K_{\rm gx} + k_{\rm px})\,x'' + \sqrt{k_{\rm p}^2 - (K_{\rm gx} + k_{\rm px})^2}\right]\right\} \\
&\mathrm{sinc}\left\{\frac{L}{2\pi}\left[K_{\rm gz} + k_{\rm pz} - \sqrt{k_{\rm p}^2 - (K_{\rm gx} + k_{\rm px})^2}\right]\right\}. \qquad (4.26)
\end{aligned}$$

The more general condition for diffracted wave-vector $\mathbf{k}_{\rm d}$ is, therefore:

$$\mathbf{k}_{\rm d} \times \hat{\mathbf{z}} = (\mathbf{k}_{\rm p} + \mathbf{K}_g) \times \hat{\mathbf{z}} \qquad (4.27)$$

$$|\mathbf{k}_{\rm d}| = k_{\rm p} = \frac{2\pi}{\lambda_{\rm p}} \qquad (4.28)$$

Thus, from Eqs. 4.17 and 4.26, an equivalent expression for the Bragg matching condition ($\delta\mathbf{k}_{\rm d} = 0$) can be obtained as

$$|\mathbf{K}_g + \mathbf{k}_{\rm p}| = k_{\rm p} = \frac{2\pi}{\lambda_{\rm p}} \qquad (4.29)$$

The K-sphere interpretation of this condition is shown in Fig. 4-2 : the ending point of the vector $\mathbf{K}_g + \mathbf{k}_\mathrm{p}$ is on the surface of the K-sphere with radius k_p. From Eq. 4.24, we can obtain the wavelength Bragg selectivity as

$$(\Delta\lambda)_\mathrm{B} = m\frac{\lambda^2 \cos\theta_\mathrm{S}}{2L\sin^2\frac{1}{2}(\theta_\mathrm{R}+\theta_\mathrm{S})}, \quad m = 1, 2, ... \tag{4.30}$$

In volume holography, the Bragg selectivity effect is used to record multiple overlapping holograms sharing the same material volume. This process is referred as "hologram multiplexing." In this section, multiplexing is achieved by changing the angle and wavelength of the reference beam by an amount equal to the respective selectivities. When the reference beam is spherical wave, shift multiplexing [58, 59] is achieved by changing the position of the focal point of the spherical wave.

4.2 Crosstalk in volume holographic storage

Holographic memories are particularly suitable for applications that demand high data capacity, high transfer rate and the presence of both direct and associative recall. In volume holographic storage, a large number of holograms are stored in the same material volume. Therefore, crosstalk is an important issue for data retrieval.

Here we derive the diffraction efficiency of crosstalk noise with angle multiplexing. We consider the Fourier-plane geometry of Fig. 4-3: an object beam containing a page of information is recorded holographically in association with a uniquely oriented reference beam (as the index of the page of information) in the recording medium. The procedure is repeated with different sets of object and reference beams to yield a volume holographic memory in which any particular page of information can be uniquely accessed by reading out the hologram with the corresponding reference beam. Even though the recorded data share the same volume, each page can be retrieved independently with reasonable fidelity because of the Bragg selectivity of readout. A unique benefit of such a system is the parallel nature of the readout, where a given reference beam can retrieve the whole page of information simultaneously to be

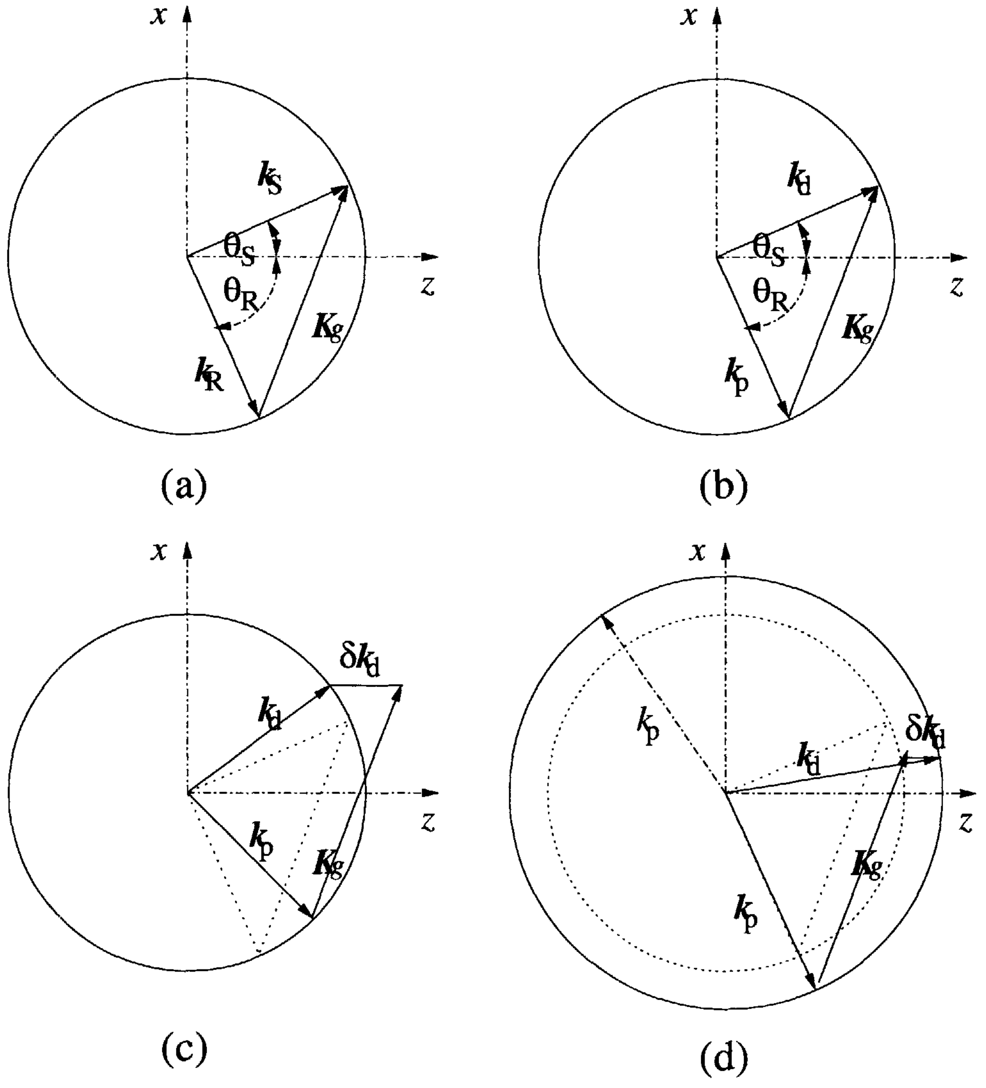

Figure 4-2: Illustration of Bragg-diffraction on the K–sphere: (a) recording of the hologram $\mathbf{K}_g$ by plane waves with wave vectors $\mathbf{k}_\mathrm{S}$ and $\mathbf{k}_\mathrm{R}$; (b) Bragg match condition, $\mathbf{k}_\mathrm{p} = \mathbf{k}_\mathrm{R}$; (c) the probe beam is different than the reference beam in angle; (d) the probe beam is different than the reference beam in wavelength.

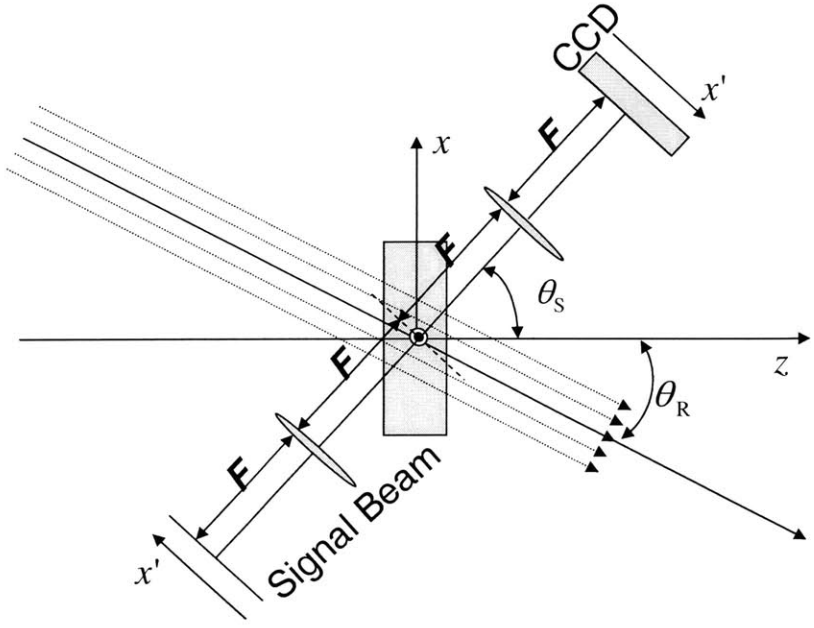

Figure 4-3: Fourier–plane geometry with angle multiplexing

imaged onto a CCD. In the readout process, an image is reconstructed by illuminating the volume with the corresponding reference beam. In an ideal case, no other stored images should be read out by this beam. However, in reality, portions of other stored pages are partially Bragg-matched resulting in crosstalk.

Considering the Fourier–plane geometry in Fig. 4-3, if we use a displaced reference beam with the direction of $\theta_R + \Delta\theta$ to probe the hologram, the selectivity response can be obtained from Eq. 4.20:

$$\eta = \eta_1 \mathrm{sinc}^2 \left(\frac{L}{\lambda} \frac{\sin(\theta_R + \theta_S)}{\cos\theta_S} \Delta\theta \right), \tag{4.31}$$

and the angluar Bragg selectivity is given by Eq. 4.30 which depends on directions of both signal beam and reference beam. In practice, we always choose an initial reference beam, called θ_i, with which the angle Bragg selectivity is calculated, and also serves as the reference beam for the m_i–th hologram.

In the Fourier–plane geometry of Fig. 4-3, pixels with $x' \neq 0$, have different spatial frequencies than the carrier θ_S of the signal beam. The difference $\delta\theta_S$ can be written as

$$\delta\theta_{\mathrm{S}} = \arctan\left(\frac{x'}{F}\right). \tag{4.32}$$

So when the m'–th hologram (whose reference beam direction is $\theta_{m'}$) is reconstructed, the crosstalk noise from the m–th hologram (whose reference beam direction is θ_m) can be obtained as

$$\eta_1^{\mathrm{X}m}(x') = \eta_1 \mathrm{sinc}^2\left\{\frac{L}{\lambda}\frac{\sin\left(\theta_m + \theta_{\mathrm{S}} - \delta\theta_{\mathrm{S}}\right)}{\cos(\theta_{\mathrm{S}} - \delta\theta_{\mathrm{S}})} p(m - m')(\Delta\theta)_{\mathrm{B}}\right\}. \tag{4.33}$$

where, two adjacent holograms are separated by p shift Bragg nulls. Using

$$\frac{\sin\left(\theta_m + \theta_{\mathrm{S}} - \delta\theta_{\mathrm{S}}\right)}{\cos(\theta_{\mathrm{S}} - \delta\theta_{\mathrm{S}})} \approx \frac{\sin\left(\theta_m + \theta_{\mathrm{S}}\right)}{\cos\theta_{\mathrm{S}}} - \cos\theta_m \frac{x'}{F}, \tag{4.34}$$

we find

$$\eta_1^{\mathrm{X}m}(x') = \eta_1 \mathrm{sinc}^2\left\{p(m - m')\left(\frac{\sin\left(\theta_m + \theta_{\mathrm{S}}\right)}{\sin\left(\theta_i + \theta_{\mathrm{S}}\right)} - \frac{\cos\theta_m \cos\theta_{\mathrm{S}}}{\sin\left(\theta_i + \theta_{\mathrm{S}}\right)}\frac{x'}{F}\right)\right\}. \tag{4.35}$$

By adding crosstalk noise from all pages, we obtain the single-pass diffraction efficiency of crosstalk noise as

$$\eta_1^{\mathrm{X}} \approx \eta_1 \sum_{m=1}^{M} \mathrm{sinc}^2\left\{p(m - m')\left(\frac{\sin\left(\theta_m + \theta_{\mathrm{S}}\right)}{\sin\left(\theta_i + \theta_{\mathrm{S}}\right)} - \frac{\cos\theta_m \cos\theta_{\mathrm{S}}}{\sin\left(\theta_i + \theta_{\mathrm{S}}\right)}\frac{x'}{F}\right)\right\}. \tag{4.36}$$

The single-pass crosstalk noise in angle multiplexing is different than the crosstalk noise in shift multiplexing [59], Eq. 4.40, but the difference is very small as shown in Fig. 4-4. Here we assumed that, the same in angle multiplexing and shift multiplexing, 1000 holograms are stored in 1001 shift-multiplexed positions, leaving position 501 blank and the shift separation between two adjacent holograms was equal to 2 angle or shift Bragg nulls. In order to make angle multiplexing and shift multiplexing comparable, we also use the same θ_{S}, and set $\theta_i = 0$ and $m_i = 501$.

In practice, $\theta_i + \theta_{\mathrm{S}} \gg (m - m_i)(\Delta\theta)_{\mathrm{B}}$ and $(m - m_i)(\Delta\theta)_{\mathrm{B}} \ll \theta_i < 90^o$, so the

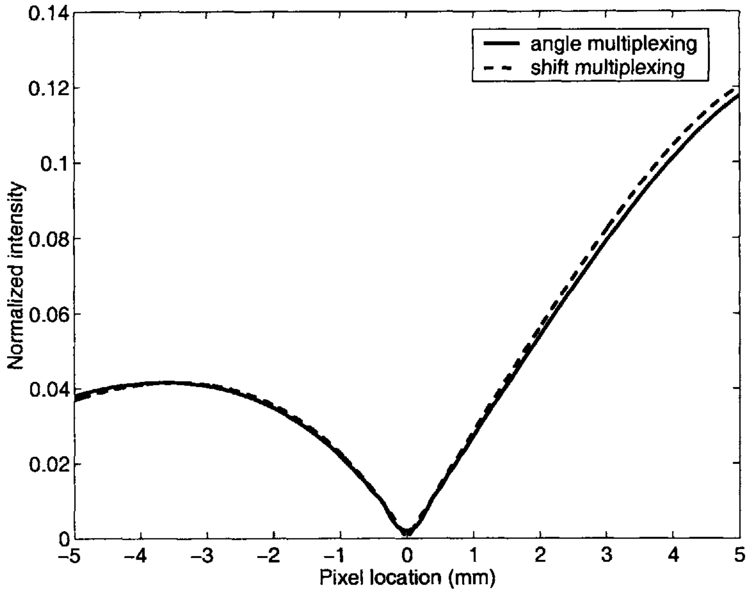

Figure 4-4: The single-pass crosstalk noise comparison: angle multiplexing and shift multiplexing. The parameters used for simulation were hologram thickness L = 10mm, wavelength λ = 488nm, focal length F = 50mm, angle of incidence of the signal $\theta_S = 20^o$, angle of the initial reference beam $\theta_i = 0^o$ and $m_i = 501$.

single-pass diffraction efficiency of crosstalk noise can be approximated as

$$\eta_1^X \approx \eta_1 \sum_{m=1}^{M} \mathrm{sinc}^2 \left[p(m-m') \left(1 - \frac{x' \cos\theta_i \cos\theta_S}{F \sin(\theta_i + \theta_S)} \right) \right]. \tag{4.37}$$

4.3 Resonant holography

The idea of enclosing holograms in optical cavities has been proposed in several information processing contexts. The first references, to our knowledge, utilized re-entrant diffraction from holograms into ring cavities for associative memory [60, 61]. In these experiments, a van der Lugt correlator with a given stored pattern was probed by a partially distorted version of the same pattern and the autocorrelation signal was enhanced by successive passes through the cavity. Subsequently, a new idea emerged for high-efficiency optical interconnects [62, 63] implemented by two Fabry-Perot optical cavities crossed and coupled via a hologram located at the intersection of the cavities.

One of the two crossed cavities was oriented along the reference beam direction, and the other along the signal beam direction. The hologram was recorded so that the beam from the reference cavity was diffracted into the signal cavity, and *vice versa.* It was found that resonance requires the reflectivity of the partially reflecting mirrors and the cavity path lengths to satisfy certain matching conditions.

Even though the idea of combining two elements with powerful optical properties, holograms and optical resonators, is very appealing, these early ideas were left somewhat dormant for over a decade. Recently, interest in resonant holograms was revived [64, 65]. In Ref. [64], it was shown experimentally that the diffraction efficiency of a weakly diffracting hologram can approach 100% if the hologram is enclosed in a Fabry–Perot optical cavity which satisfies reflectivity and path length conditions similar to those of Ref. [63]. The main difference in Ref. [64] was that the authors chose to resonate the reference beam only. Therefore, it was possible to diffract complex patterns out of the cavity, whereas with the crossed resonators of Ref. [63] the diffracted beam can only be a plane wave oriented along the direction of the signal cavity. A simple holographic memory was experimentally demonstrated where each stored hologram was individually retrievable with high diffraction efficiency due to resonance. In Ref. [65], the case of a strong hologram enclosed in an optical cavity was analyzed using coupled mode theory. It was found that reference depletion in the strong hologram decreases the resonator's potential for efficiency improvement. From Ref. [64] and [65], the conclusion is that resonant holography makes most sense with weak holograms, provided that absorption and scattering losses are small enough.

These new directions for resonant holography are promising for traditional holographic applications, such as memories, interconnects and imaging applications [66, 29]. In all three types of applications the simplest use of resonance is to increase the diffraction efficiency. In memories and interconnects, efficiency leads to smaller error rates, whereas in imaging applications improved photon utilization is equivalent to better resolution [67].

In the following, we analyze crosstalk in the resonant holographic memories, both angle– and shift– multiplexed. In Section 4.4, we carry out the calculation for the case of unapodized plane wave reference, and find out the condition where resonance is favorable. In Section 4.5, we show that further improvement is achieved by apodization, which is well known for non-resonant memories. In the specific case of resonant memories, Gaussian apodization turns out to be the most practical, because the Gaussian beam is an eigenmode of spherical mirror cavities. Also, this type of cavity tends to be more stable than flat–mirror, Fabry–Perot type cavities [68]. Therefore we carry out the analysis for holograms, recorded and readout with a Gaussian reference beam. In Section 4.6, we extend our discussion to Hermite-Gaussian beams. Mode multiplexing with Hermite-Gaussian references is proposed. We derive and simulate the diffraction response of mode multiplexing, and finally analyze its crosstalk .

4.4 Crosstalk in resonant holographic memories

In volume holographic storage systems, a large number of pages of information are stored within the volume of the recording medium. Because of the finite bandwidth of the stored pages, we can not get perfect selectivity when reading out a desired page. In the reconstruction process of the desired page, all other undesired pages are also partially reconstructed. The superposition of these undesired reconstructions is crosstalk noise [69].

Here, we discuss the crosstalk noise in resonant holographic storage systems. We find that memory capacity can be improved when resonant holography is used in holographic storage applications. First, we define the signal to noise ratio

$$(\mathrm{SNR}) = \frac{P_{\mathrm{S}}}{P_{\mathrm{X}} + P_{\mathrm{N}}} \tag{4.38}$$

as one metric to assess memory quality. In Eq. 4.38, P_{S} is the signal power, which is proportional to the diffraction efficiency. P_{X} is the crosstalk noise, which is predictable from the geometry of the optical systems and the content of the memory, whereas P_{N} includes other types of noise, such as thermal and shot noise, which are truly random. Even though P_{X} is predictable, its removal would require a rather difficult deconvolution operation involving all the stored data pages. For large-capacity holographic memories, the computational burden required for that deconvolution would be unmanageable because each page would have to be read out and participate in the calculation. For this reason, in holographic memories literature it has been customary to treat P_X as random (precluding deconvolution between pages).

Returning to 4.38, SNR is a useful metric because it is related to memory capacity in the sense that higher SNR results in lower error rate. The exact relationship can be quantified for cases when crosstalk and electrical noise are both Gaussian [70]. For non-Gaussian noise (e.g. Poisson) the analysis is prohibitively difficult, so in this thesis we simply restrict the calculations to the SNR itself. We can see that two methods are available for improving the SNR: increase the diffraction efficiency, or decrease either source of noise.

From Ref. [64], the diffraction efficiency can be greatly enhanced when the hologram is embedded in a resonant Fabry–Perot type cavity, as shown in Fig. 4-5. Both forward and backward-propagating probe beams are diffracted to amplify the signal beam as they pass through the volume hologram. Moreover, forward and phase-conjugate reconstructions are obtained simultaneously. Therefore, the reconstruction quality can be expected to improve by the resonator through signal amplification, but the possible simultaneous resonant amplification of crosstalk noise remains a concern. This issue is the focus of this section.

We will consider simultaneously the angle and shift multiplexing geometries, whose resonant implementations are shown respectively in Fig. 4-6(a) and 4-6(b). As in Ref. [64], η_1 is the single-pass diffraction efficiency of the hologram (which is obtained from the stand-alone hologram, without an optical cavity). Let η_1^X denote the single-pass diffraction efficiency of the crosstalk noise,

$$\eta_1^X \approx \eta_1 \sum_{m=1}^{M} \operatorname{sinc}^2 \left[p(m-m') \left(1 - \frac{x' \cos\theta \cos\theta_S}{F \sin(\theta + \theta_S)} \right) \right], \tag{4.39}$$

where θ and θ_S denote the directions of the initial reference and signal beams, as derived in Section 4.2. If $\theta = 0$ and the paraxial condition for signal carrier are

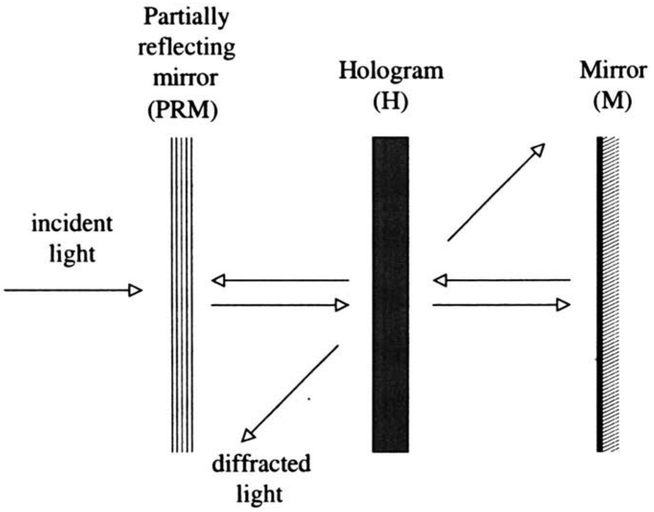

Figure 4-5: Geometry for resonant holography

satisfied, then 4.39 reduces to

$$\eta_1^{\mathrm{X}} \approx \eta_1 \sum_{m=1}^{M} \mathrm{sinc}^2 \left[p(m-m') \left(1 - \frac{x'}{\theta_{\mathrm{S}} F} \right) \right]. \tag{4.40}$$

which is identical to the crosstalk equation for shift multiplexing [59]. Here, M denotes the number of pages that are multiplexed in the memory, page m' is being reconstructed and the pages are separated by p shift Bragg nulls [59]; F is the focal length of the Fourier lens after the hologram, and x' is the coordinate of pixel location on the detector plane. Thus, Eqs. 4.39 and 4.40 can be used for both in shift and angle multiplexing by exchanging $\sin(\theta+\theta_{\mathrm{S}})/(\cos\theta\cos\theta_{\mathrm{S}})$ and θ_{S}. So although our results with resonance are calculated in the geometry of shift multiplexing, they are also applicable in angle multiplexing.

Following the notation of Ref. [64], let r denote the amplitude reflectivity of the partially reflecting mirror, λ the wavelength, b the single-pass intensity loss coefficient inside the cavity, and l the optical path length of the cavity. In ref. [64], the resonance conditions are obtained as

$$r = 1 - \eta_1 - b, \tag{4.41}$$

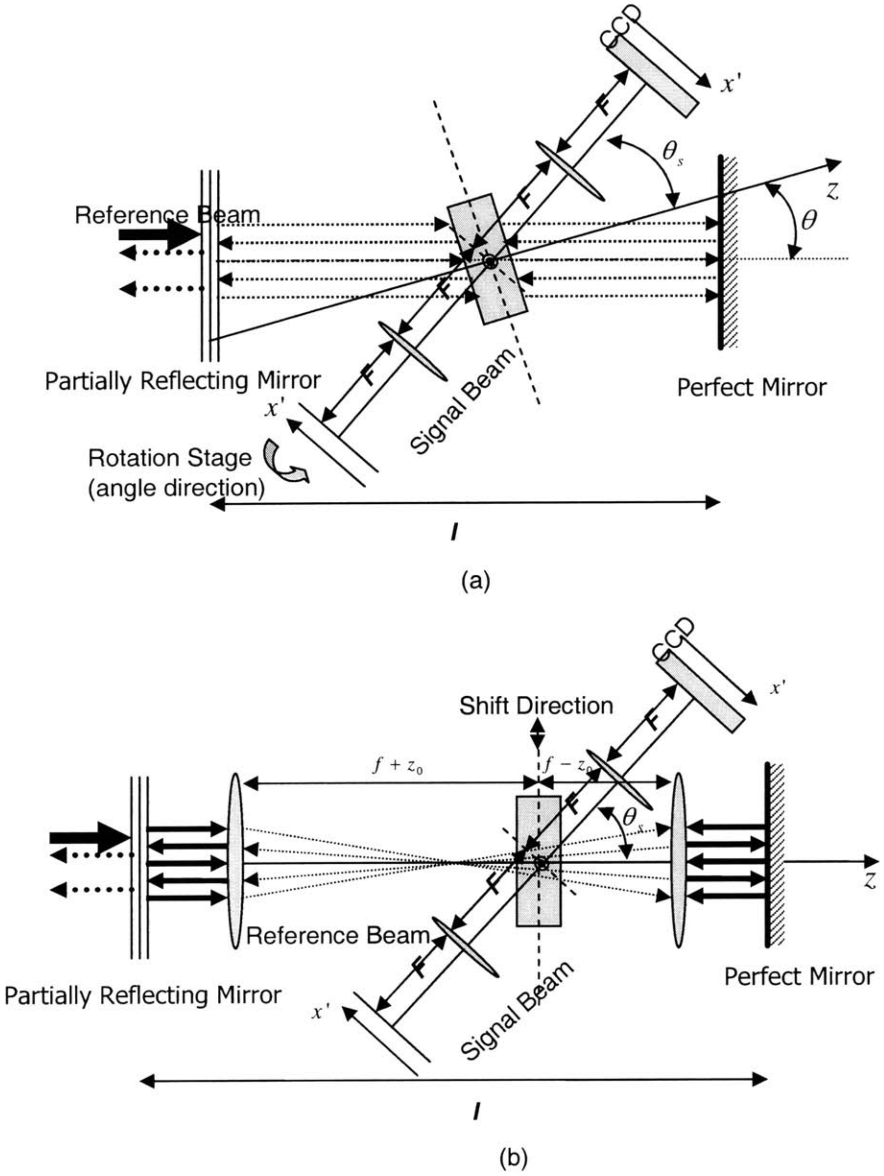

Figure 4-6: (a) Geometry for resonant holography with angle multiplexing (b) Geometry for resonant holography with shift multiplexing

and

$$l = (2m+1)\frac{\lambda}{4}. \tag{4.42}$$

Because we want to have the largest amplification of diffraction efficiency of the Bragg-matched page, these two resonance conditions must be satisfied. The total resonant diffraction efficiency is then

$$\eta_\infty = \frac{\eta_1}{\eta_1 + b}. \tag{4.43}$$

Since $\eta_1 + b < 1$, the resonant gain $G = \eta_\infty/\eta_1$ is always greater than 1. Bragg-mismatched pages do not satisfy the resonance condition 4.41. From [64] and 4.40, we can readily find the non-resonant forward, phase-conjugate and overall crosstalk are, respectively,

$$\eta_{\mathrm{fw}}^{\mathrm{X}} = \frac{\eta_1^{\mathrm{X}}(1-r^2)}{1 + r^2(1-\eta_1^{\mathrm{X}} - b)^2 + 2r(1-\eta_1^{\mathrm{X}} - b)}, \tag{4.44}$$

$$\eta_{\mathrm{pc}}^{\mathrm{X}} = \eta_{\mathrm{fw}}^{\mathrm{X}}(1 - \eta_1^{\mathrm{X}} - b), \qquad \text{and} \tag{4.45}$$

$$\eta_\infty^{\mathrm{X}} = \eta_{\mathrm{fw}}^{\mathrm{X}} + \eta_{\mathrm{pc}}^{\mathrm{X}}. \tag{4.46}$$

Using 4.38, we obtain the resonant SNR as

$$(\mathrm{SNR})_\infty = \frac{\eta_\infty}{\eta_\infty^{\mathrm{X}} + \eta_{\mathrm{N}}}. \tag{4.47}$$

where $\eta_{\mathrm{N}} = P_{\mathrm{N}}/P_{\mathrm{total}}$ is the ratio of the power of other types of noise and the total incident power.

From Eqs. 4.44– 4.46, we can see that the diffraction efficiency of crosstalk noise is also increased by the resonator. In fact, the crosstalk amplification $\eta_\infty^{\mathrm{X}}/\eta_1^{\mathrm{X}}$ is greater than the resonant amplification of the signal η_∞/η_1. So it is only when the increased diffraction efficiency overcomes the increase of the total noise contribution that the retrieval quality of resonant holograms improves. In order to quantify the occurrence of this favorable condition in terms of the parameters η_1 and η_{N}, we use the figure of

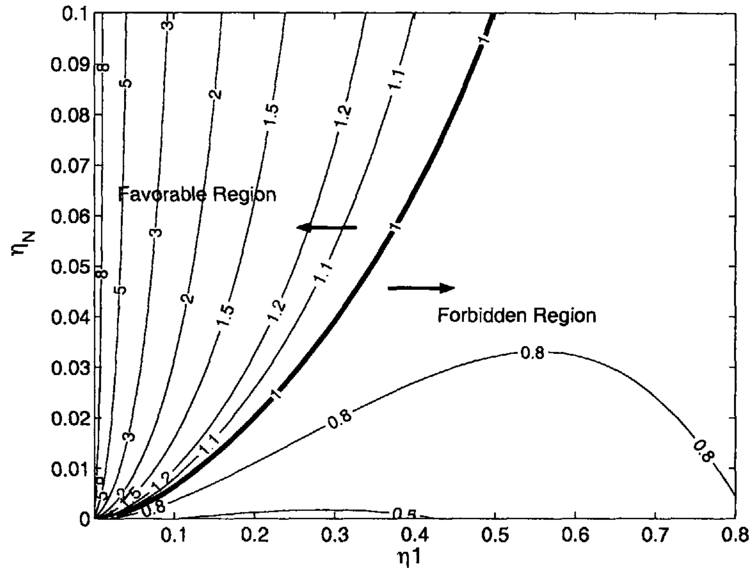

Figure 4-7: Figure of Merit with plane reference: The parameters used for the figure were hologram thickness $L = 10\text{mm}$, wavelength $\lambda = 488\text{nm}$, focal length $F = 50\text{mm}$, angle of incidence of the signal $\theta_{\mathrm{S}} = 20^o$.

merit

$$FM = \frac{(\mathrm{SNR})_\infty}{(\mathrm{SNR})_1}, \tag{4.48}$$

where $(\mathrm{SNR})_1 = \eta_{\mathrm{l}}/(\eta_{\mathrm{l}}^{\mathrm{X}} + \eta_{\mathrm{N}})$ is the single-pass SNR. When $FM > 1$, resonance is favorable; when $FM < 1$, the resonator actually degrades noise performance so we call it the "forbidden" region. Simulations were carried out to estimate the resonance effect in the case of shift multiplexing. Here we assumed that 1000 holograms were stored in 1001 shift-multiplexed positions, leaving position 501 blank. Then the power in position #501 is due to cross-talk noise alone. In the simulation, the shift separation between two adjacent holograms was equal to 2 shift Bragg nulls. The results are shown in Fig. 4-7, where we can see that memory quality improves when η_{l} is small and η_{N} is large. In this region, the crosstalk noise is relatively smaller than other types of noise. So its amplification according Eqs. 4.44– 4.46 is not sufficient to offset the resonant amplification of the signal.

4.5 Apodization

Because crosstalk noise comes from the sidelobes of the Bragg selectivity response curve, the method of apodization suggests itself as a possible remedy [71, 72]. Apodization is implemented by using a reference beam which is nonuniform in either amplitude or phase, e.g. a low aperture Gaussian beam. For the geometry illustrated in Fig. 4-8 and recorded by references with nonuniform beam profile $\tilde{E}_{\mathrm{f}}(z)$, the analytical expression of the readout intensity with probing references having nonuniform beam profile $\tilde{E}_{\mathrm{p}}(z)$ can be derived with an approach similar to that used in Ref. [2]. The result is

$$I(\Delta\theta) \propto \left| \int_{-\infty}^{\infty} \mathrm{rect}\left(\frac{z}{L}\right) \tilde{E}_{\mathrm{f}}(z) \tilde{E}_{\mathrm{p}}(z) \exp(i\xi z) dz \right|^2, \tag{4.49}$$

where $\xi = (2\pi/\lambda)[\Delta\theta \sin(\theta + \theta_{\mathrm{S}})/\cos\theta_{\mathrm{S}}]$ is the Bragg mismatch factor due to the angle difference between the recording and probing references and L is the thickness of the hologram. In deriving Eq. 4.49, we assumed that the angle multiplexing is used and the signal beam is a plane wave without loss of generality. We do not discuss apodization for shift multiplexed memories in this thesis. Note also that the cavity must be formed by spherical mirrors so as to support a Gaussian beam mode in this case.

From Eq. 4.49, we can see that the diffraction efficiency as a function of probe rotation $(\Delta\theta)$ is the Fourier transform of the beam profile function convolved with a sinc function determined by the thickness of the hologram. Comparing to the sinc function without apodization ($\tilde{E}_{\mathrm{f}}(z) \equiv 1$ and $\tilde{E}_{\mathrm{p}}(z) \equiv 1$), if each hologram is recorded and reconstructed with the same reference beam profile, the resulting selectivity response has a lower sidelobe level. However, the main lobe becomes wider [72]. The selectivity response in that case is

$$I(\Delta\theta) \propto \left| \int_{-\infty}^{\infty} \mathrm{rect}\left(\frac{z}{L}\right) \tilde{E}_{f}(z)^2 \exp(i\xi z) dz \right|^2. \tag{4.50}$$

Consider a Gaussian reference $\exp[-x^2/w^2]$ at the hologram for both recording and probing, where w is the width of the Gaussian beam at the position of the

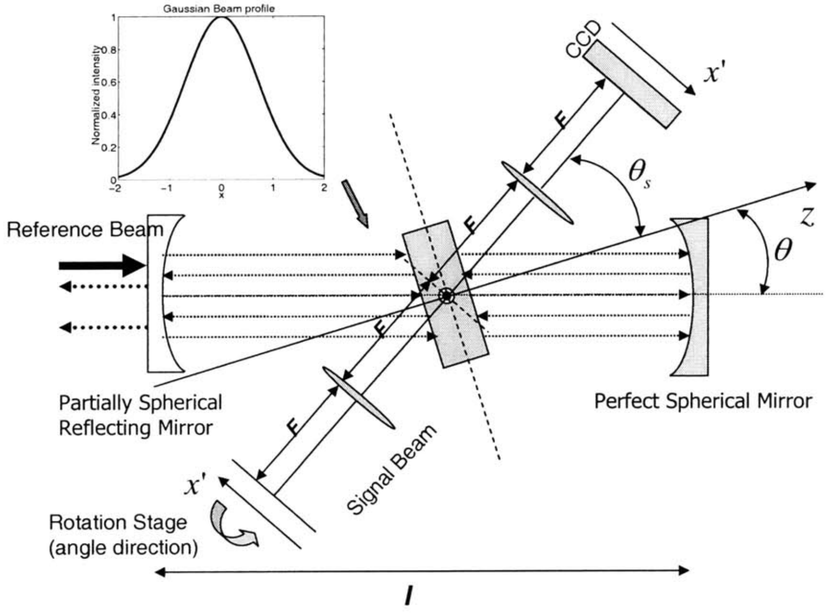

Figure 4-8: Geometry for apodization with angle multiplexing

hologram. Because the angle between the references and the z axis is not 90^o, the actual width of the Gaussian beam along the z direction is $w/\sin\theta$. By substituting it into Eq. 4.50, the selectivity response function is obtained as

$$I(\Delta\theta) \propto \left| \int_{-\infty}^{\infty} \text{rect}\left(\frac{z}{L}\right) \exp(-\frac{\sin^2\theta}{w^2}z^2) \exp(-\frac{\sin^2(\theta+\Delta\theta)}{w^2}z^2) \exp(i\xi z) dz \right|^2, \quad (4.51)$$

Using the convolution property of Fourier transforms and neglecting the divergence of the beam, 4.51 can be written in more simplified form as

$$I(\Delta\theta) \propto \left| \text{sinc}\left(\frac{L}{2\pi}\xi\right) \otimes \exp(-\frac{w^2}{8\sin^2\theta}\xi^2) \right|^2 \equiv \left|(\text{sinc} \otimes \text{Gauss})(\xi)\right|^2. \quad (4.52)$$

The selectivity response according to relation 4.52 is shown in Fig. 4-9. We can see that Gaussian references result in a very low sidelobe level (defined as the ratio of the largest sidelobe amplitude to the main lobe amplitude.)

For the Fourier–plane geometry of Fig. 4-8, the expression of the crosstalk noise

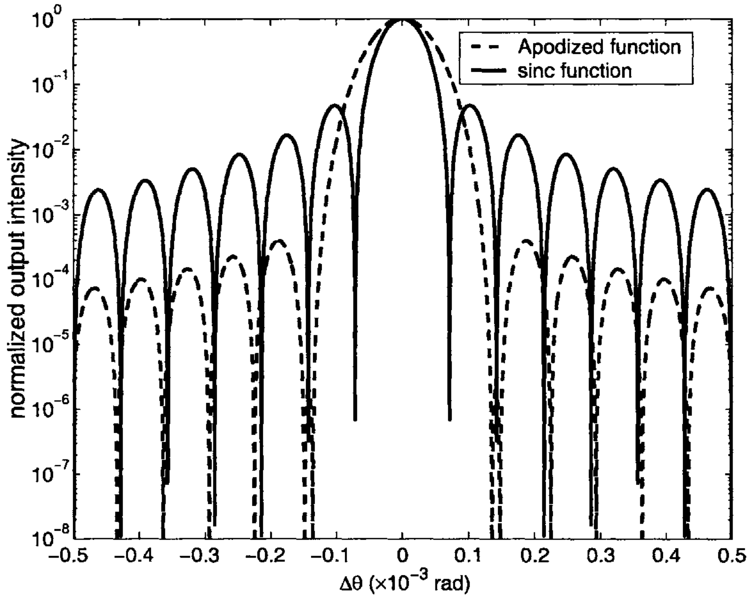

Figure 4-9: Apodization with Gaussian references: The parameters used for simulation were hologram thickness L = 10mm, angle of incidence of the signal $\theta_S = 20^o$, angle of the reference beam $\theta = 20^o$, wavelength λ = 488nm, the width of the Gaussian beam w = 1.6mm

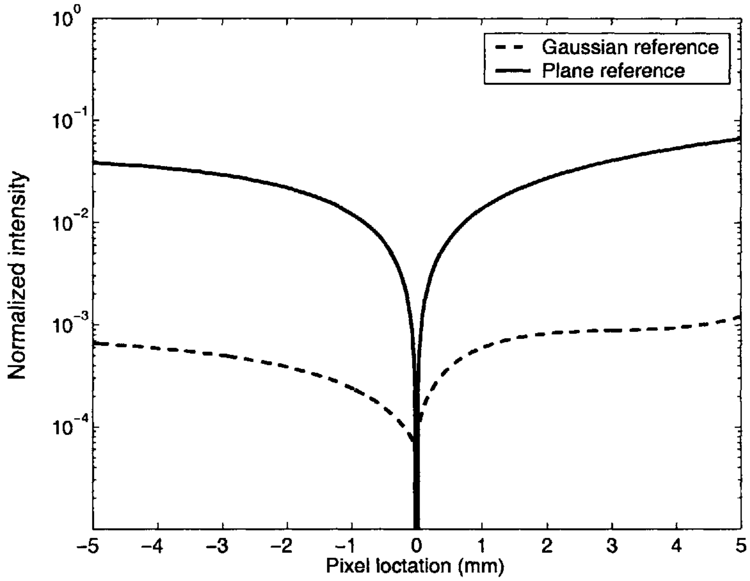

Figure 4-10: Crosstalk noise with Gaussian references: The parameters used for this plot were the same as in figure 4-9. (Note that here logarithm coordinate is used.)

with Gaussian references is obtained along the line of Section 4.2 as

$$\eta_1^{\mathrm{X}} \approx \eta_1 \sum_{m=1}^{M} \left| (\mathrm{sinc} \otimes \mathrm{Gauss}) \left[\frac{2\pi}{L} p(m-m') \left(1 - \frac{x' \cos\theta \cos\theta_{\mathrm{S}}}{F \sin(\theta + \theta_{\mathrm{S}})} \right) \right] \right|^2 . \tag{4.53}$$

We simulated the crosstalk noise with Gaussian references and compare it with the crosstalk noise with plane references, as shown in Fig. 4-10. Here, in the comparison we stored 1000 holograms in 1001 angle-multiplexed positions, leaving position 501 blank. The angle separation of the adjacent separation of the adjacent holograms was 2 angle Bragg separations with plane references but 1 angle Bragg separation with Gaussian references because these two Bragg nulls are almost at the same place in Fig. 4-9.

From Fig. 4-10, we can see the crosstalk is decreased greatly, almost by 2 orders of magnitude compared to the unapodized case. The additional prominent difference between the unapodized and apodized cases are observed in Fig. 4-10: the crosstalk never reaches zero in the apodized case. This is because the Bragg selectivity curve has minimum but not nulls in apodized case.

From section 4.4, we know that the memory quality can be improved by use of resonance when the crosstalk noise is small. With Gaussian references which decrease the crosstalk greatly, the resonator can be more efficient to improve the memory quality. This is shown in Fig. 4-11, where the favorable region is extended to almost all values of η_1 and η_{N} except those with very large η_1 (where use of the resonant technique is uninteresting anyway) and very small η_{N} (less than about 10^{-3}).

4.6 Mode multiplexing with Hermite-Gaussian references

In Section 4.5, we discussed the apodization effect of Gaussian references on resonant holograms. The Gaussian beam is the lowest order solution to the paraxial wave equation. In this section, we will extend our discussion to higher-order modes, known as Hermite-Gaussian beams. In addition to the apodization effect, Hermite-

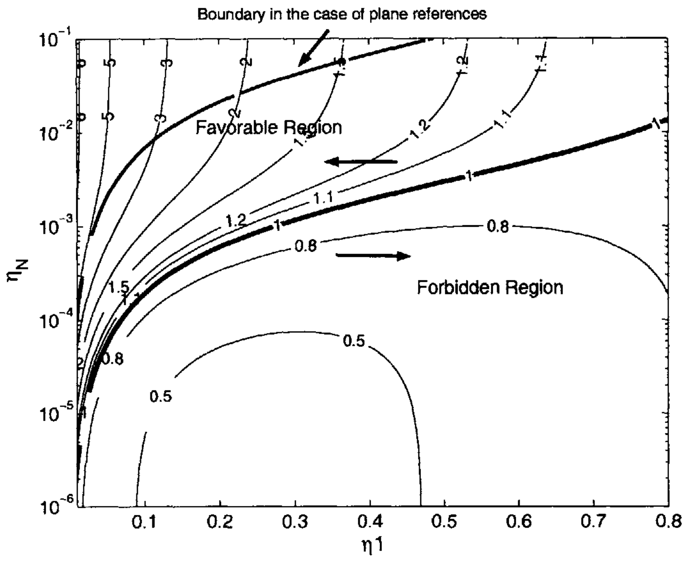

Figure 4-11: Figure of Merit with Gaussian reference: The parameters used for this figure were the same as in figure 4-9. (Note that here logarithm coordinate is used.)

Gaussian beams have another important property, orthogonality, which can result in perfect selectivity (zero inter-page crosstalk) when one mode of Hermite-Gaussian beam is used to read out a volume hologram recorded by a different mode of Hermite-Gaussian beam and signal beam. Furthermore, the Hermite-Gaussian beams are also eigenmodes of resonators with finite rectangular aperture. The orthogonality property suggests a new multiplexing method, which we refer to as mode multiplexing.

The geometry for mode multiplexing with Hermite-Gaussian references is shown in Fig. 4-12. Assume that a thick hologram is recorded by a plane wave signal and a Hermite-Gaussian reference, denoted as $\Psi_{\mathrm{mn}}(x, y, z)$. m and n are the order of the Hermite-Gaussian in $x-$ and y-direction, respectively. The waist of the Hermite-Gaussian reference is located at $z = z_0$. The waist is determined by the confocal parameter b with $w_0 = \sqrt{2b/k} = \sqrt{\lambda b/\pi}$, where $k = 2\pi/\lambda$. The expression for the Hermite-Gaussian reference in the coordinate system centered in the volume hologram

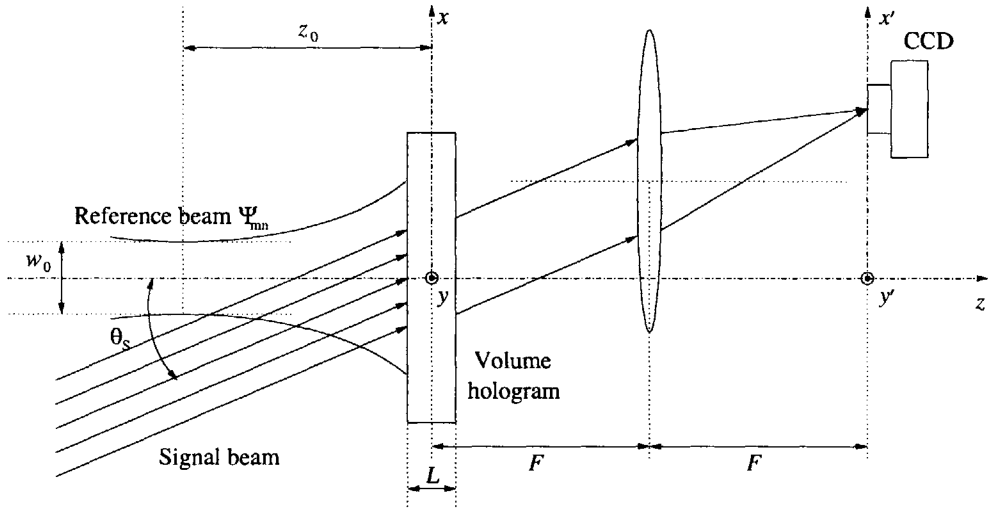

Figure 4-12: The geometry for mode multiplexing by Hermite Gaussian references.

is

$$\begin{aligned}\Psi_{\rm mn}(x,y,z) &= \frac{C_{\rm mn}}{\sqrt{1+\frac{(z-z_0)^2}{b^2}}} H_{\rm m}\left(\frac{\sqrt{2}x}{w(z)}\right) H_{\rm n}\left(\frac{\sqrt{2}y}{w(z)}\right) \exp\left(-\frac{x^2+y^2}{w^2(z)}\right) \\ &\quad \exp\left(-j\frac{2\pi}{\lambda}\frac{(x^2+y^2)}{R(z)}\right) e^{({\rm m+n+1})\phi}, \qquad (4.54)\end{aligned}$$

where

$$w^2(z) = \frac{2b}{k}\left(1+\frac{(z-z_0)^2}{b^2}\right) = w_0^2\left(1+\frac{(z-z_0)^2}{b^2}\right), \qquad (4.55)$$

$$\frac{1}{R(z)} = \frac{z-z_0}{(z-z_0)^2+b^2}, \qquad (4.56)$$

$$\tan\phi = \frac{z-z_0}{b}, \qquad (4.57)$$

$$C_{\rm mn} = \left(\frac{2}{w_0^2\pi 2^{\rm m+n}{\rm m!n!}}\right)^{1/2}. \qquad (4.58)$$

In Eq. 4.54, $H_{\rm m}(\xi)$ is the Hermite Polynomial of order m; $w(z)$, $R(z)$ and ϕ de-

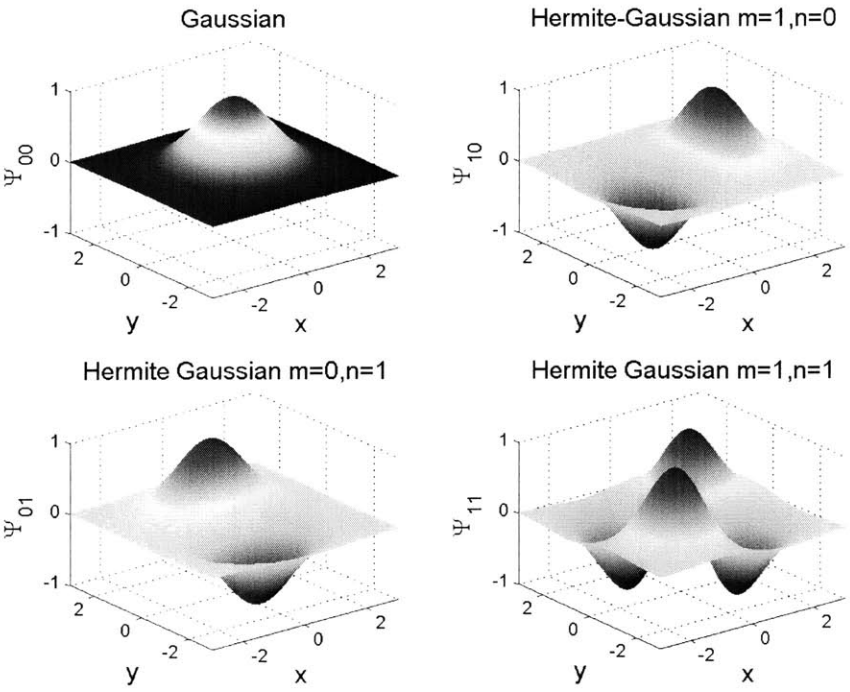

Figure 4-13: The amplitude patterns for Hermite-Gaussian beams with mode (n,m) = (00), (10), (01) and (11).

note the radius of the beam, the wavefront curvature and the phase shift of the Hermite-Gaussian at position z, respectively; and C_{mn} is the normalization factor. The amplitude patterns of different modes of Hermite-Gaussian beams are shown in Fig. 4-13. The plane wave signal is incident on the $x-z$ plane with angle θ_{s} with the z axis, and its electric field is expressed as

$$E_{\mathrm{S}}(x,z)=\exp\left(-j2\pi u_{\mathrm{S}}\frac{x}{\lambda}\right)\exp\left[-j2\pi\left(1-\frac{u_{\mathrm{S}}^2}{2}\right)\frac{z}{\lambda}\right]. \tag{4.59}$$

where $u_{\mathrm{S}}\equiv\sin\theta_{\mathrm{S}}\approx\theta_{\mathrm{S}}\ll 1$. Note that here we represent phase delay as $\exp(-jkz)$ along the wave propagation direction in agreement with accepted conventions for Hermite-Gaussian beams [46]. By assuming low-bandwidth modulation and using Eq. 4.9, the dielectric modulation of the volume hologram can be expressed as

$$\Delta\epsilon(\mathbf{r})=\epsilon_1\Psi^*_{\mathrm{mn}}(x,y,z)E_{\mathrm{S}}(x,z), \tag{4.60}$$

We now calculate the expression for the field diffracted by the volume hologram when probed by another Hermite-Gaussian mode $\Psi_{\mathrm{m'n'}}(x, y, z)$ (m $\neq$ m' or n $\neq$ n'). $\Psi_{\mathrm{m'n'}}(x, y, z)$ has same waist as the reference Ψ_{mn}, and their waists are located at the same position as well as they propagate in the same direction. But they may have different mode, *i.e.* m $\neq$ m$'$ or n $\neq$ n$'$. Using Eq. 4.10, we obtain

$$E_{\mathrm{d}}(\mathbf{r}'') = \iiint \Psi_{\mathrm{m'n'}}(\mathbf{r})\Psi^{*}_{\mathrm{mn}}(\mathbf{r})E_{\mathrm{S}}(\mathbf{r})V(\mathbf{r})G(\mathbf{r}'' - \mathbf{r})\mathrm{d}^3\mathbf{r}, \tag{4.61}$$

where the constant term ϵ_1 is neglected, $V(\mathbf{r})$ and $G(\mathbf{r})$ are the index function Eq. 4.11 and free space Green's function, respectively. Under the paraxial approximation, we substitute Eq. 4.12 as well as Eqs. 4.54 and 4.60 into Eq. 4.61:

$$\begin{aligned}
&E_{\mathrm{d}}(x'', y'', z'') \\
&= \iiint \frac{C_{\mathrm{mn}}C_{\mathrm{m'n'}}}{1 + \frac{(z-z_0)^2}{b^2}} H_{\mathrm{m}}\left(\frac{\sqrt{2}x}{w(z)}\right) H_{\mathrm{m'}}\left(\frac{\sqrt{2}x}{w(z)}\right) H_{\mathrm{n}}\left(\frac{\sqrt{2}y}{w(z)}\right) H_{\mathrm{n'}}\left(\frac{\sqrt{2}y}{w(z)}\right) \\
&\quad \exp\left(-2\frac{x^2 + y^2}{w^2(z)}\right) e^{[(\mathrm{m}-\mathrm{m'})+(\mathrm{n}-\mathrm{n'})]\phi} \exp\left(-j2\pi u_{\mathrm{S}}\frac{x}{\lambda}\right) \\
&\quad \exp\left[-j2\pi\left(1 - \frac{u_{\mathrm{S}}^2}{2}\right)\frac{z}{\lambda}\right] V(x, y, z)\frac{1}{j\lambda\left(z'' - z\right)} \exp\left(-j2\pi\frac{z'' - z}{\lambda}\right) \\
&\quad \exp\left[-j\pi\frac{\left(x'' - x\right)^2 + \left(y'' - y\right)^2}{\lambda\left(z'' - z\right)}\right] \mathrm{d}x\mathrm{d}y\mathrm{d}z.
\end{aligned} \tag{4.62}$$

Instead of the actual diffracted field just after the volume hologram, it is most informative to calculate its Fourier transform which is incident on the detector after passing a Fourier lens of focal length F, as shown in Fig. 4-12. From Fourier optics, we find

$$E_{\mathrm{d}}(x', y') = \iint_{-\infty}^{\infty} E_{\mathrm{d}}(x'', y'', 0) \exp\left(-j2\pi\frac{x'x'' + y'y''}{\lambda F}\right) \mathrm{d}x''\mathrm{d}y''. \tag{4.63}$$

Here, we assume that the effective aperture of the system is determined by the transverse size of the volume hologram rather than the lens. So the limits of integration in equation 4.63 are taken to be infinite. By substituting equation 4.62 into equation 4.63 and performing the x'' and y'' integrations analytically using the lemma 4.15, we can obtain the diffracted field on the CCD plane as

$$\begin{aligned} & E_{\mathrm{d}}(x', y', z') \\ = & \iiint \frac{C_{\mathrm{mn}} C_{\mathrm{m'n'}}}{1 + \frac{(z-z_0)^2}{b^2}} H_{\mathrm{m}} \left(\frac{\sqrt{2}x}{w(z)} \right) H_{\mathrm{m'}} \left(\frac{\sqrt{2}x}{w(z)} \right) H_{\mathrm{n}} \left(\frac{\sqrt{2}y}{w(z)} \right) H_{\mathrm{n'}} \left(\frac{\sqrt{2}y}{w(z)} \right) \\ & \exp \left(-2 \frac{x^2 + y^2}{w^2(z)} \right) e^{[(\mathrm{m-m'}) + (\mathrm{n-n'})]\phi} V(x, y, z) \exp \left\{ -j \frac{2\pi}{\lambda} \left(\frac{x'}{F} + u_{\mathrm{S}} \right) x \right\} \\ & \exp \left\{ -j \frac{2\pi}{\lambda} \frac{y'}{F} y \right\} \exp \left\{ -j \frac{\pi}{\lambda} \left(\frac{x'^2 + y'^2}{F^2} - u_{\mathrm{S}}^2 \right) z \right\} \mathrm{d}x \mathrm{d}y \mathrm{d}z. \end{aligned} \tag{4.64}$$

Here, we have neglected amplitude term $1/j\lambda(z'' - z)$ since it contributes little to the integral, in comparison with fast varying exponential terms. We also assume that the dimensions of the volume hologram are infinite in the transverse $x-$ and $y-$directions and the thickness of the volume hologram is L in the z direction. Eq. 4.64 can be organized as

$$\begin{aligned} & E_{\mathrm{d}}(x', y', z') \\ = & \int_{-\infty}^{\infty} \frac{C_{\mathrm{mn}} C_{\mathrm{m'n'}}}{1 + \frac{(z-z_0)^2}{b^2}} \mathrm{rect} \left(\frac{z}{L} \right) \exp \left\{ -j \frac{\pi}{\lambda} \left(\frac{x'^2 + y'^2}{F^2} - u_{\mathrm{S}}^2 \right) z \right\} e^{[(\mathrm{m-m'}) + (\mathrm{n-n'})]\phi} \\ & \left\{ \int_{-\infty}^{\infty} H_{\mathrm{m}} \left(\frac{\sqrt{2}x}{w(z)} \right) H_{\mathrm{m'}} \left(\frac{\sqrt{2}x}{w(z)} \right) \exp \left(-2 \frac{x^2}{w^2(z)} \right) \exp \left[j \frac{2\pi}{\lambda} \left(\frac{x'}{F} + u_{\mathrm{S}} \right) x \right] \mathrm{d}x \right\} \\ & \left\{ \int_{-\infty}^{\infty} H_{\mathrm{n}} \left(\frac{\sqrt{2}y}{w(z)} \right) H_{\mathrm{n'}} \left(\frac{\sqrt{2}y}{w(z)} \right) \exp \left(-2 \frac{y^2}{w^2(z)} \right) \exp \left[-j \frac{2\pi}{\lambda} \frac{y'}{F} y \right] \mathrm{d}y \right\} \mathrm{d}z, \end{aligned} \tag{4.65}$$

where the x and y integrals are independent with each other and can be calculated analytically from the formulae of Hermite integrals in Section 4.A,

$$\begin{aligned} & I_{\mathrm{mm'}}(z) \\ = & \int_{-\infty}^{\infty} H_{\mathrm{m}} \left(\frac{\sqrt{2}x}{w(z)} \right) H_{\mathrm{m'}} \left(\frac{\sqrt{2}x}{w(z)} \right) \exp \left(-2 \frac{x^2}{w^2(z)} \right) \exp \left[j \frac{2\pi}{\lambda} \left(\frac{x'}{F} + u_{\mathrm{S}} \right) x \right] \mathrm{d}x \\ = & \frac{w(z)}{\sqrt{2}} \sqrt{\pi} 2^m e^{-a_x^2(z)} \left[j a_x(z) \right]^{\mathrm{m-m'}} P_{\mathrm{mm'}} \left(-2a_x^2(z) \right), \end{aligned} \tag{4.66}$$

$$\begin{aligned}
&I_{\mathrm{nn'}}(z)\\
&= \int_{-\infty}^{\infty} H_{\mathrm{n}}\left(\frac{\sqrt{2}y}{w(z)}\right) H_{\mathrm{n'}}\left(\frac{\sqrt{2}y}{w(z)}\right) \exp\left(-2\frac{y^2}{w^2(z)}\right) \exp\left[-j\frac{2\pi}{\lambda}\frac{y'}{F}y\right] \mathrm{d}y\\
&= \frac{w(z)}{\sqrt{2}}\sqrt{\pi}2^n e^{-a_y^2(z)} \left[ja_y(z)\right]^{\mathrm{n}-\mathrm{n'}} P_{\mathrm{nn'}}\left(-2a_y^2(z)\right), \qquad (4.67)
\end{aligned}$$

where

$$a_x(z) = -\frac{\pi}{\lambda}\left(\frac{x'}{F}+u_{\mathrm{S}}\right)\frac{w(z)}{\sqrt{2}}, \qquad (4.68)$$

$$a_y(z) = -\frac{\pi}{\lambda}\left(\frac{y'}{F}\right)\frac{w(z)}{\sqrt{2}}. \qquad (4.69)$$

For later convenience, we define the distance of one point on the CCD plane away from the center of the signal beam as

$$\delta x' = x' + u_{\mathrm{S}}F, \qquad (4.70)$$

$$\delta y' = y'. \qquad (4.71)$$

Substituting Eqs. 4.66 and 4.67 as well as C_{mn} (Eq. 4.58) and $w(z)$ (Eq. 4.55) into Eq. 4.65, we can obtain the diffraction pattern on the CCD plane as

$$\begin{aligned}
&E_{\mathrm{d}}(x',y',z')\\
&= \int_{-\infty}^{\infty} \frac{1}{(\mathrm{m!n!m'!n'!})^{1/2}} \left[-2a_x^2(z)\right]^{\frac{\mathrm{m}-\mathrm{m'}}{2}} \left[-2a_y^2(z)\right]^{\frac{\mathrm{n}-\mathrm{n'}}{2}}\\
&\quad P_{\mathrm{mm'}}\left(-2a_x^2(z)\right) P_{\mathrm{nn'}}\left(-2a_y^2(z)\right) e^{[(\mathrm{m}-\mathrm{m'})+(\mathrm{n}-\mathrm{n'})]\phi} \mathrm{rect}\left(\frac{z}{L}\right)\\
&\quad \exp\left\{-\frac{\pi}{2\lambda}\left[\left(\frac{x'}{F}+u_{\mathrm{S}}\right)^2+\left(\frac{y'}{F}\right)^2\right]\left(\frac{(z-z_0)^2}{b}+b\right)\right\}\\
&\quad \exp\left\{-j\frac{\pi}{\lambda}\left(\frac{x'^2+y'^2}{F^2}-u_{\mathrm{S}}^2\right)z\right\}\mathrm{d}z. \qquad (4.72)
\end{aligned}$$

One way to understand Eq. 4.72 is that the diffracted pattern is the Fourier transform of the product of the slow varying polynomial terms which is determined by the orders of Hermite-Gaussian reference and probe beam, the rectangular function which is defined by the thickness of the volume hologram, and the Gaussian function which is determined by the radius of the Hermite-Gaussian beam at the location of the volume hologram. Therefore, mode multiplexing by Hermite-Gaussian references has two major differences compared to angle or shift multiplexing with plane or spherical references: (i) when $a_x(z) = 0$ and $\mathrm{m} \neq \mathrm{m}'$ or $a_y(z) = 0$ and $\mathrm{n} \neq \mathrm{n}'$, then $E_{\mathrm{d}}(x', y', z') = 0$ for any value of u_S. It means that the zero inter-page crosstalk due to the independence of the orthogonality of Hermite-Gaussian beams on the direction of the signal beam, in contrast with the angular Bragg selectivity (Eq. 4.30) and shift Bragg selectivity (Eq.5 in Ref. [59]) which explicitly depend on θ_{S}; (ii) the apodization effect due to the Gaussian characteristic of Hermite-Gaussian beams, which will attain similar benefits as we discussed in Section 4.5. So mode multiplexing not only eliminates the inter-page crosstalk, but also decreases intra-page crosstalk to lower level through apodization. This statement has been verified by performing the simulation with Eq. 4.72, as shown in Fig. 4-14. In the simulation, the volume hologram was recorded by a plane-wave signal and a Hermite-Gaussian reference of order $\mathrm{m} = 3, \mathrm{n} = 3$. When the volume hologram is probed by the same order of Hermite-Gaussian beam ($\mathrm{m}' = 3, \mathrm{n}' = 3$), the Bragg matched reconstruction is obtained on the CCD plane (Fig. 4-14(a)). When the volume hologram is probed by a different order of Hermite-Gaussian beam, e.g. $\mathrm{m}' = 1, \mathrm{n}' = 1$, the intensity is equal to zero at the center point $(\delta x', \delta y') = (0, 0)$ and the crosstalk at other points are also very small, on the order of 10^{-3}.

In summary, resonant holography can conditionally improve the memory quality without apodization when the increase of diffraction efficiency overcomes the increase of crosstalk noise. The benefit is derived despite simultaneous quasi-resonant amplification of crosstalk noise. Further gain is attained by apodizing the reference beam. We found that Gaussian apodization the most convenient since the Gaussian beam happens to be an eigenstate of spherical mirror cavities, yields at least one order of magnitude improvement in both the attainable SNR and favorable η_1 values for resonant systems. By utilizing Hermite-Gaussian beams, we proposed a new multiplexing method -- mode multiplexing. Mode multiplexing has perfect selectivity (zero

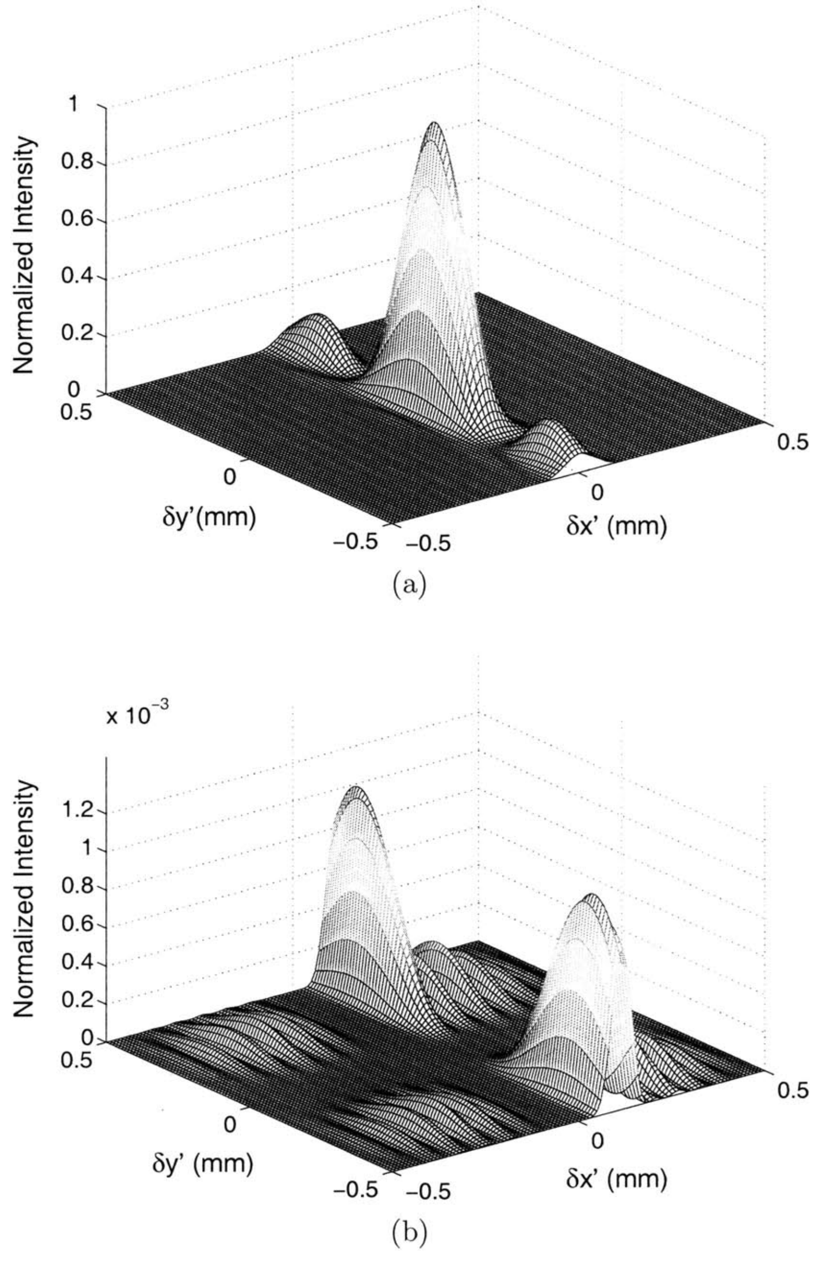

(a)

(b)

Figure 4-14: The volume hologram is recorded by a plane wave and a Hermite-Gaussian reference of order $\mathrm{m} = 3, \mathrm{n} = 3$. (a) Bragg matched diffraction pattern: intensity of the diffracted field when the volume hologram is probed by the Hermite-Gaussian beam with the order of $\mathrm{m}' = 3, \mathrm{n}' = 3$; (b) Bragg mismatched diffraction pattern: the intensity of the diffracted field when the volume hologram is probed by the Hermite-Gaussian beam with the order of $\mathrm{m}' = 1, \mathrm{n}' = 1$. The parameters used here were $L = 1\mathrm{mm}$, $\theta_S = 20^o$, $\lambda = 488\mathrm{nm}$, $F = 50\mathrm{mm}$, and $b = 1\mathrm{mm}$.

inter-page crosstalk) because the orthogonality of Hermite-Gaussian beams does not depend on the direction of signal beam.

4.A Derivation of Hermite integral

In Eq. 4.65, there are two independent integrals on x and y, respectively:

$$\int_{-\infty}^{\infty} H_{\mathrm{m}}\left(\frac{\sqrt{2}x}{w(z)}\right) H_{\mathrm{m}'}\left(\frac{\sqrt{2}x}{w(z)}\right) \exp\left(-2\frac{x^2}{w^2(z)}\right) \exp\left[j\frac{2\pi}{\lambda}\left(\frac{x'}{F}+u_{\mathrm{S}}\right)x\right] \mathrm{d}x, \quad (4.73)$$

$$\int_{-\infty}^{\infty} H_{\mathrm{n}}\left(\frac{\sqrt{2}y}{w(z)}\right) H_{\mathrm{n}'}\left(\frac{\sqrt{2}y}{w(z)}\right) \exp\left(-2\frac{y^2}{w^2(z)}\right) \exp\left[-j\frac{2\pi}{\lambda}\frac{y'}{F}y\right] \mathrm{d}y, \quad (4.74)$$

These two integrals can be written as a uniform form, so called Hermite integral,

$$\int_{-\infty}^{\infty} H_{\mathrm{m}}(\xi)\, H_{\mathrm{n}}(\xi) \exp\left(-\xi^2\right) \exp\left(j2a\xi\right) \mathrm{d}\xi. \quad (4.75)$$

Hermite integral is the generalization of the orthogonality of Hermite-Gaussian functions,

$$\int_{-\infty}^{\infty} H_{\mathrm{m}}(\xi)\, H_{\mathrm{n}}(\xi) \exp(-\xi^2) d\xi = \begin{cases} \sqrt{\pi}2^{\mathrm{n}}\mathrm{n}! & \mathrm{m}=\mathrm{n} \\ 0 & \mathrm{m}\neq\mathrm{n} \end{cases}. \quad (4.76)$$

with $a = 0$. In this section, the Hermite integral will be calculated analytically.

Let's start with the generating function of Hermite-Gaussians

$$\begin{aligned} \mathcal{F}(s,\xi) &\equiv \exp\left(-s^2 + 2s\xi - \frac{\xi^2}{2}\right) \\ &= \sum_{\mathrm{n}=0}^{\infty} \frac{s^{\mathrm{n}}}{\mathrm{n}!} H_{\mathrm{n}}(\xi) \exp\left(-\xi^2/2\right), \end{aligned} \quad (4.77)$$

The Hermite polynomials are the "coefficients" of the Taylor expansion in s of $\mathcal{F}(s,\xi)$. Multiply two generating functions together and integrate both sides from $-\infty$ to ∞.

The result is

$$\begin{aligned}&\int_{-\infty}^{\infty} \exp\left(-s^2+2s\xi-\frac{\xi^2}{2}\right)\exp\left(-p^2+2p\xi-\frac{\xi^2}{2}\right)\exp\left(j2a\xi\right)d\xi\\ &= \sum_{\mathrm{m}=0}^{\infty}\sum_{\mathrm{n}=0}^{\infty}\frac{s^{\mathrm{m}}}{\mathrm{m}!}\frac{p^{\mathrm{n}}}{\mathrm{n}!}\int_{-\infty}^{\infty} H_{\mathrm{m}}\left(\xi\right)H_{\mathrm{n}}\left(\xi\right)\exp\left(-\xi^2\right)\exp\left(j2a\xi\right)d\xi, \qquad (4.78)\end{aligned}$$

The right hand side is the sum of all the Hermite integrals from $(\mathrm{m},\mathrm{n})=(0,0)$ to (∞,∞) while the left hand side can be calculated analytically by using the lemma 4.15,

$$\text{L.H.S.} = \int_{-\infty}^{\infty} e^{-\xi^2+2(s+p+ja)\xi-(s^2+p^2)}\mathrm{d}\xi = \sqrt{\pi}e^{2(s+ja)(p+ja)}e^{a^2}, \qquad (4.79)$$

The L.H.S. can be further expressed by Taylor expansion as

$$\sqrt{\pi}e^{2(s+ja)(p+ja)}e^{a^2} = \sqrt{\pi}e^{a^2}\sum_{\mathrm{l}=0}^{\infty}\frac{2^{\mathrm{l}}}{\mathrm{l}!}\left(s+ja\right)^{\mathrm{l}}\left(p+ja\right)^{\mathrm{l}}, \qquad (4.80)$$

Expand the term $(p+ja)^{\mathrm{l}}(s+ja)^{\mathrm{l}}$

$$\begin{aligned}\text{L.H.S.} &= \sqrt{\pi}e^{a^2}\sum_{\mathrm{l}=0}^{\infty}\frac{2^{\mathrm{l}}}{\mathrm{l}!}\left[\binom{\mathrm{l}}{\mathrm{l}}s^{\mathrm{l}}+\binom{\mathrm{l}}{\mathrm{l}-1}s^{\mathrm{l}-1}(ja)+\binom{\mathrm{l}}{\mathrm{l}-2}s^{\mathrm{l}-2}(ja)^2+\dots\right.\\ &\left.+\binom{\mathrm{l}}{1}s^1(ja)^{\mathrm{l}-1}+\binom{\mathrm{l}}{0}(ja)^{\mathrm{l}}\right]\cdot\left[\binom{\mathrm{l}}{\mathrm{l}}p^{\mathrm{l}}+\binom{\mathrm{l}}{\mathrm{l}-1}p^{\mathrm{l}-1}(ja)\right.\\ &\left.+\binom{\mathrm{l}}{\mathrm{l}-2}p^{\mathrm{l}-2}(ja)^2+\dots+\binom{\mathrm{l}}{1}p^1(ja)^{\mathrm{l}-1}+\binom{\mathrm{l}}{0}(ja)^{\mathrm{l}}\right], \qquad (4.81)\end{aligned}$$

Reorganize Eq. 4.81 by terms of $s^{\mathrm{m}}p^{\mathrm{n}}$ as follows: (i) $s^{\mathrm{m}}p^{\mathrm{n}}$ appears only for $\mathrm{l} \geq \max(\mathrm{m},\mathrm{n})$; (ii) add all the coefficients of $s^{\mathrm{m}}p^{\mathrm{n}}$ for $\mathrm{l} \geq \max(\mathrm{m},\mathrm{n})$ together. Thus, the total coefficient of $s^{\mathrm{m}}p^{\mathrm{n}}$ can be obtained for $\mathrm{n} \geq \mathrm{m}$

$$\begin{aligned}C(\mathrm{m},\mathrm{n}) &= \sum_{\mathrm{k}=0}^{\infty}\frac{2^{\mathrm{n}+\mathrm{k}}}{(\mathrm{n}+\mathrm{k})\,!}\binom{\mathrm{n}+\mathrm{k}}{\mathrm{n}}(ja)^{\mathrm{k}}\binom{\mathrm{n}+\mathrm{k}}{\mathrm{m}}(ja)^{\mathrm{n}-\mathrm{m}+\mathrm{k}}\\ &= \sum_{\mathrm{k}=0}^{\infty}\frac{2^{\mathrm{n}+\mathrm{k}}}{(\mathrm{n}+\mathrm{k})\,!}\frac{(\mathrm{n}+\mathrm{k})\,!}{\mathrm{n}!\mathrm{k}!}\frac{(\mathrm{n}+\mathrm{k})\,!}{\mathrm{m}!\,(\mathrm{n}+\mathrm{k}-\mathrm{m})\,!}(ja)^{\mathrm{n}-\mathrm{m}+2\mathrm{k}}\\ &= \frac{1}{\mathrm{m}!\mathrm{n}!}\sum_{\mathrm{k}=0}^{\infty}\frac{2^{\mathrm{n}+\mathrm{k}}(\mathrm{n}+\mathrm{k})\,!}{\mathrm{k}!\,(\mathrm{n}-\mathrm{m}+\mathrm{k})\,!}(ja)^{\mathrm{n}-\mathrm{m}+2\mathrm{k}}, \qquad (4.82)\end{aligned}$$

where $\mathrm{k} = \mathrm{l} - \mathrm{n}$. Similarly, the total coefficient for $\mathrm{m} > \mathrm{n}$ can be obtained as

$$C(\mathrm{m},\mathrm{n}) = \frac{1}{\mathrm{m}!\mathrm{n}!}\sum_{\mathrm{k}=0}^{\infty}\frac{2^{\mathrm{m}+\mathrm{k}}(\mathrm{m}+\mathrm{k})!}{\mathrm{k}!(\mathrm{m}-\mathrm{n}+\mathrm{k})!}(ja)^{\mathrm{n}-\mathrm{m}+2\mathrm{k}}, \tag{4.83}$$

Thus, the left hand side of Eq. 4.78 can be expressed as series of $s^{\mathrm{m}}p^{\mathrm{n}}$

$$\text{L.H.S.} = \sqrt{\pi}e^{a^2}\sum_{\mathrm{n}=0}^{\infty}\sum_{\mathrm{m}=0}^{\infty}\frac{s^{\mathrm{m}}p^{\mathrm{n}}}{\mathrm{m}!\mathrm{n}!}\mathcal{G}(\mathrm{m},\mathrm{n}) \tag{4.84}$$

where

$$\mathcal{G}(\mathrm{m},\mathrm{n}) = \begin{cases} \sum_{\mathrm{k}=0}^{\infty}\frac{2^{\mathrm{n}+\mathrm{k}}(\mathrm{n}+\mathrm{k})!}{\mathrm{k}!(\mathrm{n}-\mathrm{m}+\mathrm{k})!}(ja)^{\mathrm{n}-\mathrm{m}+2\mathrm{k}} & \mathrm{n} \geq \mathrm{m} \\ \sum_{\mathrm{k}=0}^{\infty}\frac{2^{\mathrm{m}+\mathrm{k}}(\mathrm{m}+\mathrm{k})!}{\mathrm{k}!(\mathrm{m}-\mathrm{n}+\mathrm{k})!}(ja)^{\mathrm{n}-\mathrm{m}+2\mathrm{k}} & \mathrm{m} > \mathrm{n} \end{cases}. \tag{4.85}$$

Because Eq. 4.78 need to be satisfied by any value of s and p, the coefficient of $s^{\mathrm{m}}p^{\mathrm{n}}$ on the left and right hand side must be equal. Compare the left hand side and the right hand side of Eq. 4.78 term by term,

$$\int_{-\infty}^{\infty} H_{\mathrm{m}}(\xi)\,H_{\mathrm{n}}(\xi)\exp\left(-\xi^2\right)\exp\left(j2a\xi\right)\mathrm{d}\xi = \sqrt{\pi}e^{a^2}\mathcal{G}(\mathrm{m},\mathrm{n}). \tag{4.86}$$

Because of the symmetry of the integral on n and m, we can assume $\mathrm{n} \geq \mathrm{m}$ without loss of generality. Finally, the Hermite integral can be obtained as

$$\begin{aligned} &\int_{-\infty}^{\infty} H_{\mathrm{m}}(\xi)\,H_{\mathrm{n}}(\xi)\exp\left(-\xi^2\right)\exp\left(j2a\xi\right)\mathrm{d}\xi \\ &= \sqrt{\pi}e^{a^2}\sum_{\mathrm{k}=0}^{\infty}\frac{2^{\mathrm{n}+\mathrm{k}}(\mathrm{n}+\mathrm{k})!}{\mathrm{k}!(\mathrm{n}-\mathrm{m}+\mathrm{k})!}(ja)^{\mathrm{n}-\mathrm{m}+2\mathrm{k}} \\ &= \sqrt{\pi}e^{a^2}2^{\mathrm{n}}(ja)^{\mathrm{n}-\mathrm{m}}\sum_{\mathrm{k}=0}^{\infty}\frac{(\mathrm{n}+\mathrm{k})!}{(\mathrm{n}-\mathrm{m}+\mathrm{k})!}\frac{\left(-2a^2\right)^{\mathrm{k}}}{\mathrm{k}!}, \end{aligned} \tag{4.87}$$

from which the orthogonality of Hermite-Gaussian functions (Eq. 4.85) can be easily deduced by setting $a = 0$. When $\mathrm{n} = \mathrm{m}$ (Bragg match), the Hermite integral is simplified as

$$\int_{-\infty}^{\infty} H_{\mathrm{n}}^2(\xi)\exp\left(-\xi^2\right)\exp\left(j2a\xi\right)\mathrm{d}\xi = \sqrt{\pi}e^{a^2}2^{\mathrm{n}}\sum_{\mathrm{k}=0}^{\infty}\frac{(\mathrm{n}+\mathrm{k})!}{(\mathrm{k}!)^2}\left(-2a^2\right)^{\mathrm{k}}. \tag{4.88}$$

With Eqs. 4.87 and 4.88, we can already perform the calculation of the diffraction pattern numerically. But in order to gain more insight into the physical meaning of diffracted field, more concise expression of Hermite integral is essential. In what follows, we will discuss further simplification of the sum series in Eq. 4.87

$$\mathcal{T}(x) = \sum_{\mathrm{k}=0}^{\infty} \frac{(\mathrm{n}+\mathrm{k})\,!}{(\mathrm{n}-\mathrm{m}+\mathrm{k})\,!} \frac{x^{\mathrm{k}}}{\mathrm{k}!}. \tag{4.89}$$

By using the Taylor expansion of exponential functions, $\mathcal{T}(x)$ can be written as

$$\begin{aligned} \mathcal{T}(x) &= x^{\mathrm{m}-\mathrm{n}} \frac{\mathrm{d}^{\mathrm{m}}}{\mathrm{d}x^{\mathrm{m}}} \sum_{\mathrm{k}=0}^{\infty} \frac{x^{\mathrm{k}+\mathrm{n}}}{\mathrm{k}!}, & (4.90) \\ &= x^{\mathrm{m}-\mathrm{n}} \frac{\mathrm{d}^{\mathrm{m}}}{\mathrm{d}x^{\mathrm{m}}} \left(\mathrm{e}^{x} x^{\mathrm{n}}\right). & (4.91) \end{aligned}$$

By using the Rodrigues representation for the associated Laguerre polynomials [73]

$$L_{\beta}^{\alpha}(x) = \frac{1}{\beta!} e^{x} x^{-\alpha} \frac{\mathrm{d}^{\beta}}{\mathrm{d}x^{\beta}} \left(e^{-x} x^{\beta+\alpha}\right) \tag{4.92}$$

we can obtain

$$\begin{aligned} L_{\mathrm{m}}^{\mathrm{n}-\mathrm{m}}(-x) &= \frac{1}{\mathrm{m}!} e^{-x} (-x)^{\mathrm{m}-\mathrm{n}} \frac{\mathrm{d}^{\mathrm{m}}}{\mathrm{d}(-x)^{\mathrm{m}}} \left(e^{x}(-x)^{\mathrm{n}}\right) \\ &= \frac{1}{\mathrm{m}!} e^{-x} x^{\mathrm{m}-\mathrm{n}} \frac{\mathrm{d}^{\mathrm{m}}}{\mathrm{d}x^{\mathrm{m}}} \left(e^{x} x^{\mathrm{n}}\right) & (4.93) \end{aligned}$$

Thus, the function $\mathcal{T}(x)$ can be expressed by Laguerre polynomials as

$$\mathcal{T}(x) = \mathrm{m}! e^{x} L_{\mathrm{m}}^{\mathrm{n}-\mathrm{m}}(-x) \tag{4.94}$$

Furthermore, by using the series representation for the Laguerre polynomials [73]

$$L_{\beta}^{\alpha}(x) = \sum_{\gamma=0}^{\beta} (-1)^{\gamma} \binom{\beta+\alpha}{\beta-\gamma} \frac{x^{\gamma}}{\gamma!}, \tag{4.95}$$

Table 4.1: The $P_{\mathrm{nm}}(x)$ polynomials in the Hermite integral

$P_{\mathrm{nm}}(x)$	n = 0	n = 1	n = 2	n = 3	n=4
m = 0	1	1	1	1	1
m = 1		$x+1$	$x+2$	$x+3$	$x+4$
m = 2			x^2+4x+2	x^2+6x+6	$x^2+8x+12$
m = 3				$x^3+9x^2+18x+6$	$x^3+12x^2+36x+24$
m = 4					$x^4+16x^3+72x^2+96x+24$

the function $\mathcal{T}(x)$ can also be expressed in a finite series as

$$\mathcal{T}(x) = e^x \mathrm{m}! \sum_{\mathrm{k}=0}^{\mathrm{m}} \binom{\mathrm{n}}{\mathrm{m}-\mathrm{k}} \frac{x^{\mathrm{k}}}{\mathrm{k}!}. \tag{4.96}$$

As a summary, we simplify the sum series in Eq. 4.87 as

$$\mathcal{T}(x) = e^x P_{\mathrm{nm}}(x), \tag{4.97}$$

where the m-th order polynomial $P_{\mathrm{nm}}(x)$ is

$$\begin{aligned} P_{\mathrm{nm}}(x) &= \mathrm{m}! L_{\mathrm{m}}^{\mathrm{n}-\mathrm{m}}(-x), & (4.98) \\ &= \sum_{\mathrm{k}=0}^{\mathrm{m}} \binom{\mathrm{n}}{\mathrm{m}-\mathrm{k}} \frac{\mathrm{m}!}{\mathrm{k}!} x^{\mathrm{k}}. & (4.99) \end{aligned}$$

The first few $P_{\mathrm{nm}}(x)$ polynomials are shown in Table 4.1.

Finally, by substituting Eqs. 4.97 into Eq. 4.87, the Hermite integral is obtained analytically as

$$\int_{-\infty}^{\infty} H_{\mathrm{m}}(\xi) H_{\mathrm{n}}(\xi) \exp\left(-\xi^2\right) \exp\left(j2a\xi\right) \mathrm{d}\xi = \sqrt{\pi} 2^{\mathrm{n}} (ja)^{\mathrm{n}-\mathrm{m}} e^{-a^2} P_{\mathrm{nm}}(-2a^2). \tag{4.100}$$

Chapter 5

Diffraction from deformed volume holograms: perturbation theory approach

5.1 Volume holographic imaging systems

It has been proposed to use volume (3D) optical elements as optical imaging elements for various imaging applications [74]. Here, 3D refers to the light interacting with the whole volume, instead of a sequence of surfaces. The latter is the case in lenses, prisms, mirrors and other conventional diffractive optical elements, that we refer to as 2D optical elements. The most general 3D optical element is a volume V with a three dimensional modulation of the dielectric constant $\Delta\epsilon(x, y, z)$. we refer to these elements as 3D diffractive optical elements (A volume hologram is a 3D modulation of the dielectric constant with a carrier $\exp\{i\mathbf{K}_g \cdot \mathbf{r}\}$). As described in Section 4.1, volume holograms can be thought of as self-aligned 3D stacks of diffractive elements operating on the incident field coherently as the field propagates through.

Volume holograms are chosen as optical imaging elements because they provide a larger number of degrees of freedom in defining the optical response, compared to 2D optical elements of the same aperture. This is intuitively obvious from dimensional arguments and was proven formally in Ref. [28, 75] using the modal properties of electromagnetic fields. One interesting consequence of the degrees of freedom afforded by volume holograms is that the shift invariance of these elements can be limited in at least one dimension. This is especially a useful property for 3D imaging systems, e.g. the optical sectioning ability of confocal microscopes can be thought of as resulting from the shift variance of the pinhole response [76].

5.1.1 Volume holographic imaging (VHI)

Gabor originally proposed the use of holography as an imaging method to recover both amplitude and phase of light coming from an object [21] with the intent of using the phase to store and reconstruct 3D information about the object. A Gabor or Leith-Upatnieks [77] hologram is recorded in a thin photosensitive material as the interference pattern between a reference beam and the light scattered by the object. In these applications, the hologram does not function as a fixed imaging element, but rather as a sophisticated detector that captures phase properties of the object.

A different imaging principle, volume holographic imaging (VHI), was proposed in Ref. [74] for 3D imaging. VHI is different from traditional holographic imaging because:

1. A VHI system incorporates at least one thick holographic element, the volume hologram. The volume hologram (which is also referred to as the volume holographic lens) acts as depth selective imaging element to achieve 3D imaging.
2. A single volume holographic lens can be used to image arbitray objects on a CCD camera. Thus, there is no need to record a new hologram for each object as in the case of conventional holographic imaging.

We now describe more specifically how VHI can be used for 3D imaging. The first step is to construct the volume holographic lens. The typical recording process is a sequence of exposures of a photosensitive thick holographic medium, such as a photorefractive crystal or photopolymer. Each exposure is the result of interfering two mutually coherent beams inside the holographic medium. Once recorded, the volume

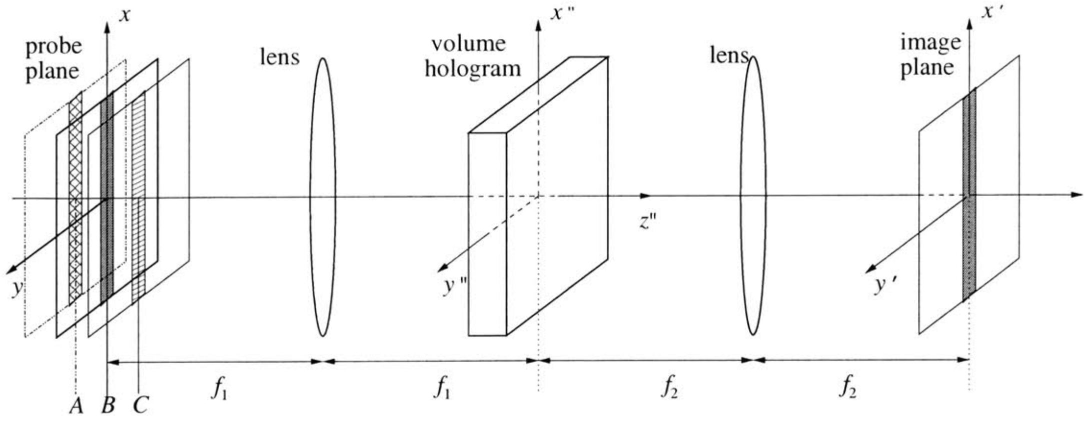

Figure 5-1: Volume holographic imaging system.

hologram is fixed. Light emitted or scattered by the object of interest acts as the probe field on the hologram. Corresponding different demands, such as long working distance [30], the possible "objective optics" may be added between the object and the volume hologram in order to shape the probe field to a more convenient form. For example, in Fig. 5-1 a Fourier lens is used as objective optics.

VHI operates by forming projections of the object on the camera. For example, a useful form of projection that has been used extensively in VHI systems is the so-called "optical slicing," as shown in Fig. 5-1, which can provide similar sectioning ability as do confocal microscopes. The volume hologram in this case can be particularly simple, such as a volume hologram recorded as the interference between two plane waves or a plane wave and a spherical wave. The volume hologram and the objective optics are arranged so as to define a "focal plane", denoted as Plane B in Fig.5-1. Unlike traditional optical systems, in the VHI system only a slit-shaped portion of the object which intersects the focal plane is visible at the image plane; the remainder of the object is invisible. In the VHI system depicted in Fig. 5-1, setting the focal plane at Plane B would results in a slice along Plane B becoming visible while the slices of the object along Plane A and Plane C would be invisible. The optical slicing principle was first implemented with a confocal microscope [78]. In VHI or confocal microscopy, the system rejects light originating away from the focal plane. At the same time, the field of view is limited to a point (confocal microscope with pinhole at detector plane)

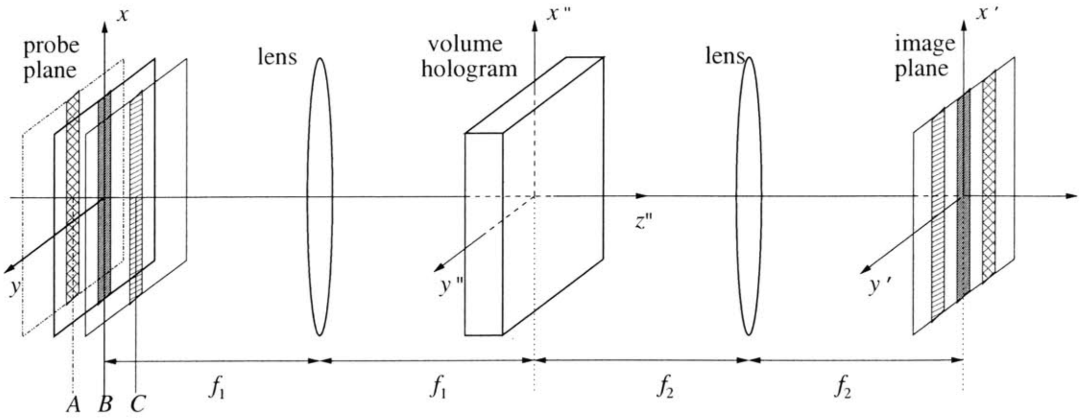

Figure 5-2: The illustration of the multiplex method used in VHI systems.

or a slice (VHI system or confocal microscope with slit-shaped pinhole.) The rest of the object is recovered by scanning in three and two dimensions, respectively.

In the confocal microscope, extensive scanning is the only option to recover the object in its entirety while VHI provides alternatives that reduce or eliminate scanning altogether:

1. Multiplex method: the volume hologram is multiplexed so that multiple slices from the object are simultaneously imaged on non-overlapping segments of a large camera. This unusual imaging mode is to project Plane A, B and C in Fig. 5-2 onto the same image plane, but on non-overlapping segments. It has been implemented experimentally for fluorescent objects [66]. Provided that the dynamic range of the hologram and the photon count are sufficiently high, and that the camera has enough pixels available, the entire 3D object shape can be mapped onto the 2D camera without scanning.
2. Rainbow method: the object is illuminated with a rainbow and each color acts as its own slit and forms independently a depth-selective image on the camera. As shown in Fig. 5-3, different colors form different slits on Plane B while the image of plane B is obtained in one shot on the imaging plane. Scanning in the depth direction only is required to recover the object in its entirety.

In the following section, we will present a derivation of the optical response of

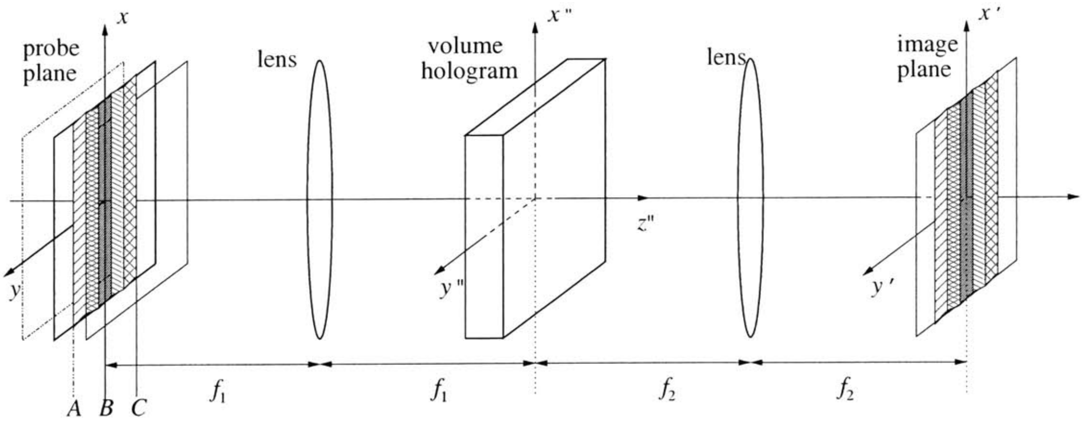

Figure 5-3: The illustration of the rainbow method used in VHI systems.

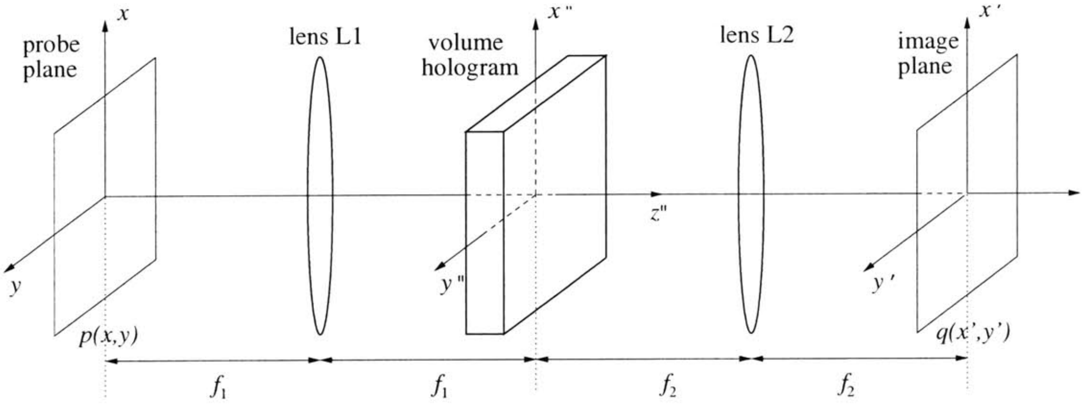

Figure 5-4: The geometry of a VHI system.

VHI that explains how volume holograms operate as imaging elements.

5.1.2 Optical response of VHI

The basic geometry of a VHI system is shown in Fig. 5-4. It consists of a 4F system formed by two ideal thin lens as L1 and L2 of focal lengths f_1 and f_2, respectively. At the front focal plane of L1, the light distribution is assumed to be monochromatic and spatially coherent, with wavelength λ and amplitude $p(x, y)$. Our goal is to determine the light amplitude distribution $q(x', y')$ at the back focal plane of L2.

If a thin transparency (amplitude or phase) is placed at the shared focal plane of the lenes in Fig. 5-4, it is well known that the transparency acts as a Fourier-plane filter, called "pupil function." The significant difference in the VHI system is that the Fourier filter is 3D. As a result, the filter behavior changes qualitatively: for example, we will see that the shift invariance property is destroyed. The loss of shift invariance is especially useful in the sectioning of 3D imaging. Furthermore, the 3D nature of the pupil permits more degrees of freedom in determining the optical response.

Let $\Delta\epsilon(x'', y'', z'')$ denote the 3D modulation of dielectric constant in the vicinity of the shared focal plane. If the modulation has a spatial carrier, it can be written in analytic form as

$$\Delta\epsilon(x'', y'', z'') = \Delta\epsilon_b(x'', y'', z'') \times \exp\{i\mathbf{K} \cdot \mathbf{r}''\}. \tag{5.1}$$

where $\mathbf{r}'' \equiv (x'', y'', z'')$ is the position vector with respect to a coordinate system centered at the hologram, $\mathbf{K} = (K_x, K_y, K_z)$ is a grating vector, and $\Delta\epsilon_b(x'', y'', z'')$ is a baseband (low-frequency) modulation. We will call $\Delta\epsilon(x'', y'', z'')$ a "volume hologram." In this chapter, we will only be considering modulations of the volume holographic type.

The field generated by propagating $p(x, y)$ through L1 to the vicinity of the shared focal plane is given by

$$\begin{aligned} P(x'', y'', z'') = \exp\left\{i2\pi\frac{z''}{\lambda}\right\} \iint p(x, y) \exp\left\{-i2\pi\frac{xx'' + yy''}{\lambda f_1}\right\} \\ \times \exp\left\{-i\pi\frac{(x^2 + y^2)z''}{\lambda f_1^2}\right\} \mathrm{d}x\mathrm{d}y. \end{aligned} \tag{5.2}$$

Here we neglect the amplitude terms $1/i\lambda z''$ from the expressions for spherical waves. These terms contribute little to the diffraction integrals, in comparison with the fast varying exponentials.

It is clear from Eq. 5.2 that $P(x'', y'', 0)$ reduces to the 2D Fourier transform of $p(x, y)$. According to the first order Born approximation, the modulated 3D dielectric material responds to illumination by $P(x'', y'', z'')$ as a superposition of secondary point sources of amplitude

$$g(x'', y'', z'') = P(x'', y'', z'') \times \Delta\epsilon(x'', y'', z'') \tag{5.3}$$

at each point (x'', y'', z'') inside the volume hologram.

By using Eq. 4.10, we can calculate the diffracted field after the back surface of the hologram at observation coordinates (x_b, y_b, z_b). Under the paraxial approximation (Eq. 4.12), the diffracted field due to the superposition of secondary point sources is

$$\begin{aligned} e(x_b, y_b, z_b) &= \iiint g(x'', y'', z'') \exp\left\{ i2\pi \frac{z_b - z''}{\lambda} \right\} \\ &\quad \times \exp\left\{ i\pi \frac{(x_b - x'')^2 + (y_b - y'')^2}{\lambda(z_b - z'')} \right\} \mathrm{d}x''\mathrm{d}y''\mathrm{d}z''. \end{aligned} \tag{5.4}$$

The most natural selection for z_b in the above equation is $z_b = f_2$, to the left of and immediately adjacent to L2. This selection, as long as the hologram is confined near the shared focal plane, as shown in Fig. 5-4, enures that the paraxial approximation of Eq. 4.12 used in Eq. 5.4 for the free space Green function remains valid. We have also avoided the potential singularity that would occur if z_b were allowed to be inside the volume hologram.

The system output is the field generated by L2 at its back focal plane when the illumination immediately to the left of L2 is $e(x_b, y_b, f_2)$, according to Eq. 5.4. From Fourier optics, we find

$$\begin{aligned} q(x', y') = \exp\left\{ i\pi \frac{x'^2 + y'^2}{\lambda f_2} \right\} \iint \exp\left\{ -i2\pi \frac{x_b x' + y_b y'}{\lambda f_2} \right\} \\ \times e(x_b, y_b, f_2)\mathrm{d}x_b\mathrm{d}y_b. \end{aligned} \tag{5.5}$$

Combining integrals Eqs. 5.4 and 5.5 and performing the x_b and y_b integrations first, the result is

$$\begin{aligned} q(x', y') &= \iiint g(x'', y'', z'') \exp\left\{ -i2\pi \frac{x'x'' + y'y''}{\lambda f_2} \right\} \\ &\quad \times \exp\left\{ -i2\pi \left(1 - \frac{x'^2 + y'^2}{2f_2^2} \right) \frac{z''}{\lambda} \right\} \mathrm{d}x''\mathrm{d}y''\mathrm{d}z''. \end{aligned} \tag{5.6}$$

which can be written in a simplified form as

$$q(x',y') = G\left[\frac{x'}{\lambda f_2}, \frac{y'}{\lambda f_2}, \frac{1}{\lambda}\left(1 - \frac{x'^2+y'^2}{2f_2^2}\right)\right], \tag{5.7}$$

where $G(u,v,w)$ is the 3D spatial Fourier transform of $g(x'',y'',z'')$. Eq. 5.7 is general, within the limits of validity of our approximations. As with any linear system, of particular interest is the special case $p(x,y) = \delta(x-x_0)\delta(y-y_0)$, which gives us the impulse response $h(x',y';x_0,y_0)$ of the VHI system. By direct substitution to Eqs. 5.2, 5.3 and 5.7, we obtain

$$h(x',y';x_0,y_0) = \mathcal{E}\left[\frac{1}{\lambda}\left(\frac{x_0}{f_1} + \frac{x'}{f_2}\right), \frac{1}{\lambda}\left(\frac{y_0}{f_1} + \frac{y'}{f_2}\right), \frac{1}{\lambda}\left(\frac{x_0^2+y_0^2}{2f_1^2} - \frac{x'^2+y'^2}{2f_2^2}\right)\right]. \tag{5.8}$$

where $\mathcal{E}(u,v,w)$ denotes the 3D spatial Fourier transform of the dielectric modulation $\epsilon(x'',y'',z'')$. Therefore, the system input-output relation can also be written as

$$q(x',y') = \iint p(x,y)h(x',y';x,y)\mathrm{d}x\mathrm{d}y. \tag{5.9}$$

It is evident from the impulse response Eq. 5.8 that the VHI system is not shift invariant. It should also be noted that the 3D pupil does not lead to three degrees of freedom in determining the impulse response. Instead, the impulse response at any given field point (x',y') remains limited to two degrees of freedom, but the shift variance introduced by the 3D pupil provides a means of controlling the impulse response as function of field coordinates (x',y'). Another way to understand Eq. 5.7 is that the impulse response is defined on a 2D manifold in the space of the Fourier transform of 3D pupil. As is evident from Eq. 5.7, the manifold shape is specified by the field coordinates (x',y').

From Eq. 5.8, we know that the Fourier transform of the dielectric modulation can obtained by using simple point source at the probe plane. This provides a way to inspect the change of the dielectric modulation, for example, through determining the change of the dielectric modulation we can know the deformation which causes the change. Since the dielectric modulation is in a 3D volume, this method can be used to detect arbitrary 3D deformations inside a transparent material with a pre-recorded hologram. This is the topic of the rest of this chapter.

5.2 3D deformation measurement

Deformation of volume holograms, such as shrinkage during processing [79, 80], or elastic deformation due to the action of a force can cause deviation in the angle or wavelength for Bragg matching condition [81, 82], and aberrations in the reconstructed image [83]. This problem, usually associated with the investigation of holographic materials, has received much attention since holography was invented [84, 85]. It is a significant source of concern in application areas such as holographic memories [86, 87], information processing [88], interconnects [89], and imaging applications [30]. For example, researchers have investigated polymer materials with minimal shrinkage [23, 90, 91, 92] and how to compensate the deviation due to shrinkage [93, 94]. Based on shrinkage only, the models used in the literature are relatively simple, treating linear deformation only. In this paper, we present a generalized theory which can deal with arbitrary deformations.

Deformation can be thought of as a two sided problem: one side is how to avoid it, the other is how to measure it. Deformation measurement has been intensively investigated during the past thirty years [95, 96, 97, 98, 99], but it has been exclusively limited to two dimensional (2D) measurements of surface deformation. The universal principle applied to this problem consists of first producing an interferogram, *i.e.* modulating a signature of the surface before deformation as a phase modulation on an optical carrier. When the interferogram is mixed with the signature of the deformed surface, the beat term corresponds to the difference, *i.e.* the deformation. The mixing can be performed optically or digitally. Optical mixing is usually referred to as "holographic interferometry" [95, 96] if the beating is with an interferogram recorded on photographic film, and "moiré interferometry" [98, 99] if the beating is between two sets of intensity fringes recorded on a digital camera. Digital mixing is called "speckle interferometry," [97] where the speckle is interpreted as a random phase mask; then the beating is the crosscorrelation function of the mask before and after deformation. Digital holography [100, 101] can also be thought of in similar terms, especially in the context of holographic particle image velocimetry [102, 103], where instead of deformation one measures displacement of particles in a thin sheet of moving fluid.

Three dimensional (3D) deformation measurement is more challenging because mixing and beating must occur throughout an entire volume as the optical fields propagate through. This eliminates both film and digital cameras as possible media for recording the interferograms. In this chapter, we propose instead the use of Bragg diffraction for 3D deformation measurement. The mixing step is the recording of a volume hologram in a transparent 3D medium before it is deformed. The hologram is then reconstructed in the presence of an unknown 3D deformation and the diffracted intensity is captured on a digital camera. Examples are shrinkage, shear, compression, indentation, crack propagation, etc. Assuming the deformation is not severe enough to destroy the optical quality of the medium, the diffracted field is, in effect, the 3D beat between the deformed and undeformed versions.

Since the diffracted intensity is measured on a digital camera, which is a 2D medium, the beating signature is captured as a *projection* rather than a direct image. This implies that, in general, more than one measurement is required to capture the complete 3D deformation field. Nevertheless, our proposed technique is the first measurement method, to our knowledge, that is explicitly designed to handle 3D deformations in optically transparent media.

In this chapter, we deal exclusively with the "forward" problem of establishing the beat field when the volume hologram and the 3D deformation are both known. Surprisingly, there have been no efforts to that end in the literature to date, except for the special case of linear shrinkage. Here we provide general expressions that are applicable to arbitrary deformations under a set of mildly restrictive assumptions, such as preservation of the average index of refraction and validity of the 1^{st}-order Born approximation. The derivation is carried out in section 5.3 for small deformations for which a perturbative approach is adequate, and in a more general (but also more algebraically complex) form in sections 5.6 and 5.7. In section 5.4, we confirm that the general theory matches with the well known predictions and observations of shrinkage effects from the literature. In section 5.5, we carry out the modeling of the diffracted field and report experimental results in the case of a deformation produced by an indenter tip applied against the surface of a semi-infinite slab. The experiments match very well with the theory.

The solution to the forward problem, which we are presenting here, is always the first step before the "inverse" problem, *i.e.* the measurement of arbitrary deformations from a set of diffracted intensity measurements in our case, can be attacked. The inverse problem usually poses additional challenges involving the efficacy of the measurement and the well-posedness of the solution. This will very clearly be the case in our approach, since the measurement is that of a projection, as we already noted. Fortunately, in many cases of interest, including the indentation problem, existing analytical or numerical models of 3D deformation can be used to extract deformation parameters even from a single measurement. In these cases, the formulation presented in this chapter is adequate.

5.3 Perturbation Theory on the Deformation of Volume Holograms

Consider a volume hologram with dielectric modulation $\Delta\epsilon(x, y, z)$ which changes to $\Delta\epsilon'(x', y', z')$ after deformation, as shown in Fig. 5-5. Our goal is to derive an expression for the diffracted field when the deformed hologram is probed by an arbitrary light field. With the assumption that the dielectric constant of each point inside the hologram does not change when that point moves due to the deformation, we can express $\Delta\epsilon'(x', y', z')$ as

$$\Delta\epsilon'(x', y', z') = \Delta\epsilon(f_x(x', y', z'), f_y(x', y', z'), f_z(x', y', z')), \tag{5.10}$$

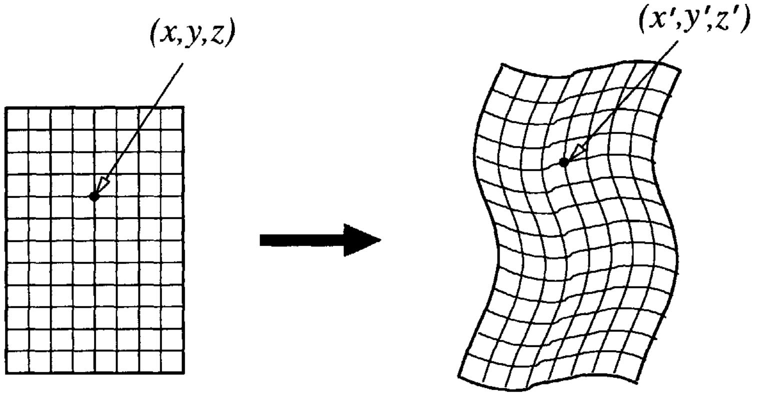

Figure 5-5: Deformation of holograms

where $\mathbf{f}(\mathbf{r}') = \hat{\mathbf{x}} f_x(x',y',z') + \hat{\mathbf{y}} f_y(x',y',z') + \hat{\mathbf{z}} f_z(x',y',z')$ is the former position of the point at $\mathbf{r}' = \hat{\mathbf{x}}x' + \hat{\mathbf{y}}y' + \hat{\mathbf{z}}z'$, and it can be obtained from the strain or displacement functions. This assumption is valid when the deformation is not large enough to affect the material properties of the hologram. We refer to these weak deformations as "conformal." The conformality condition is satisfied for most cases. An expression for the diffracted field for general non–conformal deformations is given in Section 5.6.

Returning to the case of conformal deformation, we write Equation 5.10 in vector form as

$$\Delta\epsilon'(\mathbf{r}') = \Delta\epsilon(\mathbf{f}(\mathbf{r}')), \tag{5.11}$$

When the displacement is analytic, we can approximate Equation 5.11 by N-th order Taylor expansion as

$$\Delta\epsilon(\mathbf{f}(\mathbf{r}')) \approx \Delta\epsilon(\mathbf{r}') + \sum_{j=1}^{N} \frac{[(\mathbf{f}(\mathbf{r}') - \mathbf{r}') \cdot \nabla]^j}{j!} \Delta\epsilon(\mathbf{r}'). \tag{5.12}$$

Without loss of generality, we can restrict $\Delta\epsilon(\mathbf{r}')$ to a set of planar, parallel grating fringes recorded by two intersecting plane waves: reference beam $E_{\mathrm{f}}(\mathbf{r}) = \exp(\imath \mathbf{k}_{\mathrm{f}} \cdot \mathbf{r})$ and signal beam $E_{\mathrm{S}}(\mathbf{r}) = \exp(\imath \mathbf{k}_{\mathrm{S}} \cdot \mathbf{r})$. This is because any hologram can be regarded as a linear superposition of infinite plane–wave holograms[1]. In most cases, the superposition is straightforward and numerically stable. We prefer the development of the perturbation theory using the plane–wave holograms because it leads to simpler, more intuitive expressions. The perturbation theory for non–plane–wave holograms is discussed in Section 5.7. For a plane–wave hologram, the undeformed dielectric modulation can be written in analytic form as

$$\Delta\epsilon(\mathbf{r}') = \epsilon_1 \exp\left(i\mathbf{K_g}\cdot\mathbf{r}'\right), \tag{5.13}$$

where ϵ_1 is the amplitude of the spatial modulation expressing the hologram strength and $\mathbf{K_g} = \mathbf{k_S} - \mathbf{k_f}$ is the wave vector of the grating. Its j-th order derivative can be obtained as

$$\nabla^j \Delta\epsilon(\mathbf{r}') = (i\mathbf{K_g})^j\, \Delta\epsilon(\mathbf{r}'), \tag{5.14}$$

$$\nabla \rightarrow i\mathbf{K_g}. \tag{5.15}$$

Substituting Equation 5.15 into Equation 5.12, we obtain

$$\Delta\epsilon(\mathbf{f}(\mathbf{r}')) \approx \Delta\epsilon(\mathbf{r}') + \sum_{j=1}^{N} \frac{[\Delta\mathbf{f}(\mathbf{r}')\cdot i\mathbf{K_g}]^j}{j!}\Delta\epsilon(\mathbf{r}'), \tag{5.16}$$

where $\Delta\mathbf{f}(\mathbf{r}') = \mathbf{f}(\mathbf{r}') - \mathbf{r}'$ is the displacement due to the deformation. The displacement can be expressed as

$$\Delta\mathbf{f}(\mathbf{r}') = \begin{bmatrix} \Delta f_x(x',y',z') \\ \Delta f_y(x',y',z') \\ \Delta f_z(x',y',z') \end{bmatrix} = \begin{bmatrix} a_{11} & a_{12} & a_{13} \\ a_{21} & a_{22} & a_{23} \\ a_{31} & a_{32} & a_{33} \end{bmatrix} \begin{bmatrix} x' \\ y' \\ z' \end{bmatrix} = A\cdot\mathbf{r}', \tag{5.17}$$

where, in general, a_{kl} is a function of (x', y', z') for all $k, l = 1, 2, 3$. The matrix A is referred to as "strain matrix" or "deformation matrix." In special cases, e.g. uniform shrinkage of a volume hologram, A is constant and very simple expressions of the diffracted field can be derived. Our analysis remains valid for constant as well as non-constant deformation matrices. Using Equation 5.17, Equation 5.16 can be written as

$$\Delta\epsilon(\mathbf{f}(\mathbf{r}')) \approx \Delta\epsilon(\mathbf{r}') + \sum_{j=1}^{N} \frac{[\mathbf{K_g}\cdot A\cdot i\mathbf{r}']^j}{j!}\Delta\epsilon(\mathbf{r}'). \tag{5.18}$$

Using relation 5.13, we can see that the dielectric modulation is a function not only of $\mathbf{r}'$ but also of $\mathbf{K_g}$. Therefore, we can swap derivatives and write the conjugate of equations 5.14 and 5.15 as

$$\nabla^j_{\mathbf{K_g}} \Delta\epsilon(\mathbf{r}') = (i\mathbf{r}')^j \, \Delta\epsilon(\mathbf{r}'), \tag{5.19}$$

$$i\mathbf{r}' \to \nabla_{\mathbf{K_g}}. \tag{5.20}$$

By substituting equation 5.20 into equation 5.18, we can obtain the deformed dielectric modulation as

$$\Delta\epsilon(\mathbf{f}(\mathbf{r}')) \approx \Delta\epsilon(\mathbf{r}') + \sum_{j=1}^{N} \frac{\left[\mathbf{K_g} \cdot A \cdot \nabla_{\mathbf{K_g}}\right]^j}{j!} \Delta\epsilon(\mathbf{r}'). \tag{5.21}$$

With the knowledge of the deformed dielectric modulation, we can calculate the diffracted field change in the Fourier geometry as shown in Fig. 5-6. Before deformation, when an arbitrary probe beam $E_{\mathrm{p}}(\mathbf{r})$ is used to read out the volume hologram, the diffracted field incident on the detector is [2]

$$\begin{aligned} E_{\mathrm{d}}(\mathbf{r}'') \;=\; & \iiint E_{\mathrm{p}}(\mathbf{r}) \Delta\epsilon(\mathbf{r}) V(\mathbf{r}) \exp\left(-i\frac{2\pi}{\lambda}\frac{xx'' + yy''}{F}\right) \\ & \exp\left[-i\frac{2\pi}{\lambda}\left(1 - \frac{x''^2 + y''^2}{2F^2}\right) z\right] d^3\mathbf{r}, \end{aligned} \tag{5.22}$$

where the index function $V(\mathbf{r})$ is defined as

$$V(\mathbf{r}) = \begin{cases} 1 & \text{inside the volume hologram} \\ 0 & \text{outside the volume hologram} \end{cases}, \tag{5.23}$$

F is the focal length of the Fourier lens between the hologram and the detector, and $\mathbf{r}'' = \hat{\mathbf{x}}x'' + \hat{\mathbf{y}}y''$ is the coordinate on the camera plane. In fact, Equation 5.22 is the 3-D Fourier transform of $E_{\mathrm{p}}(\mathbf{r})\Delta\epsilon(\mathbf{r})V(\mathbf{r})$ computed at spatial frequency coordinates $f_{\mathrm{x}} = x''/(\lambda F), f_{\mathrm{y}} = y''/(\lambda F), f_{\mathrm{z}} = (1/\lambda)[1 - (x''^2 + y''^2)/(2F^2)]$.

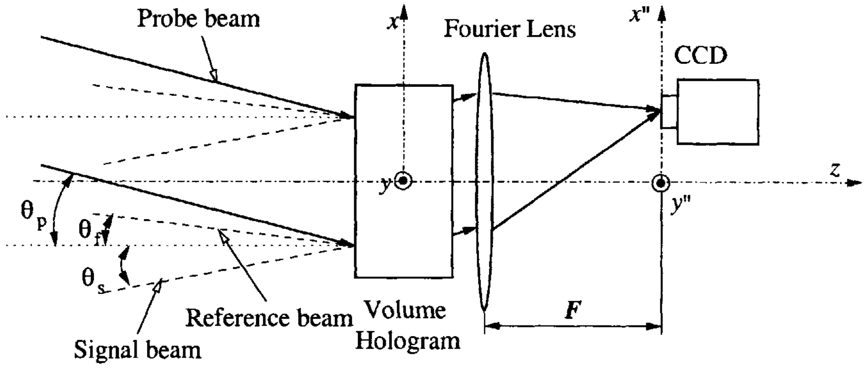

Figure 5-6: Fourier geometry with plane wave reference and plane wave signal

After deformation, the diffracted field changes to

$$\begin{aligned}\tilde{E}_{\mathrm{d}}(\mathbf{r}'') &= \iiint E_{\mathrm{p}}(\mathbf{r}')\Delta\epsilon'(\mathbf{r}')\tilde{V}(\mathbf{r}')\exp\left(-i\frac{2\pi}{\lambda}\frac{x'x''+y'y''}{F}\right)\\ &\quad \exp\left[-i\frac{2\pi}{\lambda}\left(1-\frac{x''^2+y''^2}{2F^2}\right)z'\right]d^3\mathbf{r}', \qquad (5.24)\end{aligned}$$

Since the hologram shape should remain approximately constant, except under very severe deformation, and in any case changes in index function affect only the boundary of the volume integral, we approximate $\tilde{V}(\mathbf{r}') \approx V(\mathbf{r})$. Thus by substituting Equations 5.11 and 5.21, we can obtain

$$\begin{aligned}\tilde{E}_{\mathrm{d}}(\mathbf{r}'') &\approx E_{\mathrm{d}}(\mathbf{r}'') + \iiint E_{\mathrm{p}}(\mathbf{r}')\sum_{j=1}^{N}\frac{\left[\mathbf{K_g}\cdot A\cdot\nabla_{\mathbf{K_g}}\right]^j}{j!}\Delta\epsilon(\mathbf{r}')\\ &\quad V(\mathbf{r}')\exp\left(-i\frac{2\pi}{\lambda}\frac{x'x''+y'y''}{F}\right)\\ &\quad \exp\left[-i\frac{2\pi}{\lambda}\left(1-\frac{x''^2+y''^2}{2F^2}\right)z'\right]d^3\mathbf{r}', \qquad (5.25)\end{aligned}$$

Inside the integral, $\mathbf{K_g}$ and $\nabla_{\mathbf{K_g}}$ do not depend on $\mathbf{r}'$. Therefore, if the displacement can be linearized (in which case A is a constant matrix), we can take $\left[\mathbf{K_g}\cdot A\cdot\nabla_{\mathbf{K_g}}\right]^j/(j!)$ out of the integral and obtain the final result in a very simple form as

$$\tilde{E}_{\mathrm{d}}(\mathbf{r}'') \approx E_{\mathrm{d}}(\mathbf{r}'') + \sum_{j=1}^{N}\frac{\left[\mathbf{K_g}\cdot A\cdot\nabla_{\mathbf{K_g}}\right]^j}{j!}E_{\mathrm{d}}(\mathbf{r}''). \qquad (5.26)$$

Especially, for the first order approximation in the Taylor series,

$$\tilde{E}_{\mathrm{d}}(\mathbf{r}'') \approx E_{\mathrm{d}}(\mathbf{r}'') + \mathbf{K_g} \cdot A \cdot \nabla_{\mathbf{K_g}} E_{\mathrm{d}}(\mathbf{r}''). \tag{5.27}$$

The final expression is very similar to the standard form of the perturbation theory on electromagnetism [104].

With Equation 5.25 or 5.26, we can already perform the calculation of diffracted field change due to deformation. Before doing so, it is worthwhile to look at these equations qualitatively in some detail. First interesting result is that $\mathbf{K_g} \cdot A \cdot \nabla_{\mathbf{K_g}}$ has null space when $A^T \cdot \mathbf{K_g}$ is perpendicular to $\nabla_{\mathbf{K_g}}$ or $A^T \cdot \mathbf{K_g}$ is equal to 0, meaning that there exist holograms which have zero response for a given deformation. For example, if there is a hologram with its grating fringes along the z–direction (the wave vector of the grating $\mathbf{K_g}$ is in the x-y plane), the deformation along the z–direction will have no effect on it. This is intuitively obvious, and it is useful if we desire to minimize the effect of an anticipated deformation (e.g. shrinkage) on the hologram. Second, if our goal is to measure a certain deformation, then we can find some optimal holograms which have maximum sensitivity to that deformation. The condition is

$$A^T \cdot \mathbf{K_g} \parallel \nabla_{\mathbf{K_g}} \tag{5.28}$$

Condition 5.28 also has an intuitive interpretation with the help of the K–sphere, as shown in Fig. 5-7. Usually when the probe beam is Bragg matched before deformation, $E_{\mathrm{p}}(\mathbf{r}) = \exp(i\mathbf{k}_{\mathrm{f}} \cdot \mathbf{r})$, the strongest dependence of E_{d} on $\mathbf{K_g}$ is when a change in $\mathbf{K_g}$ leads to Bragg mismatch fastest. The mismatch $\Delta\mathbf{K_g}$ is fastest when the tip of the grating vector after deformation moves as fast as possible away from the K–sphere, which is along the direction connecting the center of the K–sphere to the tip of the grating vector on the K–sphere. This is actually the same as the direction of the signal beam $\mathbf{k}_{\mathrm{S}}$. The locus of the maximum Bragg mismatch as function of deformation δ is calculated in Section 5.8, where it is shown that the maximum Bragg mismatch

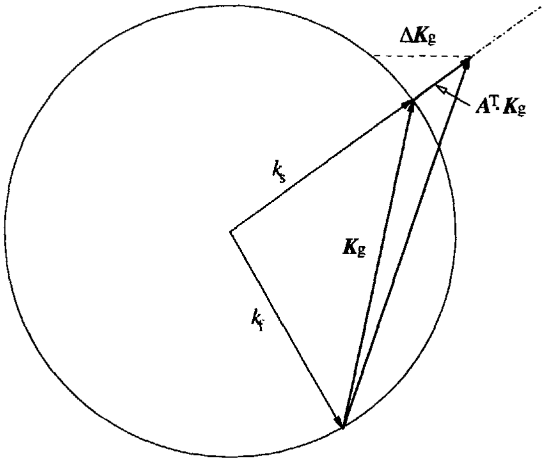

Figure 5-7: K–sphere explanation of Condition 5.28

direction angle θ_δ is

$$\sin\theta_\delta = \frac{k\sin\theta_S}{k-\delta}, \tag{5.29}$$

where $k = 2\pi/\lambda$ is the wave number and θ_S is the direction angle of signal beam. The sketch of the locus of the maximum Bragg mismatch is shown in Fig. 5-8.

From another point of view, $\nabla_{\mathbf{K_g}} E_\mathrm{d}(\mathbf{r}'')$ means the gradient of $E_\mathrm{d}(\mathbf{r}'')$ with respect to $\mathbf{K_g}$. If the plane–wave hologram with grating vector $\mathbf{K_g}$ is probed by $E_\mathrm{p}(\mathbf{r}) = \exp\left(i\mathbf{k}_\mathrm{p}\cdot\mathbf{r}\right)$, without deformation the diffracted field just after the hologram before the Fourier lens can be obtained from the generalization of Eq. 4.17 as

$$\begin{aligned} E_\mathrm{d}(\mathbf{r}'') \;=\; & \operatorname{sinc}\left\{\frac{L}{2\pi}\left[K_\mathrm{gz}+k_\mathrm{pz}-\sqrt{k^2-\left(K_\mathrm{gx}+k_\mathrm{px}\right)^2-\left(K_\mathrm{gy}+k_\mathrm{py}\right)^2}\right]\right\} \\ & \exp\left\{i\left[\left(K_\mathrm{gx}+k_\mathrm{px}\right)x''+\left(K_\mathrm{gy}+k_\mathrm{py}\right)y''+\right.\right. \\ & \left.\left.+\sqrt{k^2-\left(K_\mathrm{gx}+k_\mathrm{px}\right)^2-\left(K_\mathrm{gy}+k_\mathrm{py}\right)^2}z''\right]\right\}, \end{aligned} \tag{5.30}$$

which is a plane wave with amplitude modulated by Bragg mismatch. Here, we assumed that the dimensions of the hologram are infinite in the $x-$ and $y-$ directions, and the thickness of the hologram is L . We can calculate the diffracted field gradient

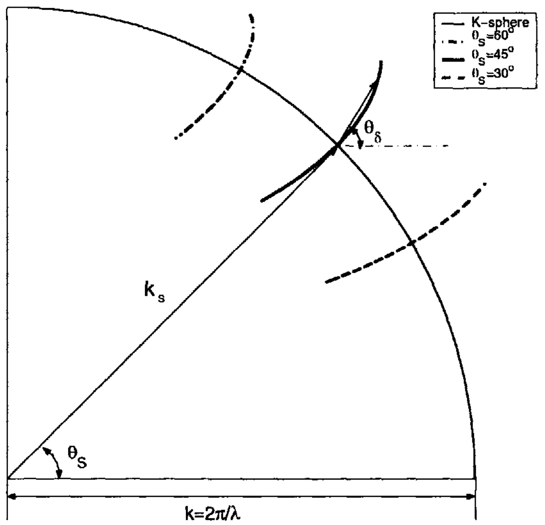

Figure 5-8: The locus of maximum Bragg mismatch

as

$$\begin{aligned}\nabla_{\mathbf{K_g}} E_{\mathrm{d}}(\mathbf{r}'') \;\propto\; & (K_{\mathrm{gx}} + k_{\mathrm{px}})\,\hat{x} + (K_{\mathrm{gy}} + k_{\mathrm{py}})\,\hat{y} + \\ & + \sqrt{k^2 - (K_{\mathrm{gx}} + k_{\mathrm{px}})^2 - (K_{\mathrm{gy}} + k_{\mathrm{py}})^2}\,\hat{z}, \qquad (5.31)\end{aligned}$$

which is also along the direction connecting the center of K–sphere to the tip of the grating vector, consistent with our earlier K–sphere analysis. According to Condition 5.28, the deformed grating vector $A^T \cdot \mathbf{K_g}$ must point in this direction to achieve maximum change. Or if we want to measure certain deformation A, the hologram whose grating vector $\mathbf{K_g}$ satisfies condition 5.28 will have maximum sensitivity to this deformation A.

5.4 Application to Linear Deformation (Shrinkage)

Equations 5.26 and 5.27 can be applied to linear deformation directly, e.g. the shrinkage of holograms, or compression by uniform pressure on the surface of holograms. The diffracted field after deformation can be calculated without complicated and time-consuming numerical integrations.

The shrinkage of holograms has been observed to cause angular deviation and/or wavelength shift for maximum diffraction-efficiency reconstruction [82, 81, 93] and to cause aberrations[83]. Using the perturbation theory from section 5.3, it can be investigated very conveniently. Here, it is assumed that the shrinkage occurs only along the direction of the normal to the hologram's surface. A hologram of original thickness L shrinks to thickness L' such that

$$L' = (1 - s)L, \tag{5.32}$$

where s is the coefficient of shrinkage. Thus, the displacement matrix is

$$A = \begin{bmatrix} 0 & 0 & 0 \\ 0 & 0 & 0 \\ 0 & 0 & s \end{bmatrix}, \tag{5.33}$$

If the plane-wave hologram with grating vector $\mathbf{K_g}$ is probed by $E_\mathrm{p}(\mathbf{r}) = \exp(i\mathbf{k}_\mathrm{p} \cdot \mathbf{r})$, without shrinkage the diffracted field just after the hologram is given by Equation 5.30. By substituting 5.33 and 5.30 into the perturbation formulae 5.26, the result after shrinkage can be simplified as

$$\begin{aligned} \tilde{E}_\mathrm{d}(\mathbf{r}'') &\approx E_\mathrm{d}(\mathbf{r}'') + \sum_{j=1}^{N} \frac{\left[K_\mathrm{gz} s \frac{\partial}{\partial K_\mathrm{gz}}\right]^j}{j!} E_\mathrm{d}(\mathbf{r}'') \\ &= \mathrm{sinc}\left\{\frac{L}{2\pi}\left[(1+s)\,K_\mathrm{gz} + k_\mathrm{gz} - \sqrt{k^2 - (K_\mathrm{gx}+k_\mathrm{px})^2 - (K_\mathrm{gy}+k_\mathrm{py})^2}\right]\right\} \\ &\quad \exp\left\{i\left[(K_\mathrm{gx}+k_\mathrm{px})\,x'' + (K_\mathrm{gy}+k_\mathrm{py})\,y'' + \right.\right. \\ &\quad \left.\left. + \sqrt{k^2 - (K_\mathrm{gx}+k_\mathrm{px})^2 - (K_\mathrm{gy}+k_\mathrm{py})^2}\, z''\right]\right\} \end{aligned} \tag{5.34}$$

which means that the shrinkage along z-direction affects only the efficiency but not the direction of the diffracted plane wave. This is consistent with the discussions in Ref. [81, 93]. Beyond this simple calculation, equation 5.26 can be used to predict the response of holograms deformed under any kind of affine transformations, including rotations, anisotropic shrinkage, etc.

5.5 Application to Nonlinear Deformation

For holograms which undergo nonlinear deformation, we have to use the full 3-D integral or Fourier transform in Equation 5.25 to predict the diffracted field. In order to verify the validity of the perturbation theory on nonlinear deformation, we simulated the change in the diffracted field due to a point load exerted normally on the surface of a hologram. We also carried out an experiment and compared the results with the simulation.

When a concentrated point force P is acting normally to the surface of an elastic solid, as shown in Fig. 5-9(a), the elastic displacements at any point in the half space are given by [105]

$$\begin{aligned} u_{\mathrm{x}} &= \frac{P}{4\pi G}\left[\frac{xz}{\rho^3} - (1-2\nu)\frac{x}{\rho(\rho+z)}\right], \\ u_{\mathrm{y}} &= \frac{P}{4\pi G}\left[\frac{yz}{\rho^3} - (1-2\nu)\frac{y}{\rho(\rho+z)}\right], \\ u_{\mathrm{z}} &= \frac{P}{4\pi G}\left[\frac{z^2}{\rho^3} + \frac{2(1-\nu)}{\rho}\right], \end{aligned} \tag{5.35}$$

where G and ν are the shear modulus and Poisson ratio, respectively; and $\rho = \sqrt{x^2+y^2+z^2}$ is the distance of the point to the origin (loading position). The resulting deformation is shown in Fig. 5-9(b). The singularity at $\rho = 0$ is due to the δ-function nature of the point load. We can obtain the displacement matrix for each point in the deformed solid. Note that the displacement matrix elements are now position–dependent, unlike the example in the previous section.

We constructed an experimental setup to verify the validity of the approach presented above. The holographic material was provided by Ondax, Inc. It had thickness $L = 2\mathrm{mm}$ and measured shear modulus $G = 44\mathrm{GPa}$, Poisson ratio $\nu = 0.22$. The hologram was of the transmission type with reference and signal beam angles $\theta_{\mathrm{f}} = -7.5^\circ$ and $\theta_{\mathrm{S}} = 20^\circ$, respectively, at wavelength of 488nm. The geometry of the experiment is shown in Fig. 5-10 with $F = 400\mathrm{mm}$. The hologram was illuminated at the Bragg matched angle. A PULNiX TM-7EX CCD with 768 × 494 pixels, pixel size $8.4\mu\mathrm{m} \times 9.8\mu\mathrm{m}$ was used to observe the diffracted intensity. The hologram was

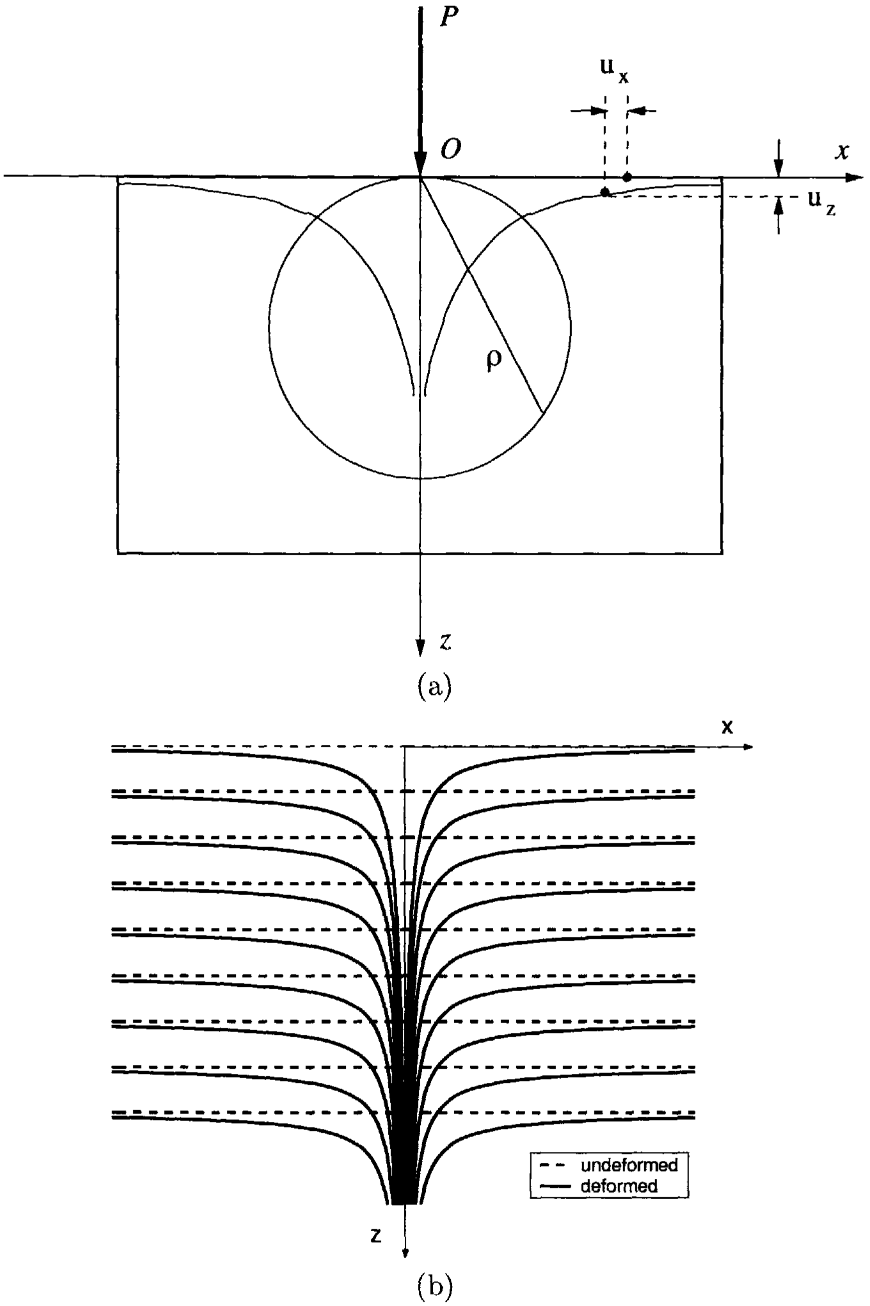

Figure 5-9: Illumination of the deformation when a point load is exerted on half space: (a) the geometry of point load, (b) the resulting deformation.

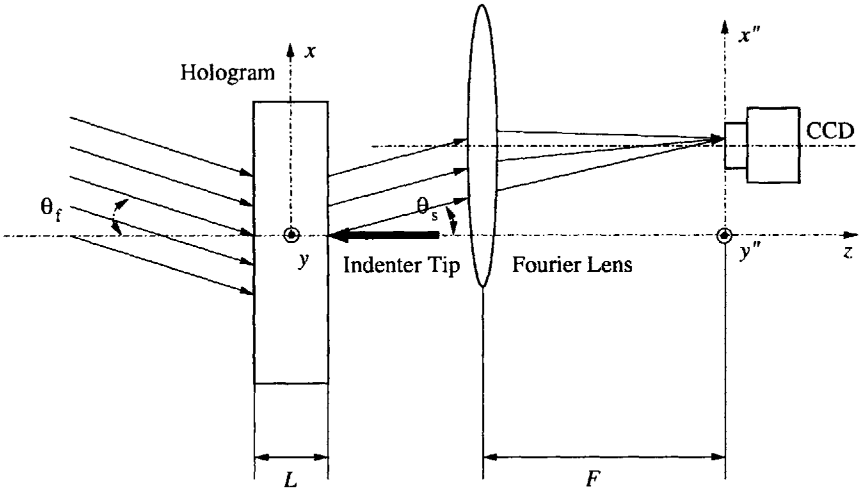

Figure 5-10: Experiment geometry when a point load is exerted on a transmission hologram

deformed using a diamond indenter tip applied normally against the back surface of the hologram. The deformation due to the indenter tip is in good agreement with the point-load described by Equation 5.35, except near the singularity point $\rho = 0$. Our experimental approach did not require force measurement; we estimated the force using the displacement reading in the indenter carrier. During the experiment, we used the same probe beam which is Bragg matched before deformation to illuminate the hologram.

First we simulated the expected change in diffracted field according to Equations 5.25 and 5.35. The results are shown in Fig. 5-11. An interesting observation is that the diffracted spot splits into "twin peaks" due to the point load deformation. This can be explained intuitively based on the deformed fringe patterns of Fig. 5-12 and the K-sphere of Fig. 5-13 as follows. From Fig. 5-12, we see that deformed grating is composed of two quasi-periodic fringe patterns, symmetric with respect to the original grating fringes. The fringes are also curved, which is indication of spatial chirp. If for the moment we neglect the spatial chirp, we obtain two gratings which are tilted with respect to the original grating, and also have smaller period because of the pressure applied by the indenter. Accordingly, we represent the twin

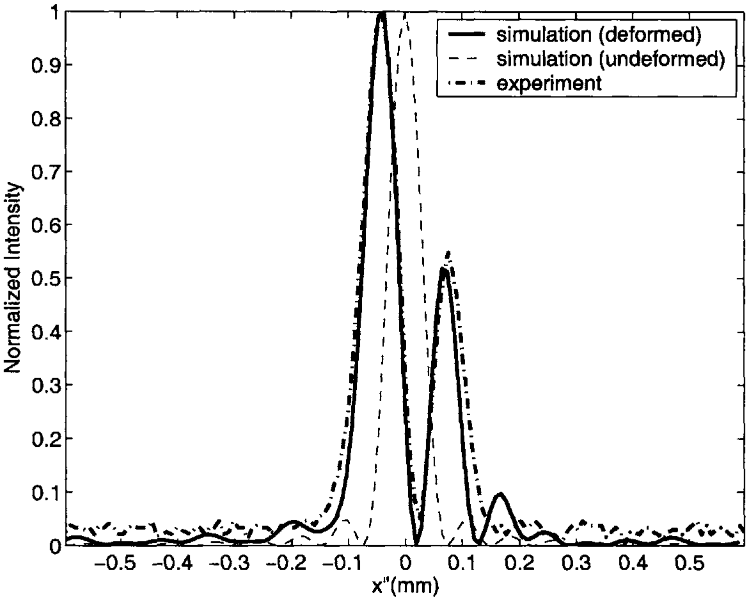

Figure 5-11: Simulated and experimental results when a point load is exerted on a transmission hologram. Parameters are wavelength $\lambda = 488nm$, the angle of reference beam $\theta_f = -7.5^o$, the angle of signal beam $\theta_s = 20^o$, the thickness of the hologram $L = 2$mm, estimated force $P = 700$N and the focal length of Fourier lens $F = 400$mm. The intensities before and after deformation were normalized by their own maximum, respectively. The maximum intensity after deformation is 19.65% of the maximum intensity before deformation.

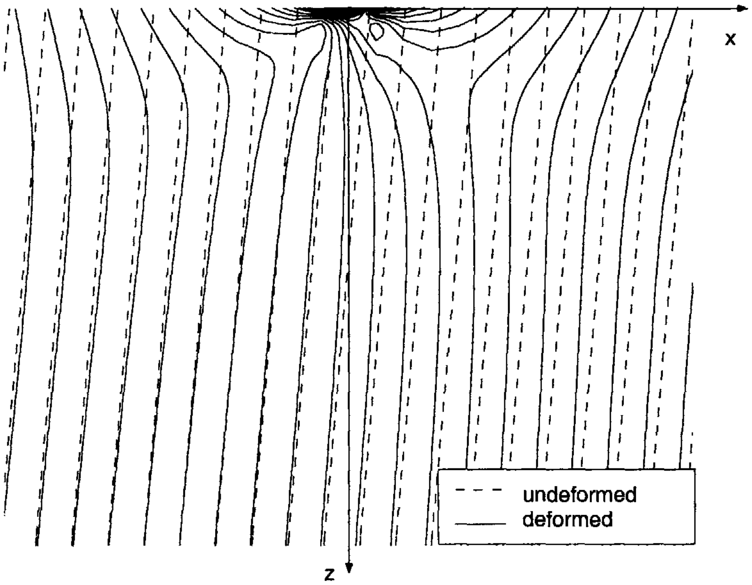

Figure 5-12: Fringe patterns of a transmission hologram due to point-load, and parameters are the same as in Fig. 5-11.

gratings with wave vectors $\mathbf{K}'_\mathbf{g}$ and $\mathbf{K}''_\mathbf{g}$ that are tilted and elongated with respect to the original wave vector $\mathbf{K}_\mathbf{g}$. Since we are reading out the hologram with the original reference $\mathbf{k}_\mathbf{f}$, the twin peaks are expected to be Bragg-mismatched. However, for small deformation, *i.e.* small deviations of the twin grating vector tips $\mathbf{K}'_\mathbf{g}$ and $\mathbf{K}''_\mathbf{g}$ from the K-sphere, we can still obtain diffraction from the partially mismatched gratings. The directions of the twin diffracted beams are denoted as $\mathbf{k}'_\mathbf{d}$ and $\mathbf{k}''_\mathbf{d}$ in Fig. 5-13; they give rise to our observed twin peak on the CCD camera after Fourier transformation by the lens. Because the Bragg mismatch amounts $\Delta\mathbf{K}'_\mathbf{g}$ and $\Delta\mathbf{K}''_\mathbf{g}$ for the twin gratings are in general different, the twin diffracted beams have different efficiencies. The elevated side lobes observed in Fig. 5-11 are due to the spatial chirp, which was neglected from the approximate explanation based on Fig. 5-13.

We performed our experiments using an indenter tip moved by a micropositioner to exert the point load on the hologram. The load position was exactly at the center of the aperture (the illumination area on the hologram.) The experimental result obtained on the CCD Camera is shown as the dash-dot line in Fig. 5-11 and is in agreement with the simulation. At the same time, we also observed some minor

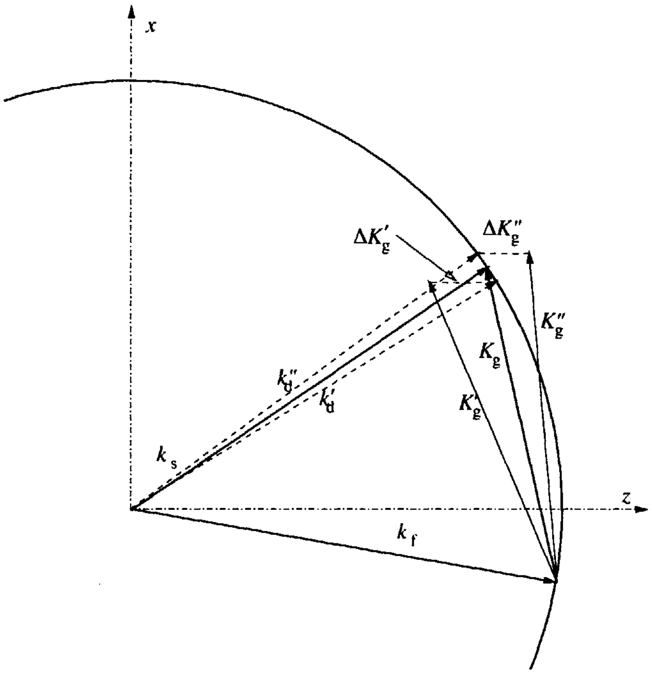

Figure 5-13: K–sphere explanation for the "twin peaks"

apodization effect mixed in our experiment result: the side lobes were suppressed and the main lobes were a little wider. Because the apodization effect of volume holograms has been accounted for in the perturbation theory inherently, the additional apodization could be due to nonuniformity of holograms and probe beams in the experiment.

We also performed simulations and experiments on a reflection type hologram. The experimental geometry is shown in Fig. 5-14. The holographic material was also from Ondax Inc., with the same shear modulus and Poisson ratio as the transmission hologram. The thickness of the reflection type hologram was $L = 1.5$mm. The angles of reference beam and signal beam were $\theta_f = 172°$ and $\theta_S = 8°$, respectively, at wavelength of 632nm. The focal length of the Fourier lens was $F = 400$mm and the hologram was also illuminated at the undeformed Bragg angle. The simulated and experimental results are shown in Fig. 5-15 and match very well. In this case, the diffracted field presents an almost symmetric pattern due to the point-load deformation. This can also be explained intuitively by the deformed fringe patterns of Fig. 5-16 and

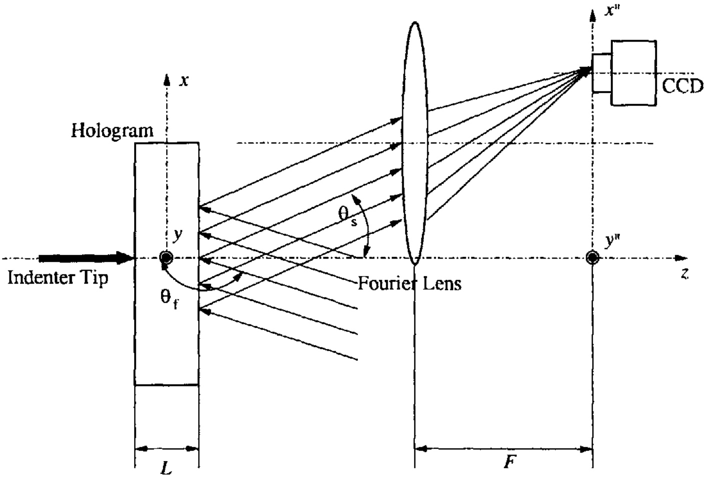

Figure 5-14: Experiment geometry when a point load is exerted on a reflection hologram

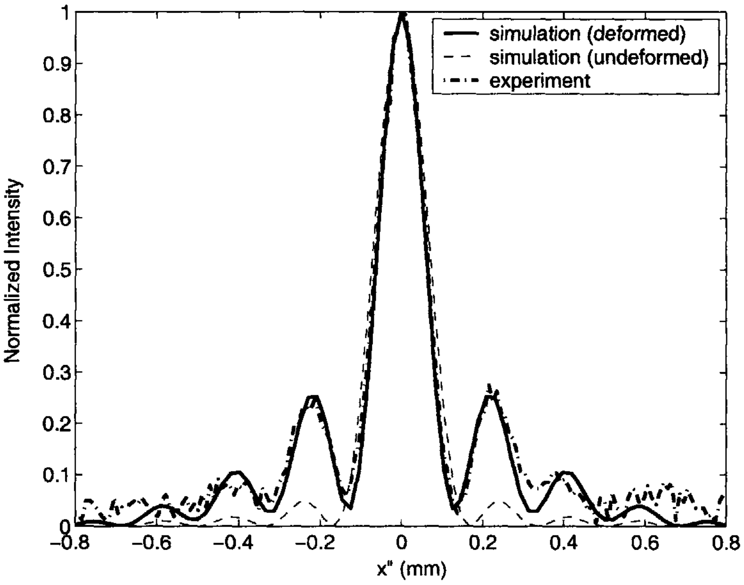

Figure 5-15: Simulated and experimental results when a point load is exerted on a reflection hologram. Parameters are wavelength $\lambda = 632nm$, the angle of reference beam $\theta_f = 172^o$, the angle of signal beam $\theta_s = 8^o$, the thickness of the hologram $L = 1.5$mm, estimated force $P = 19$N and the focal length of Fourier lens $F = 400$mm. The intensities before and after deformation were also normalized by their own maximum, respectively. The maximum intensity after deformation is 34.55% of the maximum intensity before deformation.

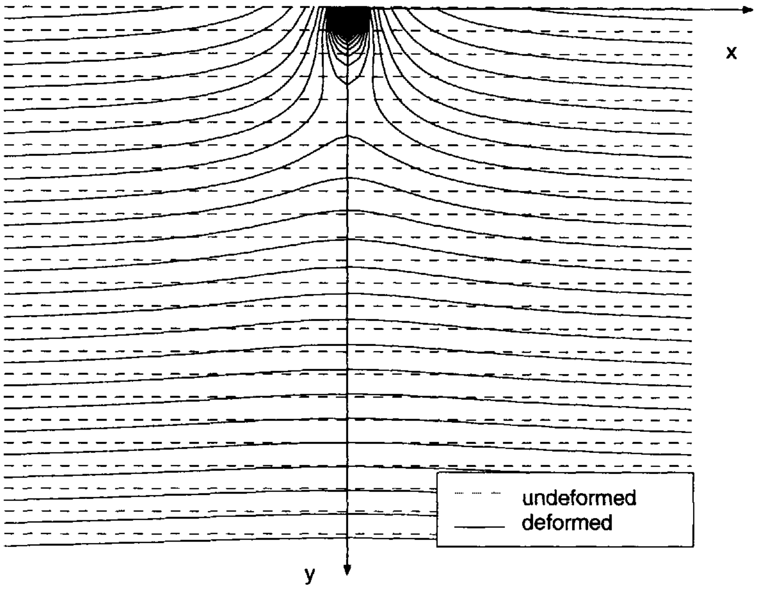

Figure 5-16: Fringe patterns of a reflection hologram due to point-load, and parameters are the same as in Fig. 5-15.

the K-sphere of Figure 5-17 as follows. In this case, the original grating vector $\mathbf{K_g}$ is split into three gratings $\mathbf{K_{g1}}$, $\mathbf{K'_g}$ and $\mathbf{K''_g}$ after deformation. $\mathbf{K_{g1}}$ remains parallel to $\mathbf{K_g}$, but is longer because of the applied pressure. The other two, $\mathbf{K'_g}$ and $\mathbf{K''_g}$, are tilted and elongated as in the transmission case and have almost the same Bragg mismatch amount $\mathbf{\Delta K'_g}$ and $\mathbf{\Delta K''_g}$. The result is a triplet peak, with a main lobe corresponding to the partially mismatched $\mathbf{K_{g1}}$, and two side lobes corresponding to the partially mismatched $\mathbf{K'_g}$ and $\mathbf{K''_g}$. The side lobes are weaker than the main lobe while the amount of Bragg mismatch for $\mathbf{K'_g}$ and $\mathbf{K''_g}$ is larger than it is for $\mathbf{K_{g1}}$. In Fig. 5-15, we can also observe minor apodization effects mixed in the experiment result, which is due to the same reasons as in the transmission geometry.

It needs to be mentioned here that success in the two experiments (transmission type and reflection type) is extremely delicate because of the difficulty to achieve the exact deformation of ideal point loading. First, we need to adjust the point load exactly at the center of the aperture. Second, the force must be normally exerted on the surface of the hologram. Third, we need the supporting and holding systems to be sufficiently stiff. The deformation is very sensitive to these factors. So in order to get

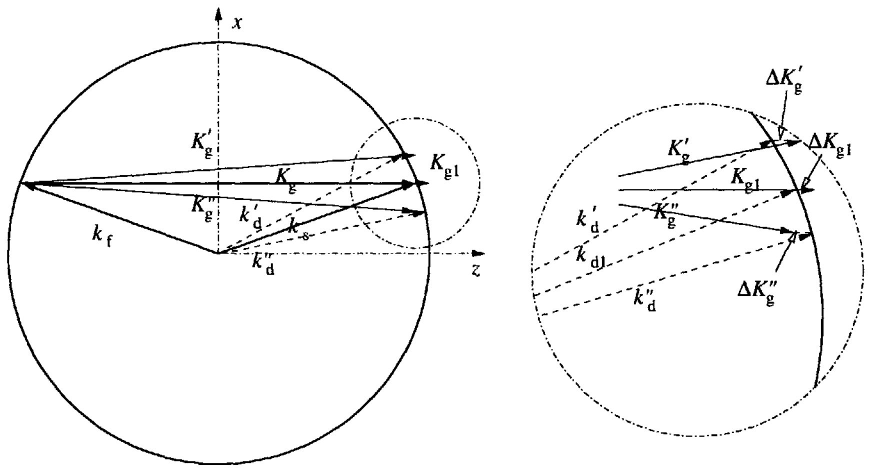

Figure 5-17: K–sphere explanation for the ”triplet peak”

the deformation as close to the ideal as possible, the adjustment in the experiments must be very precise.

5.6 Perturbation Theory Considering Dielectric Constant Change during Deformation

The conformality assumption that the dielectric constant does not change during deformation is valid when the deformation is not large enough to change the material properties of holograms. Although in some conditions the dielectric constant may change, we still can include this effect in our theory by modifying Equation 5.11 as

$$\Delta\epsilon'(\mathbf{r}') = a(\mathbf{r}')\Delta\epsilon(\mathbf{f}(\mathbf{r}')), \tag{5.36}$$

where $a(\mathbf{r}')$ is the amplitude change of dielectric modulation. Following the same derivation steps, we can easily find the diffracted field considering the dielectric constant change during deformation as

$$\begin{aligned}\tilde{E}_{\mathrm{d}}(\mathbf{r}'') \;\approx\; & \hat{E}_{\mathrm{d}}(\mathbf{r}'') + \iiint E_{\mathrm{p}}(\mathbf{r}')a(\mathbf{r}')\sum_{j=1}^{N}\frac{\left[\mathbf{K_g}\cdot A\cdot\nabla_{\mathbf{K_g}}\right]^j}{j!}\Delta\epsilon(\mathbf{r}') \\ & V(\mathbf{r}')\exp\left(-i\frac{2\pi}{\lambda}\frac{x'x''+y'y''}{F}\right) \\ & \exp\left[-i\frac{2\pi}{\lambda}\left(1-\frac{x''^2+y''^2}{2F^2}\right)z'\right]d^3\mathbf{r}', \qquad (5.37)\end{aligned}$$

where,

$$\begin{aligned}\hat{E}_{\mathrm{d}}(\mathbf{r}'') \;=\; & \iiint E_{\mathrm{p}}(\mathbf{r}')a(\mathbf{r}')\Delta\epsilon(\mathbf{r}')V(\mathbf{r}')\exp\left(-i\frac{2\pi}{\lambda}\frac{x'x''+y'y''}{F}\right) \\ & \exp\left[-i\frac{2\pi}{\lambda}\left(1-\frac{x''^2+y''^2}{2F^2}\right)z'\right]d^3\mathbf{r}', \qquad (5.38)\end{aligned}$$

If the displacement is linear, then

$$\tilde{E}_{\mathrm{d}}(\mathbf{r}'') \approx \hat{E}_{\mathrm{d}}(\mathbf{r}'') + \sum_{j=1}^{N}\frac{\left[\mathbf{K_g}\cdot A\cdot\nabla_{\mathbf{K_g}}\right]^j}{j!}\hat{E}_{\mathrm{d}}(\mathbf{r}''). \qquad (5.39)$$

5.7 Generalized Perturbation Theory to Arbitrary Holograms

We can generalize Equation 5.25 and 5.26 for arbitrary holograms which can be written as a linear superposition of many plane-wave-holograms,

$$\begin{aligned}\Delta\epsilon(\mathbf{r}) &= \sum_{m,n,l}\epsilon_{mnl}\exp\left[i2\pi\left(\frac{mx}{L_x}+\frac{ny}{L_y}+\frac{lz}{L_z}\right)\right] \\ &= \sum_{m,n,l}\epsilon_{mnl}\exp\left(i\mathbf{K}_{\mathbf{g}}^{(mnl)}\cdot\mathbf{r}\right), \qquad (5.40)\end{aligned}$$

where L_x, L_y, L_z are the dimensions of the hologram in the x, y, z direction respectively, ϵ_{mnl} is the constant expressing the hologram strength of each component, and $\mathbf{K}_{\mathbf{g}}^{(mnl)}$ is the wave vector of the grating of each component. Therefore, along the same derivation path in section 5.3 we can obtain the deformed dielectric modulation as

$$\Delta\epsilon(\mathbf{f}(\mathbf{r}')) \approx \Delta\epsilon(\mathbf{r}') + \sum_{m,n,l}\sum_{j=1}^{N} \frac{\left[\mathbf{K}_{\mathbf{g}}^{(mnl)} \cdot A \cdot \nabla_{\mathbf{K}_{\mathbf{g}}^{(mnl)}}\right]^{j}}{j!} \Delta\epsilon_{mnl}(\mathbf{r}'), \tag{5.41}$$

where

$$\Delta\epsilon_{mnl}(\mathbf{r}') = \epsilon_{mnl} \exp\left(i\mathbf{K}_{\mathbf{g}}^{(mnl)} \cdot \mathbf{r}'\right). \tag{5.42}$$

The diffracted field after deformation will render the form

$$\begin{aligned}\tilde{E}_{\mathrm{d}}(\mathbf{r}'') \approx{}& E_{\mathrm{d}}(\mathbf{r}'') + \sum_{m,n,l} \iiint E_{\mathrm{p}}(\mathbf{r}') \sum_{j=1}^{N} \frac{\left[\mathbf{K}_{\mathbf{g}}^{(mnl)} \cdot A \cdot \nabla_{\mathbf{K}_{\mathbf{g}}^{(mnl)}}\right]^{j}}{j!} \Delta\epsilon_{mnl}(\mathbf{r}') V(\mathbf{r}') \\ & \exp\left(-i\frac{2\pi}{\lambda}\frac{x'x'' + y'y''}{F}\right) \exp\left[-i\frac{2\pi}{\lambda}\left(1 - \frac{x''^2 + y''^2}{2F^2}\right) z'\right] d^3\mathbf{r}'.\end{aligned} \tag{5.43}$$

In the case of linear displacement, Equation 5.43 can be further simplified to

$$\tilde{E}_{\mathrm{d}}(\mathbf{r}'') \approx E_{\mathrm{d}}(\mathbf{r}'') + \sum_{m,n,l}\sum_{j=1}^{N} \frac{\left[\mathbf{K}_{\mathbf{g}}^{(mnl)} \cdot A \cdot \nabla_{\mathbf{K}_{\mathbf{g}}^{(mnl)}}\right]^{j}}{j!} E_{\mathrm{d}}^{(mnl)}(\mathbf{r}''), \tag{5.44}$$

where

$$\begin{aligned}E_{\mathrm{d}}^{(mnl)}(\mathbf{r}'') ={}& \iiint E_{\mathrm{p}}(\mathbf{r}') \Delta\epsilon_{mnl}(\mathbf{r}') V(\mathbf{r}') \exp\left(-i\frac{2\pi}{\lambda}\frac{x'x'' + y'y''}{F}\right) \\ & \exp\left[-i\frac{2\pi}{\lambda}\left(1 - \frac{x''^2 + y''^2}{2F^2}\right) z'\right] d^3\mathbf{r}'.\end{aligned} \tag{5.45}$$

and

$$E_{\mathrm{d}}(\mathbf{r}'') = \sum_{m,n,l} E_{\mathrm{d}}^{(mnl)}(\mathbf{r}'') \tag{5.46}$$

Equations 5.43 and 5.44 are the counterparts of equations 5.25 and 5.26, respectively.

5.8 Locus of Maximum Bragg Mismatch

In this section we calculate the locus of maximum Bragg mismatch as function of the deformation amount δ. As shown in Fig. 5-18, we want to find the point on the circle with center at O_δ and radius δ which has the maximum horizontal distance to the

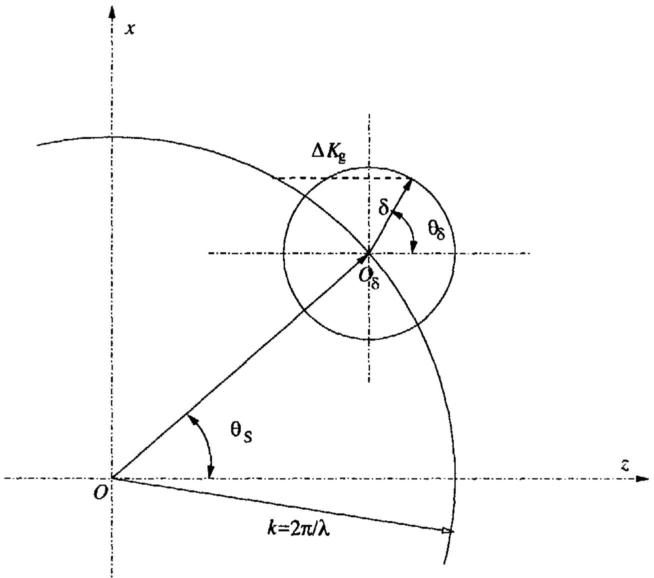

Figure 5-18: Calculation of the locus of maximum Bragg mismatch

circle of K-sphere. The horizontal distance represents the amount of Bragg mismatch $\Delta\mathbf{K_g}$. We can express the point on the circle of K-sphere as

$$z^2 + x^2 = k^2, \tag{5.47}$$

where $k = 2\pi/\lambda$, and the point on the circle O_δ as

$$(z - k\cos\theta_S)^2 + (x - k\sin\theta_S)^2 = \delta^2, \tag{5.48}$$

The amount of Bragg mismatch is the horizontal distance between two points which have the same x-coordinate and are on these two circles respectively. This distance can be calculated as a function of x,

$$\Delta\mathbf{K_g}(x) = k\cos\theta_S + \sqrt{\delta^2 - (x - k\sin\theta_S)^2} - \sqrt{k^2 - x^2}. \tag{5.49}$$

In order to get the maximum, we calculate the first order derivative of Equation 5.49 and set it equal to zero,

$$\frac{\partial \Delta \mathbf{K_g}(x)}{\partial x} = -\frac{x - k\sin\theta_S}{\sqrt{\delta^2 - (x - k\sin\theta_S)^2}} + \frac{x}{\sqrt{k^2 - x^2}} = 0. \tag{5.50}$$

Solving Equation 5.50, we obtain the x coordinate of the point, which has the maximum amount of Bragg mismatch, as

$$x_{\text{max}} = \frac{k^2 \sin\theta_S}{k \mp \delta}. \tag{5.51}$$

The result indicates that two points have the maximum amount of Bragg mismatch. One is in the interior of the K-sphere, the other is outside. Thus, the maximum Bragg mismatch direction angle can be obtained as

$$\sin\theta_\delta = \frac{x_{\text{max}} - k\sin\theta_S}{\delta} = \frac{\pm k \sin\theta_S}{k \mp \delta}. \tag{5.52}$$

After knowing the maximum Bragg mismatch direction angle to different deformation amount δ, we can sketch the locus of maximum Bragg mismatch as Fig. 5-8. When δ approaches zero, the maximum Bragg mismatch angle can be obtained as

$$\lim_{\delta\to 0} \sin\theta_\delta = \pm \sin\theta_S. \tag{5.53}$$

This means that the fastest Bragg mismatch is obtained along the direction of the signal beam, which is consistent with the discussion in Section 5.3.

5.9 Conclusions

In summary, we have derived a general solution to the problem of diffraction from a volume hologram that has been arbitrarily deformed compared to its recorded shape. We have shown that in many cases of interest, including shrinkage and indentation due to application of a point tip, a perturbation approach can predict accurately the diffracted field, and can be used to establish deformation parameters by matching the experimental measurements to analytical or numerical models. Our approach is unique in that it projects the deformation from the entire 3D volume onto the measurement, and thus it has potential for measuring even more arbitrary deformations for which analytical or numerical predictions do not exist.

Our analysis in this chapter is cast as a "forward problem," where the deformation is given and we seek the diffracted field. The future work will be the "inverse problem" which is to determine the deformation itself based on a set of observations of the field diffracted from a known (pre-deformation) volume hologram. Our ab-initio model and perturbation theory make it possible to calculate the complicated patterns analytically or numerically. This development will have high utility for the inverse problem.

Chapter 6

Conclusion

In this thesis, we have seen that photonic crystals and volume holograms acting as 3D optical elements present tremendous potential in information processing. Unlike other 2D optical elements like lenses, prisms and mirrors, 3D optical elements provide more freedom to perform better corresponding to different demands. The results presented in this thesis and in earlier work [30, 74, 106, 107, 108, 109, 110] demonstrate the enormous advantage and potential of 3D optical elements in information processing. The target applications of 3D optical information processing are broad, encompassing optical communications, optical computing, optical data storage, optical sensing and imaging. In this chapter, we recapitulate the fundamental aspects of 3D optics used in information processing and presented some directions for future research.

6.1 3D optics summary

3D optics use 3D structured media as key elements to implement information processing, such as communication, data storage, imaging and sensing. For communication, waveguiding by shear discontinuities in photonic crystals provides a new method to modify or even dynamically control the properties of the flow of the light, such as dispersion, guiding bandwidth and group velocity. Diffraction from volume holograms results in Bragg selectivity. This powerful optical property has been used in 3D imaging and sensing, as well as holographic data storage.

The shear discontinuity is introduced as a new type of defect in photonic crystals to construct a waveguide. We have demonstrated that the new type of waveguide possesses very low group velocity dispersion and maximum guiding bandwidth. It is very promising in highly integrated optical circuits that require high speed transmission and signal processing. By changing the shear shift, the mode gap and the group velocity can be tuned. This type of tuning can be implemented mechanically for dynamic reconfiguration by shearing two plates containing the half lattices relative to each other. By choosing and fixing the shear shift, the mode gap, dispersion and group velocity can be tailored for different requirements. This can be realized by lithography fabrication with very high precision. CROWs can dramatically slow down the speed of the light. By combining a CROW with shear discontinuity, we realize the active control of very slow group velocity which holds the key to the development of fast access memories and optically controlled delay lines (buffers) in optical communication systems and optical computing.

Resonant holography is developed to enhance the diffraction efficiency of volume holograms and overcome the material limitations. The crosstalk in resonant holographic systems is investigated. Through apodization using Gaussian references, the crosstalk is decreased by 2 orders. A new multiplexing method using Hermite Gaussian references (higher order modes of Gaussian beams) is proposed – mode multiplexing. Mode multiplexing eliminates the inter-pager crosstalk due to the independence of Hermite Gaussian's orthogonality on the direction of signal beam as well as decreases intra-page crosstalk to lower level through apodization. Volume holograms are used to shape the optical response of imaging systems corresponding different requirements. Based on VHI system, we proposed a technique to measure 3D deformation using volume holography. We derived the diffraction from arbitrarily deformed volume holograms using perturbation theory approach. We constructed experiments, on both transmission and reflection type of volume holograms, to verify our perturbation theory. The experimental results match our theoretical simulations very well. Based on the perturbation theory, we found the null space and maximum sensitivity. The null space can be used to avoid the effect of deformation on volume holograms while the maximum sensitivity can be used to detect the deformation using volume holography. We discussed the effect of shrinkage of volume holograms as a simple deduction from the perturbation theory.

6.2 Future work

This thesis represents a preliminary step in the direction of understanding and designing 3D optical information processing systems. There are several interesting issues that need to be addressed in utilizing further the advantages of 3D optical elements and building a systematic approach to 3D optical information processing systems. Some of these issues are:

1. Design defects capable of managing and actively controlling group velocity, group velocity dispersion (GVD), guiding bandwidth, polarization, bound states and other properties of light in integrated optical circuits. In this thesis, we have designed photonic crystal waveguides with shear discontinuities which have minimum GVD and maximum guiding bandwidth (the bandwidth is also tunable by the amount of shear shifts.) By only engineering the STRUCTURE configuration, we have also designed a novel tunable slow light device based on a CROW with a mechanically adjustable shear discontinuity to realize active control of group velocity of light. The future work will further investigate how light evolves in the vicinity of defects, study the dependence of properties of localized modes on various defects parameters, and find a set of general rules in developing optimized nanophotonic devices for different demands. In order to optimize the design of defect structures in such a huge parameter space, such as arrangements, types and sizes of defects, and various dielectric materials, we need to combine my current simulation tools and recent advances for defect calculations in solid state physics to nanophotonic device designs. These include highly localized Wannier functions as an optimal basis as well as the development of Green's function techniques and slowly varying envelope approximation (SVEA) based on Bloch waves as carriers.

2. Study defect modes in imperfect photonic crystals, such as random dislocations from original periodic or quasi-periodic lattice points, geometric distortion from the idea shape of each cell, index variation and absorption of materials. Such a study will have significant implications in the design and fabrication of nanophotonic devices. Due to the high precision and complexity requirements in nanostructure fabrication, the nanophotonic devices' tolerance to fabrication imperfections will become a serious issue. To design nanophotonic devices that are less sensitive to fabrication variances will improve the yield and decrease the cost. It would be of great importance as nanophotonic devices move towards greater commercialization. The tolerance of nanophotonic devices to dislocations is also a two-sided problem. Devices with high sensitivity can be utilized in 3-D deformation measurements. This area is also mathematically very intriguing since many current calculation methods based on fundamental results in solid state physics (e.g. Bloch theorem) no longer apply. Therefore, approximation methods, such as WKB approximation, perturbation theory and variational theorem, will play important roles, and more general mathematical models need to be developed.

3. Nonlinear and quantum effects in 3-D nanophotonics represent another new frontier just beginning to be explored. Because of possible strong resonant field concentrations and available slow group velocity in nanophotonic devices, nonlinear and quantum effects can be realized within much lower power and much smaller scale than traditional nonlinear optical devices. These enhancements can be further actively controlled by integrating them with the tunable slow light devices, e.g., tunable CROWs, since nonlinear optical effects usually are inversely proportional to the square of group velocity. Thus, active control of harmonic generation, Kerr effect (solitons), and stimulated scattering, becomes possible. Active control of nonlinear optical processes will have wide applications in many areas, such as lasers, optical communications, and biomedical optics. Another fascinating area in nonlinear 3-D nanophotonics is to achieve active modification of the band structure of photonic crystals, resulting in an-

other way to design tunable nanophotonic devices. By combining Wannier function and SVEA using Bloch waves, we can extend the research of defects design to nonlinear optical regime in order to describe and predict the nonlinear properties of nanophotonic devices and compare these results with experiments.

4. As the further development of hyperspectral VHI systems [], we are going to use a supercontinuum laser instead of a regular white light source. The high spatial coherence and low temporal coherence of the supercontinuum laser will improve resolution of VHI systems and extend working distance much further. The abundance of spectral channels will also bring unprecedented parallelism and versatility to VHI systems. The 3D deformation contains 3D information that need to be processed while the diffraction pattern measured on CCD, which is a 2D medium, is only a 2D projection rather than a direct image. Thus, more than one measurements are required or another dimension of information need to be obtained through another channel. One choice is to use wavelength/spectrum as the channel. Therefore, combining the new hyperspectral VHI systems using supercontinuum lasers with the technique we discussed in Chapter 5 is very promising to obtain real-time 3-D deformation measurements.

5. The diffraction from deformed volume holograms under illumination of randomly varying optical fields must be understood and well characterized. Coherence properties will be critical to estimate the performance of 3D deformation measurement and explore various possibilities in searching new channels to obtain information from. Some preliminary research on the coherence of 3D optical information processing system [107] are underway to understand and exploit the phenomenon better.

6. Experiment characterizing the performance of mode multiplexing system with Hermite-Gaussian reference. The generation of Hermite-Gaussian beams is the key point of the implementation of mode multiplexing. By utilizing diffractive optical elements (DOE) [111] or diode-pumped lasers [112], different Hermite-Gaussian modes can be obtained.

Bibliography

[1] J. W. Goodman. *Introduction to Fourier Optics.* Mc Graw–Hill, 2nd edition, 1996.

[2] H. Coufal, D. Psaltis, and G. Sincerbox, editors. *Holographic data storage.* Springer, 2000.

[3] H. Kogelnik. Coupled wave theory for thick hologram gratings. *Bell Syst. Tech. J.*, 48:2909–2947, 1969.

[4] N. W. Ashcroft and N. D. Mermin. *Solid State Physics.* Holt, Rinehart & Wilson, New York, 1976.

[5] E. Yablonovitch. Inhibited spontaneous emission in solid-state physics and electronics. *Phys. Rev. Lett.*, 58(20):2059, 1987.

[6] S. John. Strong localization of photons in certain disordered dielectric superlattices. *Phys. Rev. Lett.*, 58(23):2486, 1987.

[7] R. D. Meade, A. Devenyi, J. D. Joannopoulos, O. L. Alerhand, D. A. Smith, and K. Kash. Novel applications of photonic band gap materials: low-loss bends and high q cavlties. *J. Appl. Phys.*, 75(9):4753, 1994.

[8] P. R. Villeneuve, S. Fan, and J. D. Joannopoulos. Microcavities in photonic crystals: Mode symmetry, tunability, and coupling efficiency. *Phys. Rev. B.*, 54(11):7837, 1996.

[9] A. Mekis, J. C. Chen, I. Kurland, S. Fan, P. R. Villeneuve, and J. D. Joannopoulos. High transmission through sharp bends in photonic crystal waveguides. *Phys. Rev. B.*, 58(8):4809, 1998.

[10] S. Fan, , P. R. Villeneuve, J. D. Joannopoulos, and H. A. Haus. Channel drop tunneling through localized states. *Phys. Rev. Lett.*, 80(5):960, 1998.

[11] S. G. Johnson, C. Manolatou, S. Fan, P. Villeneuve, J. D. Joannopoulos, and H. A. Haus. Elimination of cross talk in waveguide intersections. *Opt. Lett.*, 23(23):1855, 1998.

[12] E. Ozbay, E. Michel, G. Tuttle, R. Biswas, K. M. Ho, J. Bostak, and D. M. Bloom. Terahertz spectroscopy of three-dimensional photonic band-gap crystal. *Opt. Lett.*, 19(15):1155, 1994.

[13] Nathan Jukam and Mark S. Sherwin. Two-dimensional terahertz photonic crystals fabricated by deep reactive ion etching in Si. *Appl. Phys. Lett.*, 23(83):21, 2003.

[14] C. Klein and C. S. Hurlbut. *Manual of Mineralogy, 20th ed.* John Wiley and Sons, New York, 1985.

[15] T. H. Wong, M. C. Gupta, B. Robins, and T. L. Levendusky. Color generation in butterfly wings and fabrication of such structures. *Opt. Lett.*, 28(23):2342–2344, 2003.

[16] D. A. Kofke and P. G. Bolhuis. Freezing of polydisperse hard spheres. *Phys. Rev. E.*, 59:618, 1999.

[17] S. Auer and D. Frenkel. Suppression of crystal nucleation in polydisperse colloids due to increase in free energy. *Nature*, 413:711, 2001.

[18] S.-Y. Lin, J. G. Fleming, D. L. Hetherington, B. K. Smith, R. Biswas, K. M. Ho, M. M. Sigalas, W. Zubrzycki, S. R. Kurtz, and J. Bur. A three-dimensional photonic crystal operating at infrared wavelengths. *Nature*, 394:251, 1998.

[19] S. Noda, K. Tomoda, N. Yamamoto, and A. Chutinan. Full three-dimensional photonic bandgap crystals at near-infrared wavelengths. *Science*, 289:604, 2000.

[20] M. Qi, E. Lidorikis, P. T. Rakich, S. G. Johnson, J. D. Joannopoulos, E. P. Ippen, and H. I. Smith. A three-dimensional optical photonic crystal with designed point defects. *Nature*, 429:538, 2004.

[21] D. Gabor. A new microscopic principle. *Nature*, 161:777, 1948.

[22] P. J. Van Heerden. Theory of optical information storage in solids. *Appl. Opt.*, 2(4):393–400, 1963.

[23] E. N. Leith, A. Kozma, J. Upatnieks, J. Marks, and N. Massey. Holographic data storage in three-dimensional media. *Appl. Opt.*, 5(8):1303–1311, 1966.

[24] D. Psaltis. Coherent optical information systems. *Science*, 298:1359–1363, 2002.

[25] D. Psaltis and F. Mok. Holographic memories. *Sci. Am.*, 273(5):70–76, 1995.

[26] J. F. Heanue, M. C. Bashaw, and L. Hesselink. Volume holographic storage and retrieval of digital data. *Science*, 265(5173):749–752, 1994.

[27] H. Lee, X.-G. Gu, and D. Psaltis. Volume holographic interconnections with maximal capacity and minimal cross talk. *J. Appl. Phys.*, 65(6):2191–2194, March 1989.

[28] D. Psaltis, D. Brady, X. G. Gu, and S. Lin. Holography in artificial neural networks. *Nature*, 343(6256):325–330, 1990.

[29] G. Barbastathis and D. J. Brady. Multidimensional tomographic imaging using volume holography. *Proc. IEEE*, 87(12):2098–2120, 1999.

[30] A. Sinha, W. Sun, T. Shi, and G. Barbastathis. Volume holographic imaging in transmission geometry. *Appl. Opt.*, 43(7):1533–1551, 2004.

[31] J. D. Joannopoulos, R. D. Meade, and J. N. Winn. *Photonic crystals*. Princeton University Press, 1995.

[32] K. M. Ho, C. T. Chan, and C. M. Soulouis. Existence of a photonic gap in periodic dielectric structures. *Phys. Rev. Lett.*, 65(25):3152, 1990.

[33] E. Yablonovitch, T. J. Gmiter, and L. M. Leung. Photonic band structure: the face-certered-cubic case employing nonspherical atoms. *Phys. Rev. Lett.*, 67(17):2295, 1991.

[34] R. D. Meade, A. M. Rappe, J. D. Joannopoulos, and O. L. Alerhand. Accurate theoretical analysis of photonic band-gap materials. *Phys. Rev. B.*, 48(11):8434, 1993.

[35] P. Yeh. *Optical waves in layered media.* Wiley, New York, 1988.

[36] J. D. Jackson. *Classical electrodynamics.* J. Wiley & Sons, second edition, 1975.

[37] S. G. Johnson, S. Fan, P. R. Villeneuve, and J. D. Joannopoulos. Guided modes in photonic crystal slabs. *Phys. Rev. B.*, 60(8):5751, 1999.

[38] S. Y. Lin, E. Chow, V. Hietala, P. R. Villeneuve, and J. D. Joannopoulos. Experimental demostration of guiding and bending of electromagnetic waves in a photonic crystal. *Science*, 282:274, 1998.

[39] M. Notomi, K. Yamada, A. Shinya, J. Takahashi, C. Takahashi, and I. Yokohama. Extremly large group-velocity dispersion of line-defect waveguides in photonic crystal slabs. *Phys. Rev. Lett.*, 87(25):253902, 2001.

[40] W. Tung and S. Fan. Creating large bandwidth line defects by embedding dielectric waveguides into photonic crystal slabs. *Appl. Phys. Lett.*, 81(21):3915, 2002.

[41] A. Jafarpour, A. Adibi, Y. Xu, and R. K. Lee. Mode dispersion in biperiodic photonic crystal waveguides. *Phys. Rev. B.*, 68:233102, 2003.

[42] T. Sondergaard and A. Lavrinenko. Large-bandwidth planar photonic crystal waveguides. *Opt. Commun.*, 203:263, 2002.

[43] M. J. Levene, J. Korlach, S. W. Turner, M. Foquet, H. G. Craighead, and W. W. Webb. Zero-mode waveguides for single-molecule analysis at high concentrations. *Science*, 299:682, 2003.

[44] A. Mekis, S. Fan, and J. D. Joannopoulos. Bound states in photonic crystal waveguides and waveguide bends. *Phys. Rev. B.*, 58(8):4809, 1998.

[45] S. G. Johnson and J. D. Joannopoulos. Block-iterative frequency-domain methods for maxwell's equations in a planewave basis. *Opt. Express*, 8:173, 201.

[46] H. A. Haus. *Waves and fields in optoelectronics.* Prentice-Hall, Englewood Cliffs, NJ, 1984.

[47] A. Adibi, Y. Xu, R. K. Lee, A. Yariv, and A. Scherer. Guiding mechanisms in dielectric-core photonic-crystal optical waveguides. *Phys. Rev. B.*, 64:033308, 2001.

[48] L. V. Hau, S. E. Harris, Z. Dutton, and C. H. Behroozi. Light speed reduction to 17 metres per second in an ultracold atomic gas. *Nature*, 397:594, 1999.

[49] M. D. Stenner, D. J. Gauthies, and M. A. Neifeld. The speed of information in a "fast-light" optical medium. *Nature*, 425:695, 2003.

[50] M. S. Bigelow, N. N. Lepeshkin, and R. W. Boyd. Superluminal and slow light propagation in a room-temperature solid. *Science*, 301:200, 2003.

[51] Y. A. Vlasov, M. O'Boyle, H. F. Hamann, and S. J. McNab. Active control of slow light on a chip with photonic crystal waveguides. *Nature*, 438:65, 2005.

[52] W. M. Robertson, G. Arjavalingam, R. D. Meade, K. D. Brommer, A. M. Rappe, and J. D. Joannopoulos. Observation of surface photons on periodic dielectric arrays. *Opt. Lett.*, 18(7):528, 1993.

[53] E. Yablonovitch, T. J. Gmiter, R. M. Meade, A. M. Rappe, K. D. Brommer, and J. D. Joannopoulos. Donor and acceptor modes in photonic band structure. *Phys. Rev. Lett.*, 67(24):3380, 1991.

[54] A. Yariv, Y. Xu, R. K. Lee, and A. Scherer. Coupled-resonator optical waveguide: a proposal and analysis. *Opt. Lett.*, 24(11):711, 1999.

[55] M. Soljacic, S. G. Johnson, S. Fan, M. Ibanescu, E. Ippen, and J. D. Joannopoulos. Photonic-crystal slow-light enhancement of nonlinear phase sensitivity. *J. Opt. Soc. Am. A*, 19(9):2052, 2002.

[56] Y. Xu, R. K. Lee, and A. Yariv. Propagation and second-harmonic generation of electromagnetic waves in a coupled-resonator optical waveguide. *J. Opt. Soc. Am. A*, 17(3):387, 2000.

[57] M. F. Yanik and S. Fan. Stopping light all optically. *Phys. Rev. Lett.*, 92(8):083901, 2004.

[58] D. Psaltis, M. Levene, A. Pu, G. Barbastathis, and K. Curtis. Holographic storage using shift multiplexing. *Opt. Lett.*, 20(7):782–784, April 1995.

[59] G. Barbastathis, M. Levene, and D. Psaltis. Shift multiplexing with spherical reference waves. *Appl. Opt.*, 35:2403–2417, 1996.

[60] D. Psaltis and N. Farhat. Optical information-processing based on an associative-memory model of neural nets with thresholding and feedback. *Opt. Lett.*, 10(2):98–100, 1985.

[61] D. Z. Anderson. Coherent optical eigenstate memory. *Opt. Lett.*, 11:56, 1986.

[62] W. H. Steier, G. T. Kavounas, R. T. Sahara, and J. Kumar. Enhanced optooptical light deflection using cavity resonance. *Appl. Opt.*, 27(8):1603–1606, 1988.

[63] S. A. Collins and H. J. Caulfield. Optical holographic interconnects: categorization and potential efficient passive resonated holograms. *J. Opt. Soc. Am. A*, 6(10):1568–1577, 1989.

[64] A. Sinha and G. Barbastathis. Resonant holography. *Opt. Lett.*, 27:385–387, 2002.

[65] L. Menez, I.Zaquine, and A. Maruani. Intracavity bragg grating. *J. Opt. Soc. Am. B*, 16(11):1848–1855, 1999.

[66] W. Liu, D. Psaltis, and G. Barbastathis. Real time spectral imaging in three spatial dimensions. *Opt. Lett.*, 27:854–856, 2002.

[67] Lord Rayleigh. *Phil. Mag.*, 8:261, 1879.

[68] H. Kogelnik and T. Li. Laser beams and resonators. *Proc. IEEE*, 5(10):1550–1567, 1966.

[69] C. Gu, J. Hong, I. McMichael, R. Saxena, and F. Mok. Cross-talk-limited storage capacity of volume holographic memory. *J. Opt. Soc. Am. A*, 9(11):1978–1983, November 1992.

[70] C. Gu, F. Dai, and J. Hong. Statistics of both optical and electrical noise in digital volume holographic data storage. *Electr. Let.*, 32(15):1400–1402, 1996.

[71] Mark A.Neifeld and Mark McDonald. Technique for controlling cross-talk noise in volume holography. *Opt. Lett.*, 21(16):1298–1300, 1996.

[72] Foster Dai and Claire Gu. Effect of gaussian references on cross-talk noise reduction in volume holographic memory. *Opt. Lett.*, 22(23):1802–1804, 1997.

[73] I. S. Gradshtein and I. M. Ryzhik. *Table of Integrals, Series, and Products.* Academic Press, fifth edition, 1994.

[74] Arnab Sinha. *Imaging using volume holograms.* PhD thesis, Massachusetts Institute of Technology, 2004.

[75] D. Brady and D. Psaltis. Control of volume holograms. *J. Opt. Soc. Am. A*, 9(7):1167–1182, 1992.

[76] A. Stein and G. Barbastathis. Axial imaging necessitates loss of lateral shift invariance. *Appl. Opt.*, 41:6055-6061, 2002.

[77] E. Leith and J. Upatnieks. Wavefront reconstruction and communication theory. *J. Opt. Soc. Am.*, 52:1123, 1962.

[78] G. Barbastathis, M. Balberg, and D. J. Brady. Confocal microscopy with a volume holographic filter. *Opt. Lett.*, 24(12):811–813, 1999.

[79] W. S. Colburn and K. A. Haines. Volume hologram formation in photopolymer materials. *Appl. Opt.*, 10(7):1636–1641, 1971.

[80] B. L. Booth. Photopolymer material for holography. *Appl. Opt.*, 14(3):593–601, 1975.

[81] D. H. R. Vilkomerson and D. Bostwick. Some effects of emulsion shrinkage on a hologram's image space. *Appl. Opt.*, 6(7):1270–1272, 1967.

[82] P. Hariharan. *Optical Holography: Principles, Techniques, and Applications.* Cambridge Universtity Presss, 1984.

[83] N. Chen. Aberrations of volume hologrphic grating. *Opt. Lett.*, 10(9):472–474, 1985.

[84] D. Gabor. Microscopy by reconstructed wavefronts. *Proc. Roy. Soc*, A197:454, 1949.

[85] D. Gabor. Microscopy by reconstructed wavefronts II. *Proc. Phys. Soc*, B64:449, 1949.

[86] X. Yi, P. Yeh, C. Gu, and S. Campbell. Crosstalk in volume holographic memory. *Proceedings of the IEEE*, 87(11):1912–1930, 1999.

[87] R. M. Shelby, D. A. Waldman, and R. T. Ingwall. Distortions in pixel-matched holographic data storage due to lateral dimensional change of photopolymer storage media. *Opt. Lett.*, 25(10):713–715, 2000.

[88] D. Psaltis, D. Brady, G. Xiang-Guang, and S. Lin. Holography in artificial neural networks. *Nature*, 343(6256):325–330, 1990.

[89] C. Zhao, J. Liu, Z. Fu, and R. T. Chen. Shrinkage-corrected volume holograms based on photopolymeric phase media for surface-normal optical interconnects. *Appl. Phys. Lett.*, 71(11):1464–1466, 1997.

[90] A. A. Friesem and J. L. Walker. Experimental investigations of some anomalies in photographic plates. *Appl. Opt.*, 8(7):1504–1506, 1969.

[91] P. Hariharan and C. M. Chidley. Rehalogenating bleaches for photographic phase holograms: the influence of halide type and concentration on diffraction efficiency and scattering. *Appl. Opt.*, 26(18):3895–3898, 1987.

[92] P. Hariharan and C. M. Chidley. Rehalogenating bleaches for photographic phase holograms: Ii. spatial frequency effects. *Appl. Opt.*, 27(18):3852–3854, 1988.

[93] J. T. Gallo and C. M. Verber. Model for the effects of material shrinkage on volume holograms. *Appl. Opt.*, 33(29):6797–6804, 1994.

[94] D. A. Waldman, H.-Y. S. Li, and M. G. Horner. Volume shrinkage in slant fringe gratings of a cationic ring-opening holographic recording material. *J. Imaging Sci. Technol.*, 41(5):497–514, 1997.

[95] C. M. Vest. *Holographic Interferometry.* Wiley, New York, 1979.

[96] P. K. Rastogi. *Holographic Interferometry.* Springer-Verlag, Berlin, 1994.

[97] Valery P. Shchepinov et al. *Strain and stress analysis by holographic and speckle interferometry.* Wiley, New York, 1996.

[98] P. S. Theocaris. *Moire Fringes in Strain Analysis.* Pergamon, New York, 1969.

[99] A. J. Durelli and V. J. Parks. *Moire Analysis of Strain.* PrenticeHall, Englewood Cliffs, NJ, 1970.

[100] M. A. Kronrod, L. P. Yaroslavski, and N. S. Merzlyakov. Computer synthesis of transparency holograms. *Sov. Phys. Tech. Phys.*, 17:329–332, 1972.

[101] U. Schnars and W. Juptner. Direct recording of holograms by a ccd target and numerical reconstruction. *Appl. Opt.*, 33(2):179–181, 1994.

[102] Y. Pu and H. Meng. An advanced off-axis holographic particle image velocimetry (HPIV) system. *Exp. Fluids*, 29:184–197, 2000.

[103] J. Zhang, B. Tao, and J. Katz. Turbulent flow measurements in a square duct with hybrid holographic PIV. *Exp. Fluids*, 23:373–389, 1997.

[104] C. Cohen-Tannoudji, B. Diu, and F. Laloë. *Quantum Mechanics*. Hermann & Wiley-Interscience, Paris, France, 1977.

[105] K. L. Johnson. *Contact Mechanics*. Cambridge Universtity Presss, 1985.

[106] K. Tian and G. Barbastathis. Cross talk in resonant holographic memories. *J. Opt. Soc. Am. A*, 21(5):751–756, 2004.

[107] K. Tian and G. Barbastathis. Coherence patterns originating from incoherent volume sources. *Opt. Lett.*, 29(7):670–672, 2004.

[108] K. Tian, T. Cuingnet, Z. Li, W. Liu, D. Psaltis, and G. Barbastathis. Diffraction from deformed volume holograms: perturbation theory approach. *J. Opt. Soc. Am. A*, 22(12):2880–2889, 2005.

[109] K. Tian, G. Babarstathis, and J. Hong. Localized propagation modes guided by shear discontinuities in photonic crystals. *submitted to Opt. Express.*

[110] K. Tian, G. Babarstathis, and J. Hong. Tunable group velocity in a coupled-resonator optical waveguide (CROW) formed by shear discontinuities in a photonic crystal. *submitted to Phys. Rev. B.*

[111] V. S. Pavelyev, V. A. Soifer, M. Duparre, R. Kowarschik, B. Ludge, and B. Kley. Iterative calculation, manufacture and inverstigation of doe forming uninodal complex distribution. *Opt. Lasers Eng.*, 29:269–279, 1998.

[112] Y. F. Chen, T. M. Huang, C. F. Kao, C. L. Wang, and S. C. Wang. Generation of hermite-gaussian modes in fiber-coupled laser-diode end-pumped lasers. *IEEE J. Q. El.*, 33(6):1025–1031, 1997.